

DIPLOMA THESIS

Full-Sphere $\sqrt{\Delta RCS}$ Characterization of Passive UHF RFID Tags

Conducted in partial fulfillment of the requirements for the degree of a

Diplom-Ingenieur (Dipl.-Ing.)

by

Bernhard Grill, BSc

Matriculation Number: 01608707

Institute of Electrodynamics, Microwave and Circuit Engineering Faculty of Electrical Engineering and Information Technology TU Wien

Supervisor: Assoc. Prof. Dipl.-Ing. Dr. techn. Holger Arthaber Assistant Supervisor: Dipl.-Ing. Thomas Michael Pohl, BSc

> Vienna, Austria October 2025

Erklärung zur Verfassung der Arbeit

Hiermit erkläre ich, dass die vorliegende Arbeit gemäß dem Code of Conduct – Regeln zur Sicherung guter wissenschaftlicher Praxis (in der aktuellen Fassung des jeweiligen Mitteilungsblattes der TU Wien), insbesondere ohne unzulässige Hilfe Dritter und ohne Benutzung anderer als der angegebenen Hilfsmittel, angefertigt wurde. Die aus anderen Quellen direkt oder indirekt übernommenen Daten und Konzepte sind unter Angabe der Quelle gekennzeichnet. Die Arbeit wurde bisher weder im In- noch im Ausland in gleicher oder in ähnlicher Form in anderen Prüfungsverfahren vorgelegt.

Wien, 1. Oktober 2025

Bernhard Grill

Abstract

Phase-based localization using passive ultra high frequency (UHF) radio-frequency identification (RFID) technology has received plentiful attention due to its low cost and sufficient localization accuracy. An accurate phase model must incorporate the phase response of the tag, which is typically modeled in the literature without any dependency on the spherical direction. This assumption might hold if the tag is an ideal dipole in free space, but it is no longer valid in practical scenarios, where tags are mounted on complex objects. Comprehensive measurement data is lacking, and therefore, this thesis addresses this gap by developing a measurement system capable of determining the phase response of tags, either in free space or on objects, on the entire sphere. The essential parameter for obtaining the phase response is the square root delta radar cross-section ($\sqrt{\Delta}$ RCS), which is the complex-valued difference of the tag's two different radar cross-sections (RCSs) that are used for backscatter communication. Based on prior investigations, it is known that self-interference, especially in monostatic arrangements, limits the dynamic range of the measurement system. By the use of additional carrier cancellation hardware, the dynamic range can be improved at the expense of non-standard components and an additionally required control-loop. To proceed with off-the-shelf measurement equipment, this work follows a different approach: A bistatic arrangement together with spherical wave expansion (SWE) is used to lower the requirements on the measurement system's dynamic range. The SWE represents the radiated field as a weighted sum of spherical basis functions. Essentially, this means that measurement points that cannot be covered by the dynamic range of the measurement system can be represented through the SWE. The bistatic arrangement allows to separate transmit and receive paths, which inherently reduces the amount of self-interference. Three possible assignments were investigated and developed which differ in the duration per measurement sample, the hardware complexity, the maximum power density at the tag, and the dynamic range. Since the bistatic arrangement introduces an uncalibrated signal path, a calibration procedure had to be developed. Reciprocal tag behavior can be assumed, therefore, activating the tag from both paths by simply reversing TX/RX, under the fulfillment of the minimum power density at the tag, leverages a two-step path calibration. Although the measurements are bistatic, a calibrated monostatic $\sqrt{\Delta RCS}$ can be determined. A measurement system consisting of three configurations and off-the-shelf hardware leveraging the determination of the $\sqrt{\Delta RCS}$ of tags, either in free space or on objects, on the entire sphere, was developed. Applied scenarios were compared, and it was shown that tagged objects indeed show a strong dependency on the spherical direction, non-negligible for most phase-based localization algorithms. This indicates the importance of collecting further measurement data, which will contribute to improving the phase model, and eventually, the accuracy of localization.

Kurzfassung

Phasenbasierte Lokalisierung mithilfe von Verfahren zur automatisierten Identifikation über Funk (engl. radio-frequency identification (RFID)) im UHF-Bereich (engl. ultra high frequency (UHF)) hat, durch ihre geringen Kosten und dabei ausreichende Genauigkeit, viel Aufmerksamkeit erlangt. Ein präzises Phasenmodell muss die Phasenantwort des Transponders (engl. Tag) berücksichtigen, jedoch wird diese in der Literatur typischerweise ohne Abhängigkeit von der sphärischen Richtung modelliert. Diese Annahme könnte zutreffen, wenn es sich bei dem Tag um einen idealen Dipol im freien Raum handelt, aber in der Praxis, wo Tags an komplexe Objekte angebracht sind, ist sie nicht mehr gültig. Umfangreiche Messdaten dazu fehlen und daher zielt diese Arbeit darauf ab, ein Messsystem zu entwickeln welches fähig ist, die Phasenantwort von Tags, entweder im Freiraum oder angebracht an Objekten, auf der gesamten Sphäre zu bestimmen. Der essenzielle Parameter für die Bestimmung der Phasenantwort ist der Wurzel Delta Radarquerschnitt (engl. square root delta radar cross-section ($\sqrt{\Delta RCS}$)), welcher die komplexwertige Differenz der beiden Radarquerschnitte, die ein Tag für die Rückstreukommunikation verwendet, darstellt. Basierend auf vorangegangenen Untersuchungen weiß man, dass durch signifikante Selbstinterferenz, vor allem in monostatischen Anordnungen, der Dynamikumfang des Messsystems limitiert ist. Mit der Nutzung von zusätzlicher Hardware zur Trägerunterdrückung kann der Dynamikumfang verbessert werden, jedoch auf Kosten von Nicht-Standardkomponenten und einer zusätzlich notwendigen Regelschleife. Um bei kommerziellem (engl. off-the-shelf) Messequipment zu bleiben, verfolgt diese Arbeit einen anderen Ansatz: Eine bistatische Anordnung gemeinsam mit einer sphärischen Modenzerlegung (engl. spherical wave expansion (SWE)), um die Anforderungen an den Dynamikumfang des Messsystems zu senken. Die SWE ermöglicht eine analytische Beschreibung des abgestrahlten Feldes mithilfe von gewichteten sphärischen Basisfunktionen und das bedeutet im Wesentlichen, dass Messpunkte, welche nicht durch den Dynamikumfang des Messsystems abgedeckt werden, durch die SWE trotzdem repräsentiert werden können. Die bistatische Anordnung, erlaubt die Separation von Sende- und Empfangspfad, was inhärent zur Reduktion der Selbstinterferenz führt. Drei mögliche Zuordnungen wurden untersucht und ausgearbeitet welche sich in Dauer pro Messpunkt, Hardwarekomplexität, Maximale Leistungsdichte am Tag und Dynamikumfang unterscheiden. Die bistatische Anordnung führt einen unkalibrierten Signalpfad ein und daher musste ein Kalibrationsverfahren entwickelt werden. Es kann von einem reziproken Verhalten des Tags ausgegangen werden, daher ermöglicht das Aktivieren des Tags von beiden Signalpfaden, durch einfaches Vertauschen von TX/RX unter Erfüllung der Minimalen Leistungsdichte am Tag, eine zweistufige Pfadkalibration. Obwohl die Messungen bistatisch durchgeführt werden, kann nun eine kalibrierte monostatische $\sqrt{\Delta RCS}$ bestimmt werden. Es konnte somit ein Messsystem, bestehend aus drei Konfigurationen und off-the-shelf Equipment, erstellt werden, welches das Bestimmen der $\sqrt{\Delta RCS}$, von Tags im freien Raum oder angebracht an Objekten, auf der gesamten Sphäre ermöglicht. Praktische Anwendungsfälle wurden verglichen und es wurde gezeigt, dass getaggte Objekte eine starke Abhängigkeit von der sphärischen Richtung aufweisen, welche nicht vernachlässigbar für die meisten Phasenbasierten Lokalisierungsalgorithmen ist. Das indiziert die Dringlichkeit weitere Messdaten zu sammeln, welche dazu beitragen das Phasenmodell zu verbessern und schließlich die Genauigkeit der Lokalisierung.

Acknowledgements

I want to thank:

- My family, for the many years of unwavering support and belief in me. Without you, this journey would not have been possible.
- My supervisor, Prof. Holger Arthaber, for his technical expertise, constant support, and guidance throughout this work.
- The members of the microwave engineering group at TU Wien for all their advice and help, especially Dipl.-Ing. Thomas Michael Pohl for his detailed review of this thesis.
- Dr. techn. Jure Soklič for sharing the framework of pattern stitching that enabled a full-sphere instead of a less-than-full-sphere analysis in the first place and for reviewing parts of this thesis.

Table of Contents

1	Intr	oduct	ion 1
	1.1	Motiv	ation
	1.2	Proble	em Statement
	1.3	Objec	tives
	1.4	Thesis	Structure
2	\mathbf{RF}	CS, and Antenna Measurements 5	
	2.1	RFID	System Operation
		2.1.1	Core Components
		2.1.2	Passive vs. Active
		2.1.3	$R \Rightarrow T$ Communication
		2.1.4	$T\Rightarrow R$ Communication
	2.2	From	RCS to Δ RCS to Δ RCS
		2.2.1	Definition RCS IEEE
		2.2.2	Definition ΔRCS
		2.2.3	Derivation $\sqrt{\Delta RCS}$
	2.3	RCS a	and Antenna Measurements
		2.3.1	Fundamental Parameters
		2.3.2	Test Ranges
		2.3.3	Test Range at TU Wien
3	$\sqrt{\Delta}$	RCS C	Characterization Method 16
	3.1	Anten	na Arrangements
		3.1.1	Monostatic
		3.1.2	Configuration Probe-TX
		3.1.3	Configuration Probe-RX
		3.1.4	Configuration Probe-RX-C
	——————————————————————————————————————		rement Setup Blocks
		3.2.1	RF Signal Generation and Modulation
		3.2.2	Measurement Instrument
		3.2.3	Calibration
		3.2.4	Sequencer
	3.3	Measu	rement Setup Overview
	3.4	Measu	rement Procedure
		3.4.1	Power Leveling
		3.4.2	Parameters
		3.4.3	Data Acquisition and Post-Processing
	3.5	Deter	mination of the $\sqrt{\Delta RCS}$
		3.5.1	Tag Model
		3.5.2	Antenna Coupling Model
		3.5.3	Resolving the Unknown Path
		3.5.4	Embedding the $\sqrt{\Delta RCS}$

	3.6	Link E	${f Sudget}$	36							
		3.6.1	R⇒T Budget	37							
		3.6.2	$T\Rightarrow R \text{ Budget } \dots $	38							
		3.6.3	Leakage, Phase and Thermal Noise	38							
4	Results										
	4.1	Tag ur	ider Test	39							
	4.2	$\sqrt{\Delta RC}$	$\overline{ ext{CS}}$ Power Dependency	39							
	4.3										
		4.3.1		40							
		4.3.2	Hardware Complexity	42							
		4.3.3		42							
		4.3.4		43							
	4.4	Long-		46							
	4.5			48							
5	Exp	ansion	to the Full Sphere	5 0							
	5.1	Introd	uction to the Spherical Wave Expansion	50							
	5.2		uction to Pattern Stitching	51							
	5.3			52							
	5.4			54							
		5.4.1	Tag in Free Space	55							
		5.4.2	Tag on Object	56							
	5.5	Summ	ary	61							
6	Con	clusio	1	62							
References											
A	Util	lized E	quipment and Software	68							

List of Figures

2.1	Link Timing for a Single Tag and Response	7
2.2	Equivalent Circuit of a Passive RFID Tag	8
2.3	Spherical Near-Field Test Range at TU Wien	14
3.1	Exemplary Monostatic Arrangement	17
3.2	Bistatic Configuration Probe-TX	18
3.3	Bistatic Configuration Probe-RX	19
3.4	Combined Monostatic-Bistatic Configuration Probe-RX-C	20
3.5	RF Signal and Query Command Generation Block Diagram	21
3.6	Measurement Setup Block Diagram	22
3.7	Implemented Link Timing	24
3.8	Full Measurement Setup with Configuration Probe-RX-C	25
3.9	Photograph of the Hardware Setup	26
3.10		27
	Principle of the Delta Tag Response Determination	28
3.12	T⇒R Preamble with Indications for FFT Method and Correlation Sequence	29
	Measurement Continuous Tag Modulation in the Complex Plane	30
	Measurement Continuous Tag Modulation in the Frequency Domain	31
	Backscatter-Based RFID Tag Model	32
3.16	Antenna Coupling Model	33
4.1	Analysis of the $\sqrt{\Delta RCS}$ Power Dependency	40
4.2	Measurement Setup to Evaluate the Dynamic Range	44
4.3	Comparison of the Achieved Dynamic Ranges	45
4.4	Analysis of the Long-Term $\sqrt{\Delta RCS}$ Stability	47
4.5	Label on Teflon Measurement Orientation	49
4.6	Truncated-Sphere $\sqrt{\Delta}$ RCS Pattern with the Label on Teflon	49
5.1	Comparison of Analytical SWCs	54
5.2	Full-Sphere $\sqrt{\Delta RCS}$ Patterns with the Label on Teflon and in Free Space .	57
5.3	Empty Tagged Crate Measurement Orientations	58
5.4	Full-Sphere $\sqrt{\Delta RCS}$ Pattern with the Label on an Empty Crate	59
5.5	Filled Tagged Crate Measurement Orientations	60
5.6	Full-Sphere $\sqrt{\Delta RCS}$ Pattern with the Label on an Filled Crate	61



List of Tables

3.1	Link Budget of the Implemented Configurations	37
4.1	Performance Comparison of the Implemented Configurations	41
4.2	Dimensions of the Label on Teflon or in Free Space	48
5.1	SNR and SMSE Evaluation for the Label on Teflon and in Free Space	55
5.2	Dimensions of the Crate	58
5.3	SNR and SMSE Evaluation for the Empty Tagged Crate	59
5.4	SNR and SMSE Evaluation for the Filled Tagged Crate	61
A.1	Overview of the Equipment and Software Used	68

Abbreviations

 ΔRCS delta radar cross-section

 $\sqrt{\Delta RCS}$ square root delta radar cross-section

AUT antenna under test

BLF backscatter link frequency

CW continous wave

EPC electronic product code

FF far-field

FFT fast Fourier transform

FSPL free-space path loss

IC integrated circuit

MRE minimum radial extent

NF near-field

PA power amplifier

RFID radio-frequency identification

RN16 random number 16-bit

RX receive

SMSE scaled mean square error

SNR signal-to-noise ratio

SWC spherical wave coefficient

SWE spherical wave expansion

TX transmit

UHF ultra high frequency

VSA vector signal analyzer

Chapter 1

Introduction

Wireless radio-frequency identification (RFID) technology [1] enhances automated identification and tracking of objects and is used in a wide range of areas such as healthcare, logistics, manufacturing, retail, and many more professional sectors. In what follows, RFID is explained based on an applied scenario in the fashion industry.

1.1 Motivation

Imagine a situation where a customer enters a fashion store to buy, e.g., a two-piece suit for a man or a woman [2]. Apart from liking the color, the style, the fabric, the customer wants the exact waist size, and leg length, but also the correct jacket size and arm length. Typically, the store will offer this sort of garment in many size variations. Unless the correct size combination is available when and where the customer wants it, they may be disappointed and leave the store empty handed. But if the desired suit is not available, does that mean it is truly unavailable, i.e., there are no units left in the store or in the backroom? Or are there perhaps still units that have been hopelessly misplaced and simply cannot be found?

Especially the fashion industry is a highly dynamic environment, with ever-changing fashion trends (short product life cycles) and unpredictable demand [3]. To deal with these circumstances, an efficient supply chain management and an accurate inventory is of utter importance [4]. Although barcode scanning is the pervasive technology used for inventory control and also at the point of sale, it suffers from three main limitations [5]: (i) It requires line of sight scanning, i.e., manual placement and orientation of the barcode to be read. (ii) Only one item can be scanned at a time. (iii) It is only a unique identifier on the product-level but not on the item-level. Inevitably, any human interaction required for scanning the barcodes, is prone to errors, e.g., scanning the same article accidentally twice, and moreover, the process is time-consuming. This renders the inventory control rather difficult and a certain level of inaccuracy is inevitable.

After seeking an alternative to barcodes, which does not require human interaction in the scanning process and allows for faster reads, the solution was found in the related RFID technology. Like barcode systems, RFID systems comprise at least two elements: a reading device (also known as reader or interrogator) and an information carrying device [1]. The information carrying device, in barcodes, is a printed label, whereas in RFID, it is a tag (also known as transponder). A tag comprises in its simplest form two components which are an antenna and a chip mounted on a substrate.

In RFID the information is no longer embedded in the systematic pattern of black bars and white spaces, it is stored in the memory of the chip. The specific barcode format and encoding is standardized, for example, by the European article number (EAN) and in the case of the EAN-13, the sequence is made up 13 digits, embedding generic product

2 1. Introduction

information, e.g., brand name, product type, color, and size. In contrast, in RFID, the tag stores an electronic product code (EPC) which provides an unique identity (UID) for each individual item to which the tag is attached. In addition to the generic product information, EPC could include, the price, the charge number, and the item number in the respective charge. Having a UID means that, e.g., the garments can be counted without the need to worry about counting duplicates.

Since different communication principles and applications of RFID arise dependent on the utilized transmit (TX) frequency, it is important to categorize them [6]:

- Low frequency (LF) (between 125 kHz and 134 kHz) and high frequency (HF) (13.56 MHz) RFID systems: These systems are based on inductive coupling between the reader and the tag antenna. Depending on the mutual inductance, the reading range is in the order of several centimeters and up to 1 m in HF RFID. LF RFID is popular for animal identification as tags can be read even in the presence of water or salt in this frequency range. HF RFID is widely used for contactless smart cards supporting access control or financial transactions.
- Ultra high frequency (UHF) (between 860 MHz and 960 MHz) and microwave (2.45 GHz and 5.8 GHz) RFID systems: These systems are based on radiative coupling, i.e., electromagnetic waves propagating between reader and tag and in particular UHF RFID is predominant in use. In contrast, microwave RFID systems allow for a wider bandwidth, which is of interest in localization purposes but their short reading range limits their applicability and thus they only play a minor role.

Throughout this thesis, the focus is on UHF RFID in the frequency range from 865 MHz to 868 MHz as allocated by the European Telecommunications Standards Institute (ETSI) [7].

In UHF RFID, the reader is an radio-frequency (RF) transceiver connected to an antenna to communicate with the tag via radio waves. The tag is typically a passive device, i.e., it has no onboard power source (battery-less) and cannot initiate communication. Therefore, the reader must provide an unmodulated RF carrier, i.e., a continuous wave (CW) signal, which allows the tag to harvest its operating power from it. Then, communication is initiated by the reader, by sending a query command to which the tag responds with its EPC [8]. A principal difference to barcode systems is that UHF RFID reader and tags can communicate with each other without being in each others line of sight. Moreover, UHF RFID systems implement a multiple access scheme that allows readers to successfully read tags in bulk. The reading distance is enhanced from about 0.5 m in barcode systems to roughly 10 m in passive UHF RFID systems. Due to this benefits, UHF RFID is technically more feasible to barcodes, but also significantly more expensive.

1.2 Problem Statement

Not only to perform simple identification by reading the tags is of interest, but also to determine their exact position. Over the years, many localization strategies with UHF RFID have been proposed, see [9, 10] where the authors give surveys of methods based on received signal strength (RSS), phase, time of flight (ToF), and fingerprinting techniques. RSS-based methods suffer for multiple reasons, such as propagation environment, tag orientation, and properties of the tagged object. ToF-based methods require high-accuracy clock synchronization, which significantly increases the cost. Fingerprinting techniques



3 1. Introduction

require pretraining, which limits their adaptability to different environments. Eventually, phase-based methods do not suffer from these disadvantages, and hence, received plentiful attention in research activities, see [11-17]. Such methods rely on measuring the phase of the backscattered signal φ from the tag to the reader to determine the tag's position. An accurate phase-based localization model requires the incorporation of information about the phase of the tag modulation. A typical phase model, like the one presented in [9] reads

$$\varphi = (\varphi_r + \varphi_T + \varphi_{TX} + \varphi_{RX}) \mod 2\pi , \qquad (1.1)$$

where φ_r is the phase shift resulting from the distance between the reader and the tag antenna, $\varphi_{TX}(\varphi_{RX})$ is the phase shift of the transmission(receiving) hardware, and φ_T is the phase of the tag modulation. Equation (1.1) does not incorporate any dependency on the spherical direction (θ, ϕ) . This assumption might hold true if the tag is an ideal dipole in free space, but it is no longer valid in applied scenarios, where tags are mounted on complex objects, and the tag can indeed show dependency on (θ, ϕ) .

The essential parameter for determining the phase of the tag modulation is the square root delta radar cross-section ($\sqrt{\Delta RCS}$), which is the complex-valued difference of the tag's two radar cross-sections (RCSs) that are used for backscatter communication. In contrast to the well-known delta radar cross-section (ΔRCS), which is based on power quantities, the $\sqrt{\Delta RCS}$ is based on field quantities and includes phase information. While the ΔRCS of UHF RFID tags was a quantity of interest in many research activities [18–24] and comprehensive investigations were done, the $\sqrt{\Delta RCS}$ was only addressed in [22, 24] but not in the context of the dependency on (θ, ϕ) . In addition, the authors in [22, 24] propose a measurement system that utilizes a sophisticated carrier cancellation at the expense of non-off-the-shelf hardware. Furthermore, they cannot perform full-sphere measurements, and do not consider tagged objects.

1.3 Objectives

The aim of this thesis is to develop a measurement system capable of determining the $\sqrt{\Delta RCS}$ of passive UHF RFID tags, either in free space or attached to objects, on the entire sphere.

The specific objectives are to:

- implement a measurement system based on mono-/bistatic arrangements in the anechoic chamber.
 - The hardware setup shall constitute exclusively off-the-shelf hardware.
 - Its performance is to be evaluated on predefined metrics: the duration per measurement sample, the hardware complexity, the maximum power density at the tag, and the dynamic range.
- develop a framework enabling the determination of the $\sqrt{\Delta RCS}$ in a spherical coordinate system and resolved onto a spherical polarization basis.
- investigate the application of the spherical wave expansion (SWE) to the $\sqrt{\Delta}RCS$ data, enabling an continuous field reconstruction from measurements.
- study the dependency on the spherical direction of tagged objects in applied scenarios.



1. Introduction 4

Achieving this objectives will contribute by providing a measurement system to gather the $\sqrt{\Delta RCS}$ of tagged objects on the entire sphere to refine in a further step phase-based localization models to increase their accuracy.

Thesis Structure 1.4

The rest of this document is organized as follows:

• Chapter 2: RFID, RCS, and Antenna Measurements – introduces the three fundamental topics, RFID, RCS, and antenna measurements, which together form the basis of this thesis.

- Chapter 3: $\sqrt{\Delta RCS}$ Characterization Method is devoted to the implementation of the $\sqrt{\Delta RCS}$ characterization method.
- Chapter 4: Results presents the results obtained by the implemented $\sqrt{\Delta RCS}$ characterization method.
- Chapter 5: Expansion to the Full Sphere expands the $\sqrt{\Delta RCS}$ to the entire sphere by the utilization of the SWE [25] and pattern stitching [26]. Moreover, applied scenarios of tagged objects are presented.
- Chapter 6: Conclusion draws a conclusion.



Chapter 2

RFID, RCS, and Antenna Measurements

This chapter introduces three fundamental topics that form the basis of this thesis: RFID, RCS, and antenna measurements. Although addressed individually, these topics are deeply related since RFID technology is based on backscatter modulation. In turn, scattering properties of an antenna and, consequently, RFID tags, are defined by RCS parameters and revealed in RCS measurements. To close the circle, RCS measurements are linked to antenna measurements as they share instrumentation, test facilities, and fundamental concepts.

In Section 2.1, a brief introduction to the RFID system operation, comprising core components, passive vs. active tags, operating frequency, reader-to-tag (R \Rightarrow T) and tag-to-reader (T⇒R) communication, is given. In Section 2.2, the IEEE definition of the RCS is presented followed by the definition of the ΔRCS and the derivation of the $\sqrt{\Delta RCS}$. This chapter closes in Section 2.3 with discussing fundamental concepts such as field regions, measurement coordinate systems, polarization, gain, as well as test ranges, with a focus on the utilized in-house range.

2.1RFID System Operation

2.1.1 Core Components

An RFID system consists of at least two elements, a reading device (the reader or interrogator) and an information carrying device (the tag) [6]:

- Reader: A reader is an RF transceiver together with a digital section connected to an antenna and may be mobile or stationary. A stationary reader is mounted on walls, doors, or other objects and is typically connected to a host computer via Ethernet which simultaneously provides energy trough power over Ethernet (PoE). The host computer is used to store the data from the reader but also to allow the user to control the reader. In contrary, a mobile reader is a battery-powered handheld device typically with an integrated user interface to allow the user to control the reader and, as well as the stationary reader, it includes a digital section and an RF transceiver connected to an antenna.
- Tag: A tag is composed of an antenna, oftentimes in planar meander-shaped form, and a small integrated circuit (IC) mounted on a substrate. In turn, the IC comprises three main elements, an analog interface, a digital section, and a memory. The computation possibilities of the IC are very limited to a few operations such as responding to a query command, and reading from or writing to the memory.

Note that various terms are often used interchangeably in the context of RFID tags: RFID

inlay, RFID label, and RFID tag. They are not the same and differ in their construction, because the RFID inlay is the bare antenna and chip mounted on a substrate, while the RFID label embeds the inlay but with an additional printed layer on which barcodes, text or graphics can be added (like the typical RFID price label on garments) and the RFID tag embeds the RFID inlay in a (possibly hard plastic) housing. While the RFID tag is a standalone product, the RFID inlay and RFID label are designed to be attached to other objects.

2.1.2Passive vs. Active

RFID tags can be categorized in passive, semi-passive, and active, dependent whether they use a internal power source and/or RF transceiver or not. While a passive tag costs in the orders of cents, semi-passive and active tags increases this cost significantly [6]:

- Passive: Passive tags have no onboard power source and harvest their operating energy entirely from the RF carrier provided by the reader. The advantage of a passive tag is its simplicity and it needs no maintenance.
- Semi-passive: Semi-passive tags are battery-powered but like passive tags do not initiate communication with readers and rely on backscatter modulation. Semi-passive tags can achieve reading ranges up to 100 m but come with increased maintenance cost since the battery needs to be renewed from time to time.
- Active: An active tag is a fully-developed battery-powered RF transceiver. It can generate an RF carrier signal using a local oscillator and a crystal reference. With on-board amplification and filtering to provide good read sensitivity, the read range can be extended to hundreds of meters. The maintenance cost is increased for the same reason as for the semi-passive tag.

R⇒T Communication

This work will deal with the EPCglobal EPC RFID Air Interface Specification Class 1 Generation 2 [8], henceforth EPC Gen 2. The EPC Gen 2 specifies the air interface of passive UHF RFID systems and was developed by EPCglobal¹.

A passive RFID tag harvests its operating power from the RF carrier (CW signal) provided by the reader. To accomplish this, the induced voltage at the tag antenna terminals is forwarded to the analog interface where it is rectified and stabilized, and then provided to the digital section which consists of a very simple microprocessor or a finite state machine (FSM) used for the implementation of the protocol stack. Nevertheless, providing the operating power is not the only task of the reader, besides that, it must also establish communication with the tag. As outlined in Figure 2.1, adapted from [8], a communication for a single tag and response comprises the following sequences. The reader shall not issue commands before the end of the maximum settling-time interval, i.e., before T_s . Afterwards, it sends a query command by modulating the RF carrier accordingly, using an amplitude shift keying (ASK) or binary phase shift keying (BPSK) modulation format. After the transmission of the query, the reader continues providing an unmodulated RF carrier. The tag recognizes the query and replies with a T⇒R preamble and a random number 16-bit (RN16) if the decoding of the query was successful. The reader then acknowledges its reception by sending another message including the received RN16 and the tag replies with

¹Note that the EPC Gen 2 was adopted by the international organization for standardization (ISO) as ISO 18000-6C. Both forms can be found on datasheets interchangeably.

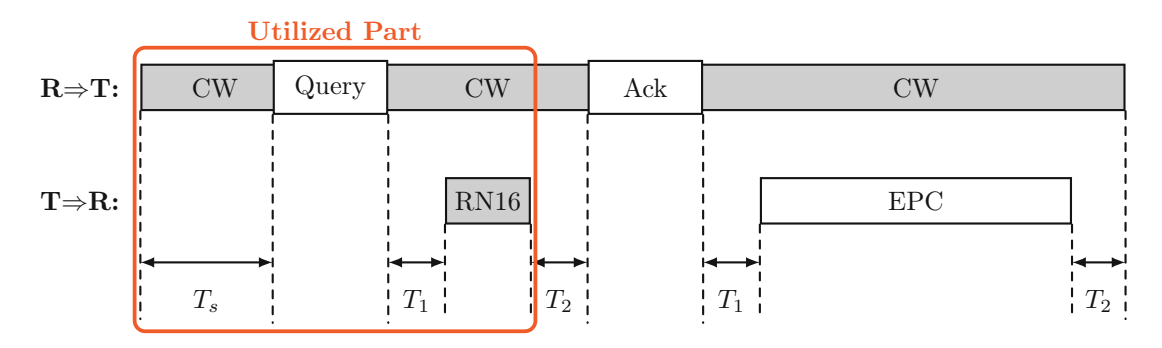


Figure 2.1: Link timing for a single tag and response [8] together with the indication of the utilized part in this work.

its EPC. If the EPC received at the reader is valid, user selected commands can follow. This communication principle is also known as interrogator-talks-first and besides that the communication is half-duplex meaning that interrogators talk and tags listen or vice versa. The time intervals T_1 and T_2 denote the tag and reader response times, respectively. Moreover, the utilized part for the work at hand is indicated in orange. Including the EPC in the measurements would result in a higher accuracy of the $\sqrt{\Delta RCS}$, because of its significant longer duration compared to the RN16 (96 bits vs. 16 bits). Nevertheless, it would require that the measurement system is capable of responding to the RN16 and since the ACK incorporates the RN16, it would require to actually establish $R \Rightarrow T/T \Rightarrow R$ communication in each tag reading. This would come at the expense of non-off-the-shelf hardware, which is against the objectives, and therefore, not accomplished.

2.1.4 $T\Rightarrow R$ Communication

Data transmission via backscatter modulation is achieved by altering the load Z_l presented to the tag antenna by switching the additional impedance Z_{mod} on and off in accordance with data to be transmitted [1]. To illustrate this, in Figure 2.2 the equivalent circuit representation of a passive tag based on backscatter modulation is shown. The switch is typically realized as a modulation transistor. In the unmodulated state (switch open) the tag antenna "sees" the impedance of the chip Z_{chip} , whereas in the modulated state (switch closed) the antenna sees the parallel impedance $Z_{\text{chip}}||Z_{\text{mod}}$. The RCS of loaded antennas has been expressed by Green [27] as cited in [28] as

$$\sigma = \frac{\lambda^2 G^2}{4\pi} |C + \Gamma|^2 , \qquad (2.1)$$

where λ is the wavelength (in m) and G is the antenna gain (dimensionless on linear scale). The load-independent complex-valued constant C (dimensionless) is introduced by the currents induced on the surface of the antenna by the incident wave (structural mode). The antenna load mismatch (antenna mode) is denoted by Γ and defined as modified current reflection coefficient (dimensionless) as

$$\Gamma = \frac{Z_a^* - Z_l}{Z_a + Z_l} \ . \tag{2.2}$$

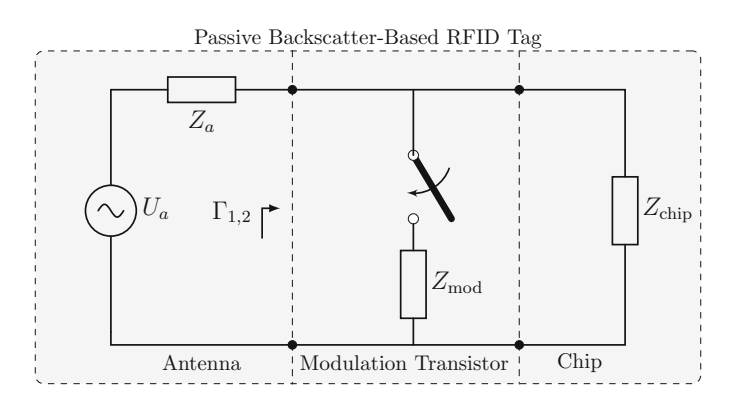


Figure 2.2: Equivalent circuit of a passive tag based on backscatter modulation [1].

Scalar ΔRCS of Tags

To assess the tag modulation, (2.1) needs to be modified to include both modulation states, since the tag exhibits a RCS even if it is not modulating hence

$$\Delta \sigma_{\text{scalar}} := \sigma_1 - \sigma_2 = \frac{\lambda^2 G^2}{4\pi} \left(|C + \Gamma_1|^2 - |C + \Gamma_2|^2 \right) . \tag{2.3}$$

Equation (2.3) suffers from the disadvantage that it is the mere difference of two scalar RCS values and it might be the case that both modulation states produce the same RCS value, thus a zero $\Delta \sigma_{\text{scalar}}$ although the tag is modulating. Therefore, (2.3) needs to be reformulated to utilize a vector difference of the modulation states Γ_1 and Γ_2 instead of a scalar difference.

Vector ΔRCS of Tags

By taking the square $root^2$ of (2.1) to keep the phase:

$$\sqrt{\sigma} = \frac{\lambda G}{\sqrt{4\pi}} \left(C + \Gamma \right) , \qquad (2.4)$$

where $\sqrt{\sigma}$ is the complex-valued square root radar cross-section (\sqrt{RCS}). Following (2.3), the difference of the modulation states must be taken to assess the tag modulation hence

$$\sqrt{\Delta \sigma} := \sqrt{\sigma_1} - \sqrt{\sigma_2} = \frac{\lambda G}{\sqrt{4\pi}} \left(\Gamma_1 - \Gamma_2 \right) , \qquad (2.5)$$

where $\sqrt{\Delta\sigma}$ denotes the square root delta radar cross-section ($\sqrt{\Delta RCS}$) and takes the vector difference of the complex-valued modulation states $\Delta\Gamma := \Gamma_1 - \Gamma_2$ into account. Note that in (2.5), the load-independent part vanishes. By squaring (2.5), the well-known vector ΔRCS [18] can be obtained:

$$\Delta \sigma_{\text{vector}} = \frac{\lambda^2 G^2}{4\pi} |\Delta \Gamma|^2 \ . \tag{2.6}$$



²From the microwave transmission line theory [29] it is known that (complex-valued) voltages and currents (u,i) on transmission lines can be represented by forward and backward traveling (complex-valued) power waves (a, b) which are field quantities, and moreover, from these power waves, the power delivered to and reflected from the load can be determined by $P_{inc} = |a|^2/2$ and $P_{rev} = |b|^2/2$. Simply put, complex-valued field quantities are related to real-valued power quantities by simply squaring. Conversely, field quantities can be derived from power quantities by taking the square root. Note that not the square root is being extracted, but simply a representation based on field quantities which are derived from the square root of power quantities.

Now, it is known how the RCS is related to the tag modulation. The next step is to present how the RCS can be expressed by measurable parameters, since the parameters Γ_1 , Γ_2 , and G are typically unknown from the customer's perspective.

From RCS to Δ RCS to $\sqrt{\Delta}$ RCS 2.2

First, the definition of the RCS based on the IEEE Standard for Radar Definitions [30] is presented. Afterwards, the radar equation [31] for a bistatic radar is derived, which acts as the basis for the $\triangle RCS$ and $\sqrt{\triangle RCS}$ relations.

2.2.1Definition RCS IEEE

The IEEE Standard for Radar Definitions [30] provides a formal definition of the RCS

$$\sigma = \lim_{r \to \infty} 4\pi r^2 \frac{S_r}{S_i} \,, \tag{2.7}$$

where S_i is the incident power density at the scattering target (in W/m²), and S_r the scattered power density (in W/m^2) observed at distance r (in m). In [32] an intuitive description of (2.7) is presented: Let the incident power density at the scattering target from a distant radar be S_i . The amount of power intercepted by the target is then related to its cross-section σ (in m²), so that the intercepted power is σS_i (in W). This intercepted power is then either re-radiated as scattered power or absorbed as heat. Assuming it is entirely re-radiated, and moreover, uniformly in all 4π steradian of space, then the scattered power density S_r at a certain distance R is

$$S_r = \frac{\sigma S_i}{4\pi R^2} \ . \tag{2.8}$$

An alternative but equivalent description of the RCS is in terms of the radar equation in [31]. It can be derived, for example, for a bistatic radar with polarization-matched directional antennas in the far-field by using (2.8) as starting point and substituting the relationships for S_i and S_r . Note that although Skolnik [31] expressed the radar equation for a monostatic radar, the extension to the bistatic case is straightforward. The incident power density at the scattering target from a radar transmitter at a distance R_{tx} reads [31]

$$S_i = \frac{P_{tx}G_{tx}}{4\pi R_{tx}^2} \,, (2.9)$$

where P_{tx} is the power at the transmit antenna terminals and G_{tx} is the gain of the transmit antenna. Further, the received power at the radar receiver is determined by [31]

$$P_r = S_r A_e (2.10)$$

where an effective Area A_e is introduced. Substituting (2.9) and (2.10) into (2.8) becomes

$$P_{rx} = \frac{\sigma\left(\frac{P_{tx}G_{tx}}{4\pi R_{tx}^2}\right)}{4\pi R_{rx}^2} A_e , \qquad (2.11)$$

considering now a differentiation between transmit and receive distances $R = R_{rx}$ Skolnik. [31] provides further a relationship between the transmitting gain and the receiving effective area

$$A_e = \frac{\lambda^2 G}{4\pi} \ . \tag{2.12}$$



Embedding (2.12) in (2.11) and reformulating for σ eventually yields

$$\sigma = \frac{P_{rx}}{P_{tx}} \frac{4\pi}{G_{tx}G_{rx}} \left(\frac{4\pi R_{tx}R_{rx}}{\lambda}\right)^2 . \tag{2.13}$$

Having (2.13) at hand, the ΔRCS is presented in the following.

2.2.2Definition $\triangle RCS$

Utilizing (2.13) but embedding the power difference at the receiving antenna because of the tag's two modulations states yields [18]

$$\Delta \sigma = \frac{\Delta P_{rx}}{P_{tx}} \frac{4\pi}{G_{tx}G_{rx}} \left(\frac{4\pi R_{tx}R_{rx}}{\lambda}\right)^2 . \tag{2.14}$$

Derivation $\sqrt{\Delta RCS}$ 2.2.3

By taking the square root of (2.14)

$$\sqrt{\Delta\sigma} = \frac{\Delta w}{v} \sqrt{\frac{4\pi}{G_{tx}G_{rx}}} \left(\frac{4\pi R_{tx}R_{rx}}{\lambda}\right) . \tag{2.15}$$

where $\Delta w := \sqrt{\Delta P_{rx}}$ and $v := \sqrt{P_{tx}}$ are complex-valued power waves, and moreover, Δw is the complex-valued difference of the backscattered fields at the receiving antenna due to the tag's two modulation states. Throughout the thesis Δw is denoted as the delta tag response and its computation from measurement results will play an important role in the determination of the $\sqrt{\Delta}$ RCS.

Comparing (2.5) with (2.15) reveals that the latter is practically tractable because the parameters can either be determined from the measurement system or obtained by measurements but to not require information from the tag manufacturer about the tag antenna gain or the modulation states. Nevertheless, (2.15) does neither incorporate the spherical direction nor the polarization basis. Achieving this, the $\sqrt{\Delta RCS}$ will be revised once more in Section 3.5.

2.3RCS and Antenna Measurements

2.3.1 **Fundamental Parameters**

Starting with the definition of an antenna. An antenna is a means for radiating or receiving electromagnetic waves [33]. Simply put, an antenna is a two port with a certain behavior with respect to gain, efficiency, polarization, input impedance, radiation pattern, bandwidth and more, and connects a waveguide and a RF signal generator at the input and free space, where waves are outgoing or incoming, at the output. The field distribution of an outgoing wave is dependent on the distance to the antenna, therefore, the field regions are discussed next.

Field Regions

The space surrounding an antenna is subdivided into three regions [34]:



- Reactive near-field region: Defined as the portion of the near-field region immediately surrounding the antenna wherein the reactive field predominates, i.e., the energy is stored very near to the antenna surface, rather than radiated outwards. The reactive field contribution decays fast with increasing distance and as a rule of thumb, the outer boundary of this region is at a distance $R < 0.62\sqrt{D^3/\lambda}$ from the antenna surface, where D is the largest dimension of the antenna and λ is the wavelength.
- Radiative near-field (Fresnel) region: The transition region where the phases of the electric field (E-field) and the magnetic field (H-field) approach from out-of-phase to in-phase, which causes the formation of a time-average power flow in the radial direction, i.e., the radiative field predominates over the reactive field. The inner boundary of this region is at a distance $R \geq 0.62\sqrt{D^3/\lambda}$ where again D is the largest³ dimension of the antenna and λ is the wavelength and the outer boundary of this region is at a distance $R < 2D^2/\lambda$.
- Far-field (Fraunhofer) region: This region is defined at distances $R \ge 2D^2/\lambda$. The E-field and H-field components are in-phase, perpendicular to each other, and transverse to the radial direction of propagation. In this region, the field distribution is not a function of the distance R anymore.

Radiation Pattern

The radiation or antenna pattern [34] is defined as the representation of the radiation properties of an antenna as a function of the spatial direction. Such properties include the radiation intensity, field strength, gain, directivity, phase or polarization. Typically the patterns are visualized in two or three dimensional rectangular, polar or spherical plots. However, for any radiation pattern to be meaningful, a coordinate system and a polarization basis must be defined.

Coordinate System

A coordinate system leverages to describe a point in space and in the case of antenna measurements it is important to differentiate between the measurement coordinate system and the plotting coordinate system [35]. That is, the measurement coordinate system is related to the mechanical movement of the positioner system, where the probe antenna and the antenna under test (AUT) are mounted, and the plotting coordinate system is the coordinate system in which the radiation pattern is visualized. Since mathematical transformations exist, both not need to be identical. However, the three types of spherical coordinate systems which are supported by typical positioner systems are:

- Azimuth over elevation $\mathbf{r}(r, \mathrm{Az}, \mathrm{El})$
- Elevation over azimuth $\mathbf{r}(r, \text{El, Az})$
- Spherical $(\theta \phi)$ $\mathbf{r}(r, \theta, \phi)$

Plotting coordinate systems include these three types of coordinate systems, but also extend them, by introducing alternative forms (e.g., true-view, direction cosine, Arcsinespace) which do not necessarily have direct analogy to the positioner system, but can potentially offer advantages when interpreting the data. For the work at hand the spherical

³To be valid, D must also be large compared to the wavelength $(D > \lambda)$

 $(\theta - \phi)$ coordinate system will be used for the visualization as it matches the measurement coordinate system of the utilized range.

Polarization Basis

The polarization describes the orientation of the E-field on a plane perpendicular to the propagation direction and is a far-field property. In contrary to the near-field, where three vector components are required to describe the E-field, in the far-field, the third component, parallel to the propagation direction, vanishes (is identically zero) and hence the E-field can be expressed with respect to a chosen polarization basis based on a pair of orthogonal unit vectors [35]:

 Cartesian polarization basis (Ludwig I): The cartesian polarization basis corresponds to resolving the E-field onto three unit vectors $(\mathbf{e}_x, \mathbf{e}_y, \mathbf{e}_z)$ aligned with each of the three cartesian axes x, y, z defined by the positioner system. The E-field can be expressed as

$$\mathbf{E}(\mathbf{r}) = E_x(\mathbf{r})\mathbf{e}_x + E_y(\mathbf{r})\mathbf{e}_y + E_z(\mathbf{r})\mathbf{e}_z . \tag{2.16}$$

In the far-field, the component parallel to the propagating direction vanishes.

- Spherical polarization basis (Ludwig II): If instead the E-field is resolved onto a spherical polarization basis, it allows for the definition of three further polarization bases, each corresponding to placing the pole along the y-, x-, or z-axes, respectively:
 - Azimuth over elevation polarization basis (Ludwig II-1)
 - Elevation over azimuth polarization basis (Ludwig II-2)
 - Spherical polarization basis $(\theta \phi)$:

$$\mathbf{E}(\theta,\phi) = E_{\theta}(\theta,\phi)\mathbf{e}_{\theta}(\theta,\phi) + E_{\phi}(\theta,\phi)\mathbf{e}_{\phi}(\theta,\phi) . \tag{2.17}$$

• Co-polar and cross-polar polarization basis (Ludwig III): Taking the orientation of the probe and the AUT on the positioner system into account. The co-polarization is the component measured when the probe is aligned with the AUT's main polarization and the cross-polarization is measured when the probe is rotated by 90°.

$$\mathbf{E}(\theta, \phi) = E_{\text{co}}(\theta, \phi)\mathbf{e}_{\text{co}}(\theta, \phi) + E_{\text{cross}}(\theta, \phi)\mathbf{e}_{\text{cross}}(\theta, \phi) . \tag{2.18}$$

The relationship of the individual polarization components, i.e., for example, in a spherical polarization basis can be represented as:

- Linear polarization: $E_{\theta}(\theta, \phi) = 0$ or $E_{\phi}(\theta, \phi) = 0$.
- Circular polarization: $E_{\theta}(\theta, \phi) = E_{\phi}(\theta, \phi)$.
- Elliptical polarization: $E_{\theta}(\theta, \phi) \neq E_{\phi}(\theta, \phi)$.

Gain

The qain $G = G(\theta, \phi)$ [33] is defined as the ratio of the radiation intensity in a given direction relative to the radiation intensity that would be obtained if the power accepted by the antenna were radiated isotropically. In further accordance, the partial gain $g_{\chi} = g_{\chi}(\theta, \phi)$ is defined for a polarization component χ .



Monostatic / Bistatic Arrangement

A radar system distinguishes between monostatic and bistatic arrangement [36]. That is, in a monostatic arrangement the TX antenna is also the receive (RX) antenna, or if two seperate antennas are used, TX and RX antenna are co-located. In this case, the spherical direction relative to the target for both, the TX and RX antenna, are identical. However, if the TX and RX antenna are not co-located, the arrangement is referred to be bistatic.

2.3.2 Test Ranges

A prerequisite for an accurate characterization of the AUT is a well known environment, called antenna test range [37]. Such ranges have been developed to measure the far-field radiation pattern of an AUT independent of their operational environment, i.e., without external influences. A test range consists of the required instrumentation as well as the physical space required for the measurements. A basic instrumentation equipment includes the test antenna (the probe), the positioner system, the transmit/receive RF system, and a workstation. The movement of the probe and the AUT is controlled by the positioner system which in turn receives the commands from the workstation. The transmit RF system provides a stimulus and the receive RF system detects the AUT response at various spherical directions. The measurement data is provided to the workstation which does then the further data processing. The IEEE [37] recommends a classification into three basic types of ranges:

- Free-space ranges: Are designed to mimic free space and far-field conditions. That is, all the effects of the surroundings are suppressed to acceptable levels. The most commonly encountered free-space ranges are anechoic chambers, elevated ranges, and the compact range. The former and latter are indoor ranges, whereas the elevated range is an outdoor range. In outdoor ranges the probe and the AUT are mounted above the ground, for example on towers, buildings, mountains, or wherever one can establish an unobstructed line of sight (LOS). It is evident, that environmental influences cannot be eliminated and thus the accuracy of the measurements suffers. However, the main reason for outdoor ranges is that far-field conditions can easily established, whereas in indoor ranges there is often not enough separation to achieve this. However with the development of compact ranges which make use of a reflector whose shape is designed to reflect the spherical waves in an approximate planar manner and thus establishing far-field conditions.
- Ground reflection ranges: The idea is similar to that of compact ranges, to allow for reflections to produce an approximate plane wave.
- Near-field ranges: This type of range allows for conducting the measurements in the radiative near-field of the AUT and subsequently transform the near-field data to far-field. Typically, planar, cylindrical and spherical coordinate systems are utilized to conduct the measurement. Such systems are preferred because the vector Helmholtz equation is separable in each of these coordinates, and moreover, the positioner system that perform rotations of the antennas can be easily constructed. The utilization of the SWE to solve the Helmholtz equation in the respective coordinate system allows then the computation of the far-field pattern. Near-field antenna measurements have become a well-established technique and especially the spherical near-field antenna measurement technique is seen as state-of-the-art for high accuracy antenna measurements [38] because it samples on a closed surface surrounding the AUT and capturing the radiation of the AUT on the entire sphere.

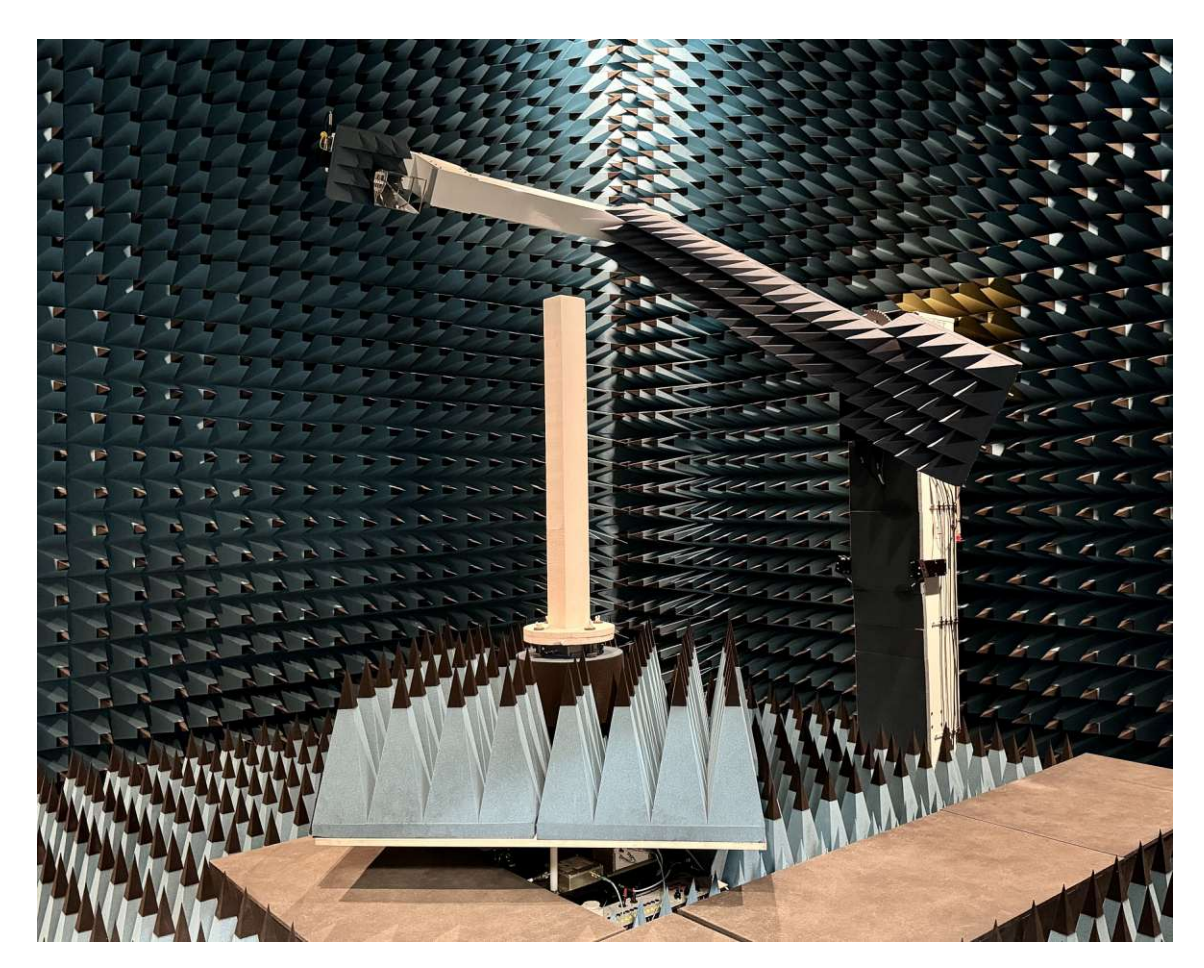


Figure 2.3: Spherical near-field test range at TU Wien.

2.3.3 Test Range at TU Wien

The remainder of this work is devoted to the in-house spherical near-field test range from NSI-MI technologies [39]. It is a spherical test range and realized as a swing arm-overazimuth range with the polar angle θ , azimuth angle ϕ , and polar axis in z-direction, depicted in Figure 2.3. The probe antenna mounted on top of the θ -stage, is a highdirectivity dual-ridge horn antenna (DRHA) in linear polarization pointing towards the center of the sphere and is either used as TX or RX antenna. It can be rotated to permit measurements of both polarization components. The polarization angle is denoted as χ . The ϕ -rotations (360° rotations permitted) are done with the azimuth positioner (ϕ -stage) at the base of the anechoic chamber. To mount the AUT in the center of the measurement sphere, a support structure of appropriate height, mounted on the ϕ -stage, is needed. A glance at Figure 2.3 reveals that it is not possible to cover the entire sphere within a single measurement. The swing arm (θ -stage) is designed for a deflection $0 < |\theta| < 160^{\circ}$, however, because the additional absorbers are placed on the ϕ -stage the maximum deflection is $\theta_{\rm trunc} = 140^{\circ}$. The additional absorbers reduce reflections from the ϕ -stage, which is especially in the case of low-gain omnidirectional tag antennas important. Since pattern stitching must be use anyways to determine full-sphere field data more truncation is accepted.

Tag Support Structure

Two different support structures are utilized, which are both from the Rohacell family [40]. These are intended to resemble the dielectric properties of air as close as possible. The first structure is made from Rohacell 31 IG foam. It provides a large surface such that tagged objects can be placed on it. Further, the structure can be layered with smaller pieces of Rohacell such that flexible heights of the support structure can be achieved. Tape is used to secure the positioning. The second structure is made from Rohacell 31 HF foam [40] and its surface is compact with the focus to fit specifically for connectorless AUTs and in this work, for tags in free space. It cannot be layered. Both structures were developed as part of the PhD thesis in [26]. Dust, glue, and tape have impact on the path performance, however, knowing the exact behavior is not necessary because, for the same reasons as above, it is compensated by a two-step calibration procedure presented in Section 3.5.

Bi-Directional and Equiangular Sampling

The radiated field of the antenna is measured at discrete points on the measurement sphere. Since the utilized range is a spherical $(\theta - \phi)$ range the measurement samples are taken for discrete values of the θ and ϕ angles of the measurement coordinate system. Without any further knowledge about the AUT, for example, if it possess some rotational symmetry the sampling step sizes in θ and in ϕ are identical. Equiangularly sampled data is also a prerequisite pattern stitching, presented in Chapter 5, therefore, in this work, regardless of the AUT sampling is performed θ and in ϕ identically. In spherical near-field measurements (which holds also true for far-field measurements) the sampling increment is given by [25]

$$\Delta_{\theta\phi} = \frac{2\pi}{2N+1} \ . \tag{2.19}$$

The mode order $N = |kr_0| + n_1$ describes the fastest phase variation of the AUT that can occur, and thereby defines the sampling increment, where $k = 2\pi/\lambda$ is the wavenumber (in 1/m), r_0 the radius (in m) of the smallest sphere with center at the origin fully enclosing the AUT and the integer n_1 . Hansen [25] suggests that $n_1 = 10$ is sufficient for most practical cases. The mode order will be addressed in detail in Chapter 5. To capture both polarization components at each sampling point two probe orientations

$$\chi = \left[0, \frac{\pi}{2}\right] , \qquad (2.20)$$

are used. These relations are used throughout the thesis to determine the sampling step size of the tagged object under test. Moreover, bi-directional sampling is pursed that is the measurements are taken in both directions starting from $\chi = \theta = \phi = 0^{\circ}$. In the case of a rotation in ϕ the measurements are taken from 0° to 360° , and then again from 360° to 0° for the next θ step, without prior moving back to 0°, until $\theta = 140^{\circ}$ is reached. Consequently for the second polarization the measurements are taken in θ from 140° to 0°. If instead uni-directional scanning is pursued, the measurements are solely taken from 0° to 360° in ϕ and from 0° to 140° in θ .

Chapter 3

$\Delta {f RCS}$ Characterization Method

This chapter starts with presenting the elaborated antenna arrangements on the spherical positioner system in the anechoic chamber in a systematic manner, in Section 3.1. Afterwards, functional blocks of the measurement setup are explained in Section 3.2 and combined into a complete setup in Section 3.3. Data acquisition and processing are addressed in Section 3.4. Note that the $\sqrt{\Delta RCS}$ itself is a characteristic and is not directly accessible via measurements, i.e., its value needs to be determined in post-processing. Therefore, a comprehensive formal treatment, provided in Section 3.5, is required. It allows the determination of the $\sqrt{\Delta RCS}$ from measurements and a calibration procedure. The chapter closes in Section 3.6 with the link budget.

3.1Antenna Arrangements

This section elaborates on different concepts of the antenna arrangement in the anechoic chamber and starts with a monostatic approach known from the literature. Then, a bistatic approach is presented, which allows for three different configurations which are investigated throughout the thesis.

Monostatic 3.1.1

Research has demonstrated [22, 24, 41], that in a monostatic arrangement, self-interference is a challenge. Figure 3.1 illustrates an exemplary monostatic scenario adapted to the utilized range where the anechoic chamber and the spherical positioner system are depicted as abstraction of the side view of Figure 2.3. That is, the probe antenna mounted on top of the θ -stage tests the tag, which is positioned in the center of the measurement sphere, by utilizing a support structure, of appropriate height, mounted on the ϕ -stage. Transmit and receive paths are decoupled outside the anechoic chamber via a circulator. The exact implementation of the transmitter and the receiver is not discussed now but in Section 3.2, instead it is assumed that the transmitter is capable of successfully activating the tag and the receiver is capable of measuring the received signal. The solid red line illustrates the TX signal (RF carrier followed by the query command), the solid green line visualizes the wanted backscatter response from the tag, and the dashed red line illustrates the unwanted self-interference. Although the individual signal components are drawn as separate lines, it is a single line connecting the circulator with the probe and a single line connecting the circulator with the receiver.

Self-interference occurs when a transmitted signal leaks into the receiver, due to nonideal elements on the TX path, and it becomes severe when:

- (i) The transmitter and the receiver operate at the same time.
- (ii) The transmitted and the received signal are within the same frequency range.

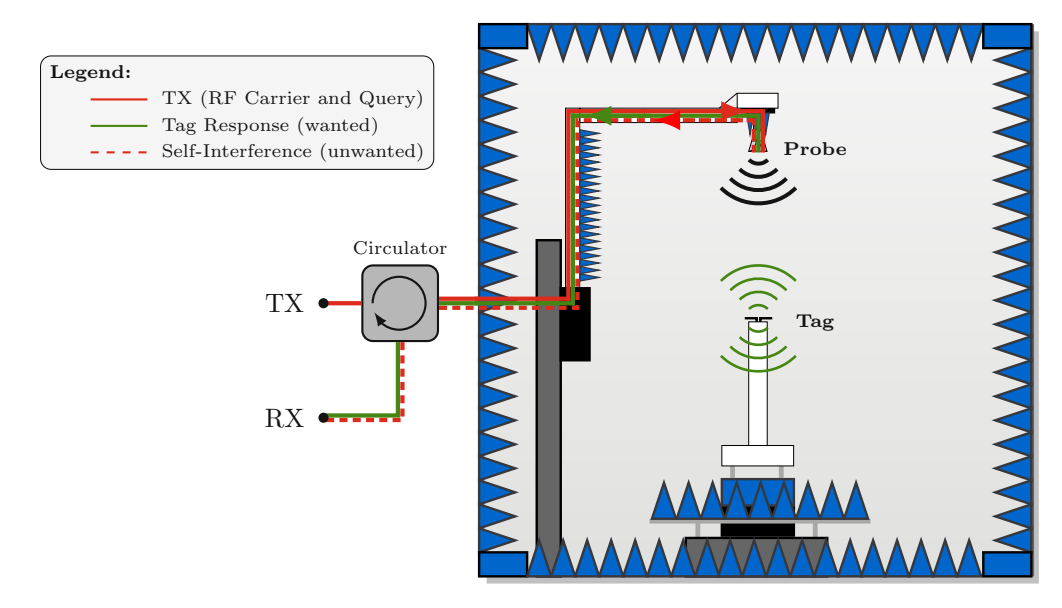


Figure 3.1: Exemplary monostatic arrangement adapted to the utilized test range. The probe is assigned the TX and the RX antenna.

(iii) The transmitted signal is predominant compared to the received signal.

This is exactly what happens in RFID systems. The tag, while backscattering, necessitates an RF carrier from the transmitter, which is orders of magnitudes stronger than the backscatter signal, and moreover, backscattering occurs on a subcarrier of the RF carrier, i. e., the receiver cannot simply filter out the unwanted RF carrier in favor of the backscatter signal. As a result, the dominant RF carrier overwhelms the receiver and drives its frontend components (amplifier, mixer, analog-to-digital converter, ...) into saturation. The receiver counteracts by attenuating the overall signal causing that the anyway weak backscatter signal cannot be recovered due to an insufficient signal-to-noise ratio (SNR). The challenge of self-interference is well known and commercial RFID systems employ carrier cancellation to tackle this issue. The carrier cancellation system injects a phase-inverted copy of the RF carrier into the receiver which is then added to the received backscatter signal. This is not trivial because it requires a control-loop to find the optimal amplitude and phase to minimize the residual leakage. Moreover, this process must be repeated for each reading of the tag, due to the varying reflections when moving with the positioner system. Besides that carrier cancellation requires non-off-the-shelf hardware. To mitigate the self-interference, without using the carrier cancellation, the idea is to employ a bistatic arrangement. By utilizing two antennas the transmit and receive paths can already be decoupled in the anechoic chamber which inherently reduces the amount of self-interference.

3.1.2Configuration Probe-TX

This arrangement, denoted as configuration Probe-TX and visualized in Figure 3.2, uses the probe as the TX antenna and the second antenna, denoted as the pickup antenna, as the RX antenna. The pickup antenna is placed on the ϕ -stage below the tag support structure. In principle, the pickup antenna could be placed at any location in the anechoic chamber, but a location in short distance to the tag, and further, where the relative position between the pickup antenna and the tag is fixed during the rotation of the ϕ -stage is in favor because it enables that the coupling between them is constant and consequently (χ, θ, ϕ) -independent. Simply put, after the placement of the pickup antenna and the tag,

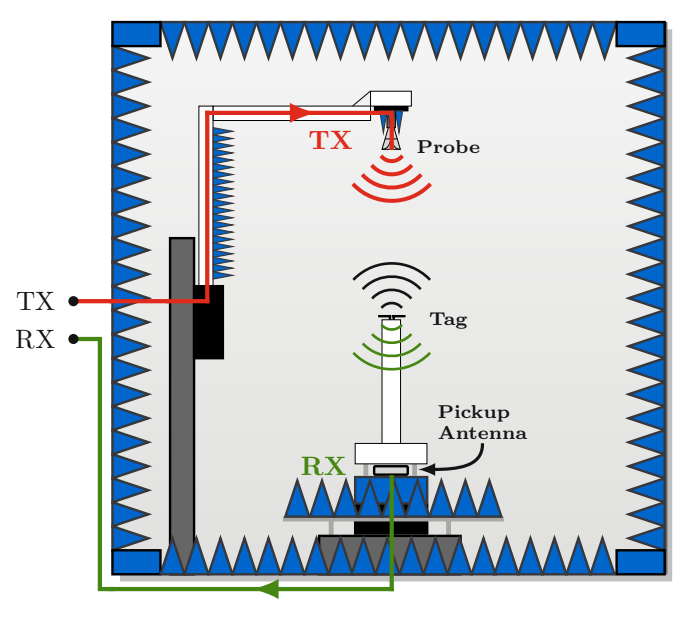


Figure 3.2: The bistatic configuration Probe-TX assigns the probe the TX and the pickup antenna the RX antenna.

the coupling between both antennas is set and the link loss maintained during the entire measurement. Moreover, by using a right handed circular polarized pickup antenna¹, the link quality becomes independent on the relative orientation of the pickup antenna and the tag which enables a low-loss link without the use of precision instrumentation for a polarization alignment of the antennas. One can think of the coupling between the pickup antenna and the tag as an "extended port" of the tag and this perspective reveals a decent property of this configuration that if the tag can be activated, it is likely that the tag response can also be decoded at the receiver with sufficient SNR.

The internal circuitry of the tag exhibits nonlinear and power-dependent behavior. This means that the tag must be operated at a fixed point with regard to the power wave entering its input stage. Since the path between probe and tag is (χ, θ, ϕ) -dependent and if the radiated power at the probe is kept constant, the power wave entering the input stage is dependent on the (χ, θ, ϕ) -position. To ensure, however, a (χ, θ, ϕ) -independent power wave, a power leveling in which the radiated power at the probe is adjusted accordingly, must be pursued². Depending on the granularity of the power leveling, it becomes evident this process is either time-consuming, for example, if done in 0.1 dB-steps, or not accurate, if done in 1 dB-steps. The need for a power leveling is cumbersome, but it can be bypassed by simply reversing TX and RX. That is, the pickup antenna at the ϕ -stage transmits and the probe at the θ -stage receives, leading to configuration Probe-RX. Note that the measurement setup that will be developed later is not changed in configuration Probe-RX, only the connections to the anechoic chamber are changed.

Configuration Probe-RX 3.1.3

The pickup antenna is used as the TX antenna and the probe as the RX antenna, see Figure 3.3. Due to the TX/RX reversion, the major difference to configuration Probe-TX

¹The antenna pattern was not pre-measured and this is accepted because a two-step calibration procedure presented in Section 3.5 eliminates the need for knowing the pattern.

²See Section 3.4.1 for implementation details of the power leveling.

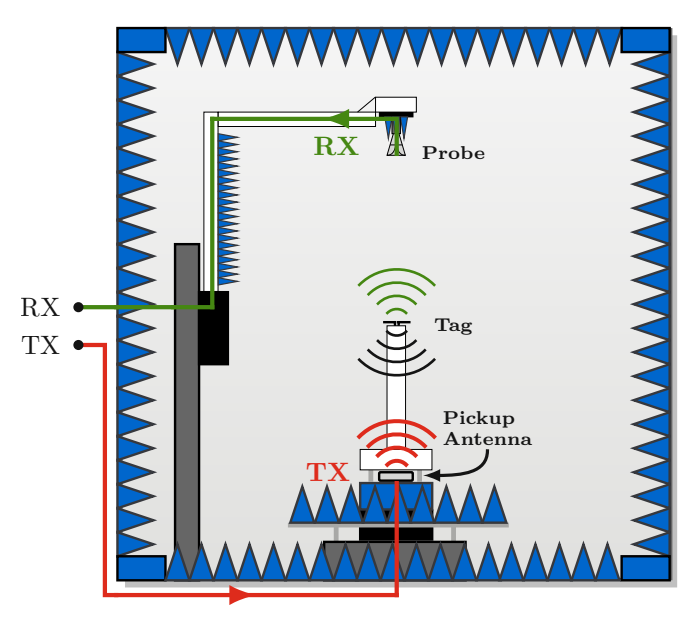


Figure 3.3: The bistatic configuration Probe-RX assigns the pickup antenna the TX and the probe the RX antenna.

is the utilization of the (χ, θ, ϕ) -independent transmit path (cf. extended port perspective). Hence, the power leveling to ensure a fixed tag operating point, needs to be done only once for the entire spherical measurement instead of repeatedly for each individual spherical direction and, moreover, due to the low-loss link it can be guaranteed that the transmitter can provide the power required to wake up the tag. Since now the receive path is (χ, θ, ϕ) dependent it cannot be guaranteed that the SNR at the receiver will be sufficient to decode the tag response. An insufficient SNR causes that a phase ambiguity of 180° in the $\sqrt{\Delta}$ RCS is introduced. Measurements suffering from a fast phase variation cannot be neglected since the determination of truncated spherical wave coefficients (SWCs), introduced in Chapter 5, is sensitive to measurement uncertainties and might cause a nonphysical field distribution. To bypass the decoding, a third configuration, denoted as configuration Probe-RX-C is introduced.

Configuration Probe-RX-C 3.1.4

The probe is assigned the RX antenna and the pickup antenna is assigned the TX and the RX antenna, see Figure 3.4. This configuration is an extension to configuration Probe-RX by simply recording the tag response simultaneously at the probe and the pickup antenna. Compared to the previous configurations, the specific implementations of the transmitter and the receiver are maintained, but it requires an additional receiver and a directional coupler. Since the backscattered response at the pickup antenna is (χ, θ, ϕ) -independent (cf. extended port perspective), it is considered as a reference response. The reference response is then correlated with the backscatter response received at the probe and the result is then embedded in the $\sqrt{\Delta RCS}$. This method has the advantage, that the decoder is bypassed and instead a correlation is carried out without introducing a phase ambiguity. Note that the situation at the pickup antenna is again monostatic and the challenges of such arrangements were presented previously, therefore, the actual performance of this approach is to be determined.

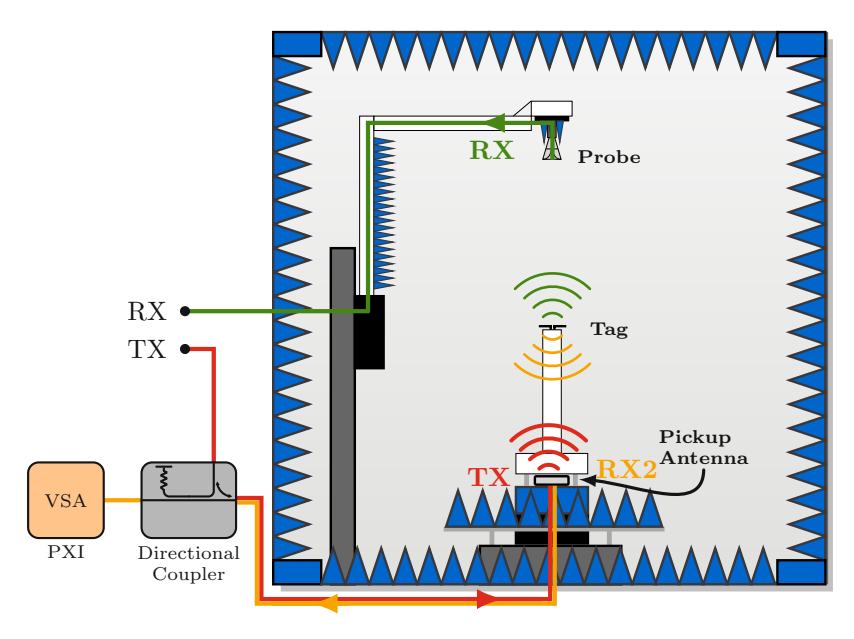


Figure 3.4: The combined monostatic-bistatic configuration Probe-RX-C assigns the probe the RX antenna and the pickup antenna the TX and the RX antenna.

3.2Measurement Setup Blocks

After the antenna arrangement, the measurement setup is described, and although four different arrangements were discussed, it is a single setup to serve them all. The measurement setup is split into key functional blocks: the RF signal generation and modulation block (Section 3.2.1), the measurement instrument (Section 3.2.2), the calibration block (Section 3.2.3), and the sequencer (Section 3.2.4). Each block represents a distinct part of the signal path, and within each block, the requirements on the equipment are defined, and then the component choice is discussed. A systematic list of all equipment can be found in Appendix A.

3.2.1RF Signal Generation and Modulation

As indicated in Figure 2.1 only the part of the $R \Rightarrow T$ and $T \Rightarrow R$ communication until the tag responds with the RN16 is of relevance for this work. Hence the purpose of this block to generate an query command to activate the tag preceded and followed by an unmodulated RF carrier to supply the tag. The utilized equipment in this block is shown in Figure 3.5 and explained in what follows starting with the RF signal source.

RF Signal Source

The tag modulates back on a subcarrier of the RF carrier. Therefore, the phase noise performance of the signal source at the desired backscatter link frequency (BLF) of 640 kHz³ is crucial, as it contributes to the SNR at the BLF. Further, a signal source with an integrated IQ modulator and an arbitrary waveform generator⁴ to generate the RF carrier and the query command within a single instrument, is preferred over a CW-only source, to keep the hardware complexity feasible. The granularity of the power leveling

³The specific choice of the BLF is discussed in Section 3.4.2.

⁴The arbitrary waveform generator allows the generation of custom IQ baseband waveforms, such as the query command which can be either ASK, in the form of on-off keying, or BPSK.

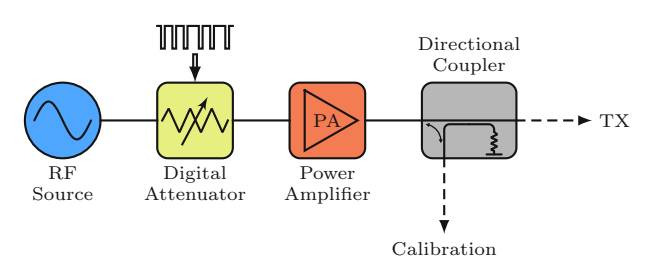


Figure 3.5: Block diagram of the equipment used for RF signal and query command generation.

is bounded by the level resolution of the source suggesting the need for a high level resolution of the source. Measurements revealed that the phase noise performance of the Agilent E8244A PSG, a CW-only source, is better than that of the Rohde & Schwarz SMBV100A, which could perform the modulation. The exact values are $-144\,\mathrm{dBc/Hz}$ at the desired BLF achieved by the former and $-136\,\mathrm{dBc/Hz}$ by the latter. The phase noise performance is considered more important than the others, therefore, the Agilent E8244A PSG was selected and the modulation is done externally with a digital attenuator. The level resolution of the Agilent is 0.01 dB, which is sufficient for the power leveling. The maximum output power of the source was not considered critical because initial link budget evaluations already suggested the need for a power amplifier (PA).

Digital Attenuator

To generate the query command, the RF carrier must be modulated accordingly. Note that the use of an attenuator restricts the R⇒T modulation format to solely ASK modulation. The requirements on the attenuator are given by the EPC Gen 2 [8] and comprise the modulation depth which shall be at least 14dB, the rise and fall times which shall be at maximum $0.33 \cdot \text{Tari}^5$, which gives $2.06 \, \mu \text{s}$, in the case of the smallest Tari of $6.25\,\mu s$, and the pulsewidth⁶, which shall be at least $0.265\cdot Tari$, hence $1.66\,\mu s$. The requirements are achieved by a fast-switching 6-bit digital attenuator from Analog Devices, the HMC472ALP4E integrated on an evaluation board. The attenuator is controlled by a sequencer and configured to switch between minimum and full attenuation to perform the on-off modulation. The hard on-off modulation violates compliance to the spectral mask, but since the measurements are carried out in the shielded anechoic chamber, this is of no consequence, and the additional filter is saved. The modulated RF carrier is then provided to the input of the amplifier. The signal power entering the PA is not monitored. Instead, the PA is operated up to a maximum of 1 dB below its maximum input power to cover the level inaccuracy of the source.

Power Amplifier

The PA shall provide a sufficient output power, support modulated signals, at the desired RF frequency range (865...868 MHz), and come as a off-the-shelf device. This is achieved by the Mini-Circuits ZHL-30W-252+ which was freely available in the lab. With a maximum output level of 46 dBm (measured) compared to the 23 dBm (measured) maximum output level of the signal source, it can clearly extend the power on the TX path which will be needed in configuration Probe-TX. Before the amplifier output is presented to the TX antenna, a portion must be coupled into a separate RF path for the magnitude and phase

⁵Reference time interval for a data-0 symbol in R⇒T signaling.

⁶Time interval between the falling and the rising edge of the on-off modulation in $R \Rightarrow T$ communication.

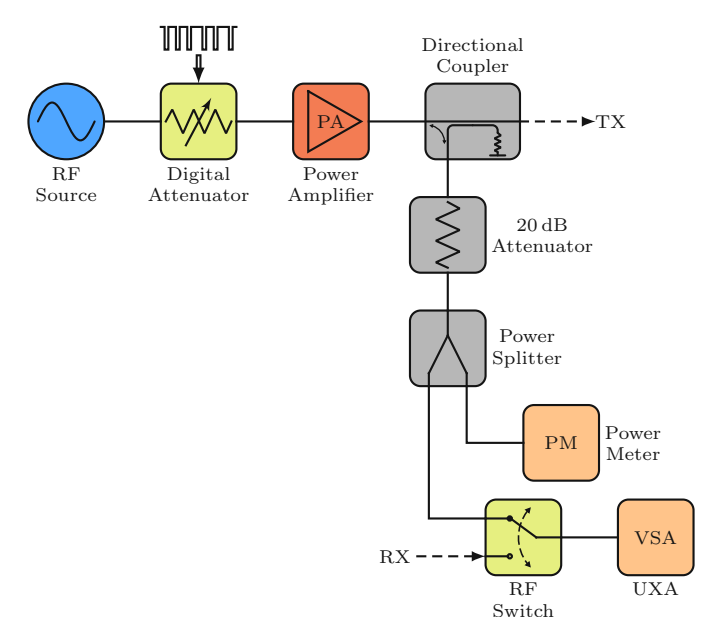


Figure 3.6: Block diagram of the measurement setup.

calibration. Before addressing the calibration, the RX path comprising the measurement instrument is introduced.

3.2.2Measurement Instrument

To determine the $\sqrt{\Delta RCS}$ accurately, it is necessary to capture the T \Rightarrow R communication over time. Vector signal analyzers (VSAs) are designed for such applications where a signal needs to be measured in magnitude and phase over time. Two VSAs were freely available in the lab, on the one hand, the Keysight N9040B UXA, and on the other, the Keysight M9391A PXI together with the Keysight 89600 VSA Software in version 21.2. The UXA is used in the measurement setup and the PXI is used as the additional receiver for configuration Probe-RX-C.

3.2.3 Calibration

As discussed in Section 2.2.3, the determination of the $\sqrt{\Delta RCS}$ requires, among knowing other parameters, measuring the complex-valued transmitted and received signals defined at the feeds of the TX and RX antenna. The antennas are located on the positioner system in the chamber and a vector measurement at these points would require installing additional equipment on the θ - and ϕ -stage which is not feasible. Therefore, the transmitted and received signals must be measured outside the chamber and afterwards de-embedded to the feed of the respective antenna. Since the exact phase centers of the TX and the RX antenna cannot be determined anyway, a magnitude calibration was performed and a relative phase calibration up to an unknown constant via the utilization of a phase reference was established. The magnitude calibration is done with a power meter because it achieves a higher amplitude accuracy than the UXA (PM: $\pm 0.04\,\mathrm{dB}$ vs. UXA: $\pm 0.16\,\mathrm{dB}$ at sub-GHz frequencies) and the phase calibration is done with the UXA. Through the coupling port of a directional coupler a portion of the transmitted signal is coupled out at the amplifier output and after proper attenuation provided to a power meter and to the UXA via a switch. The switch has two RF ports, one for the reference path and one for the receive path. A visualization of the calibration block can be found in Figure 3.6 where the previously described RF signal and query command generation is extended by the calibration block.

Power Meter

Only the unmodulated portion of the RF carrier, after the query command can be utilized for the power measurement. Therefore, a power meter that can handle timegated measurements is needed. In this measurement setup the Agilent E4417A power meter and the Agilent E9327A power sensor are utilized. The raw time-gated power readings conducted with a sample rate of 20 Msps and the gate length is chosen to be 600 µs. The power meter gets triggered from the sequencer as it will be explained in Section 3.2.4.

Phase Reference

Two things must be ensured when establishing a phase reference. (i) The RF signal source and the UXA must be synchronized to the same reference clock. (ii) The phase of the RF carrier must be measured together with the backscatter signal in each measurement and within a single recording of the UXA. Only in this case can a phase reference be achieved, because otherwise, it cannot be guaranteed that the phase reference between the signal source and the UXA does not change between separate measurements. Although the source and the UXA are frequency synchronized, they are not phase synchronized and their absolute local oscillator (LO) phase is arbitrary after startup. That is, even after two consecutive measurements the phase reference is lost which requires the measurement of the backscatter signal and the phase of the RF carrier within a single recording. In post-processing the phase of the backscatter signal is then corrected by the phase of the RF carrier.

RF Switch

Apart from sufficient isolation between the RF ports, no special requirements were placed on the RF switch. Therefore, a freely available switch was taken. It is a HMC545 from Hittite Microwave Corporation, comes integrated on an evaluation board and is controlled by the sequencer.

3.2.4 Sequencer

To form the query on the digital attenuator and to trigger the VSAs, the power meter and the switch, an instrument with digital outputs allowing the control of external devices with user defined marker signals is needed. The Rohde & Schwarz SMBV100A is capable of achieving this and is therefore used. Since the instruments are separate devices without a common clock, the reference of the sequencer at 10 MHz is shared with the RF signal source, and both VSAs.

The $R \Rightarrow T$ and $T \Rightarrow R$ sequences and the respective time steps are visualized in Figure 3.7, not to scale. As already indicated in Figure 2.1 no actual communication between the measurement system and the tag will be accomplished and therefore the measurement concludes right after the RN16. Moreover, no select command will be transmitted, as only a single tag is measured at a time. Therefore the RF carrier is provided to the tag for 2000 µs which comprises the maximum rising and settling time, 500 µs and 1500 µs respectively, as specified in the EPC Gen 2 [8]. No commands shall be issued before the

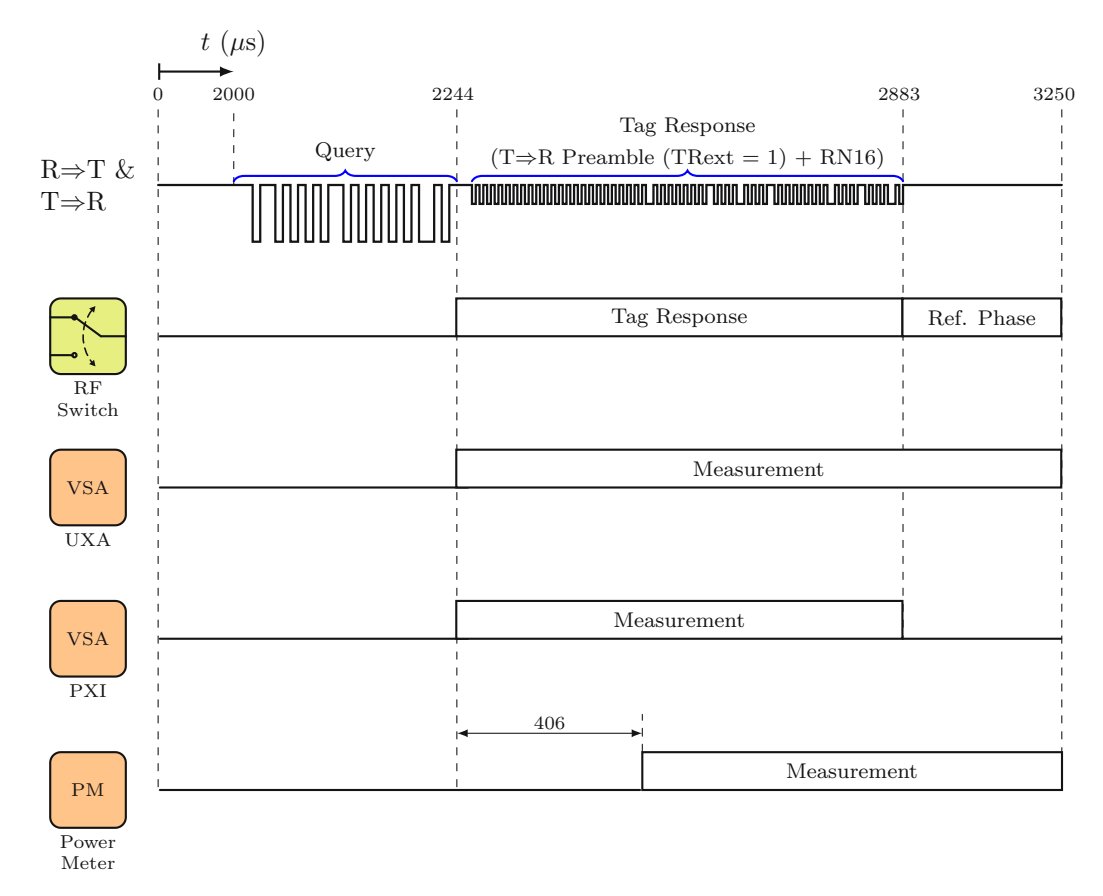


Figure 3.7: Implemented measurement timings with time steps indicating device activation, not to scale.

end of the maximum settling time. Then the query is transmitted which lasts for 244 µs in the present implementation. Since the durations for the data-0 and the data-1 symbol lengths are different and the query command includes a cyclic redundancy check (CRC), the determined duration is the minimum duration assuming only data-0 symbols in the CRC. Afterwards, the switch transitions to the receive path and the measurements on the instruments start. To ensure that the output power of the PA has stabilized after the on-off modulation during the query, the power meter measurement is delayed by 406 µs. After 639 µs, the switch transitions back to the reference path and the measurement on the UXA is continued while it ends on the PXI. Note that the duration of 639 us include the minimum time from the last bit of the query and the first bit of the tag response $(T_1 = 12 \,\mu\text{s})$ and further the maximum duration of the tag response (627 μs). The duration of the measurement of the RF carrier is not critical, and eventually, after 3250 µs the measurement is concluded.

3.3 Measurement Setup Overview

The implemented measurement setup together with the arrangement in the anechoic chamber is visualized, for configuration Probe-RX-C, in Figure 3.8. The measurement setup embeds the previously introduced blocks: the RF signal generation and modulation, the measurement instrument, the calibration, and the sequencer. In addition, the signal types RF, signaling, and 10 MHz are visualized using solid, dashed, and dotted line styles, respectively. It is designed to wake up the tag, by providing a query which then responses



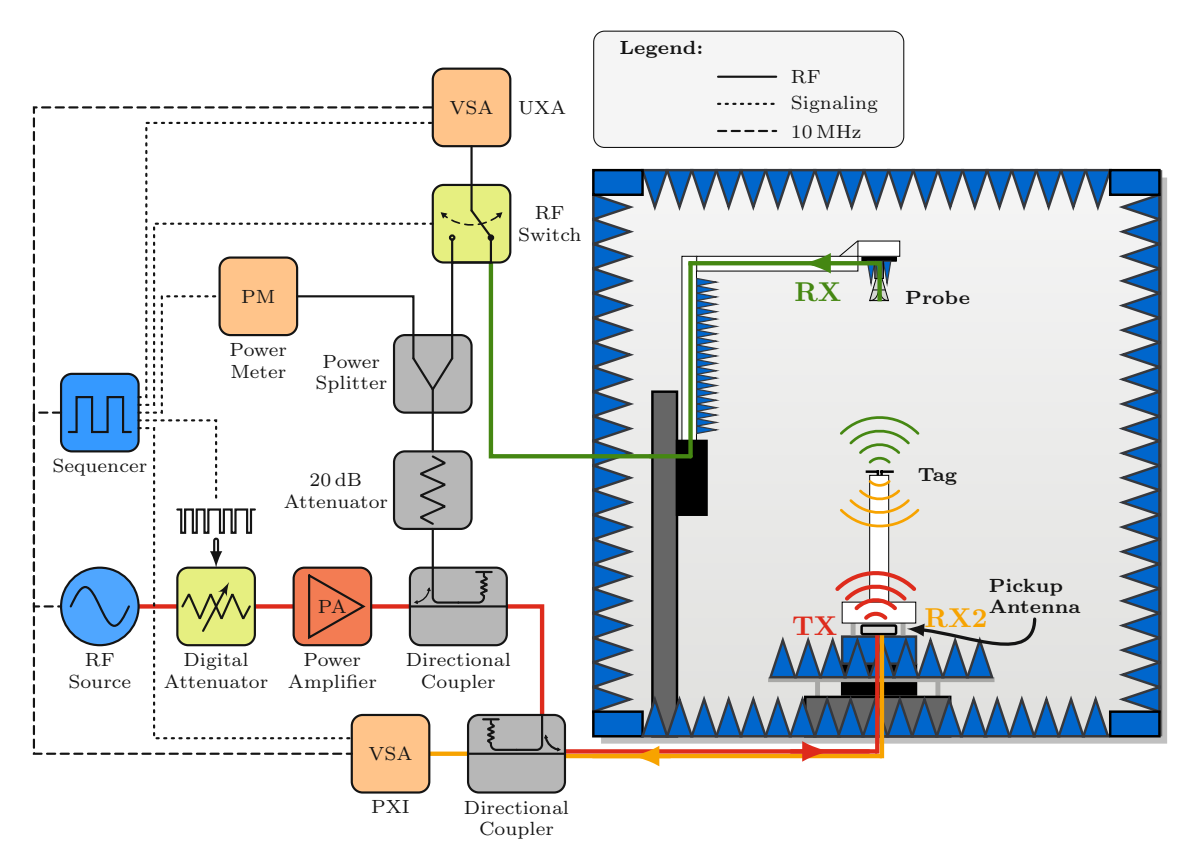


Figure 3.8: Block diagram of the implemented measurement setup together with the arrangement in the anechoic chamber for configuration Probe-RX-C.

with a T⇒R preamble and a RN16, without the need for commercial RFID hardware.

Since in configuration Probe-RX-C a second VSA is utilized, the phase reference of the second VSA requires consideration as well. Previously it was mentioned that it cannot be guaranteed that the phase reference of the source and the VSA is maintained between measurements and therefore the phase of the reference signal is measured together with the backscatter signal within every single measurement to establish the phase reference in post-processing. For the same reasons also for measurements with the PXI a phase reference to the source must be established. Since the PXI is already located in the transmit path and see's a strong leaking RF carrier while measuring the backscatter signal the phase reference can be established by compensating the backscatter signal by the phase of the leaking RF carrier in post-processing.

Throughout this work, measurements of configuration Probe-RX and Probe-RX-C are often compared. Since the measurement setup of configuration Probe-RX-C is an extension to the setup of configuration Probe-RX, it is not necessary to carry out separate measurements. Instead, the measurements are done only with configuration Probe-RX-C because the data that would be obtained by configuration Probe-RX is recorded in any case.

A picture of the hardware setup is presented in Figure 3.9. It depicts the power meter, sequencer, RF signal source, RF switch, digital attenuator, PA, PXI, positioner controller, connections to AUT and probe respectively, UXA, and the step attenuator. The step attenuator is not part of the measurement setup depicted in Figure 3.8 because it is only required for the performance evaluation in Chapter 4.

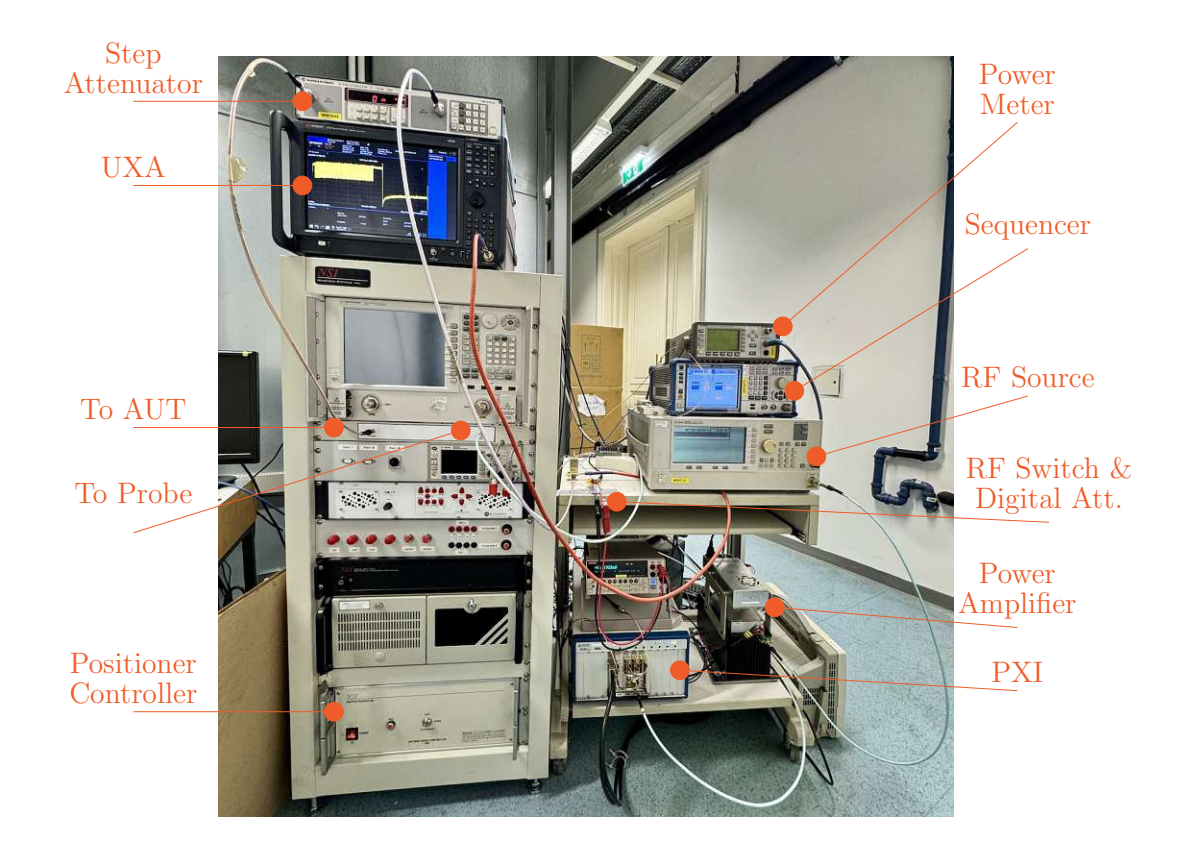


Figure 3.9: Photograph of the hardware setup. Note that the step attenuator is utilized in Chapter 4 and is not part of the standard measurement setup.

3.4 Measurement Procedure

First, the implementation of the power leveling is discussed, then the parameters of the implemented query command are presented, and then the data acquisition and processing of the measurement data is described.

3.4.1Power Leveling

Given that the tag exhibits a nonlinear response due to nonlinear and power-dependent internal circuit elements, it is crucial to operate the tag at a fixed point, defined at the power required to provide stable operation. To achieve this, a power-leveling process in which the source power is adjusted to meet this point, is necessary. A key observation allowing for an actual examination is that, if a tag receives enough power to operate correctly, a magnitude peak at the subcarrier beyond the noise floor is observable. That is, the decision whether the tag operates correctly or not, can be verified based on the behavior at the subcarrier, but care must be taken since the noise floor is not a constant, it is dependent on the resolution bandwidth (RBW) of the VSA. The smaller the RBW, the lower the noise floor but the longer the required sweep time. Since the tag response is of short length (max. 627 µs), it limits the maximum sweep time and raises the noise floor. However, once the power leveling reveals the magnitude peak at the subcarrier the respective source power level is increased by 2 dB as a power margin to ensure stable tag operation.



Figure 3.10: $T \Rightarrow R$ preamble with Miller subcarrier modulation and TRext = 1 [8].

3.4.2**Parameters**

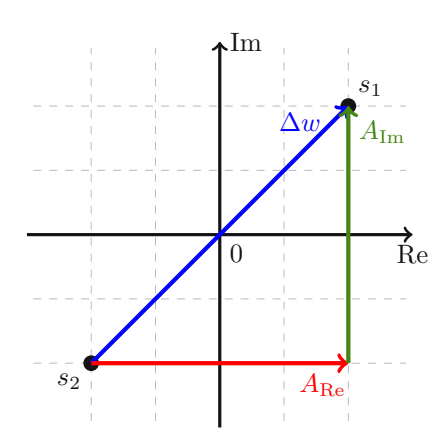
Since the tag's backscatter behavior, required for the determination of the $\sqrt{\Delta RCS}$, can only be gathered during T \Rightarrow R communication, careful choices must be made when configuring the parameters of the tag response. Doubling the frequency distance often results in more than 3 dB phase noise change, therefore, the approach is to select Miller subcarrier modulation together with the largest BLF of 640 kHz, the reduce the impact of the source phase noise. Nevertheless, a large BLF causes high data rate, i. e., the tag response will be of short length. This contradicts the idea, from the previous section, that a long duration of the tag response decreases the RBW of the VSA and consequently lowers the noise floor. To make up for that, the idea is to extend the tag response. To do so, the largest number of subcarrier cycles per symbol (M = 8) is selected and further the $T \Rightarrow R$ preamble is prolonged by 16 zero symbols instead of 4 by selecting TRext = 1, see Figure 3.10 for an illustration of the extended Miller preamble. Moreover, the illustration reveals that in Miller modulation encodes the data into phase changes which will be utilized in the next section. The choice of the RF frequency underlies regulatory constraints and in Europe the allocated range, by the ETSI [7], is 865...868 MHz. Due to this narrow bandwidth, it is sufficient to characterize the $\sqrt{\Delta RCS}$ on a single frequency which is set to $f_{RF} = 867.5 \, \text{MHz}$ without further consideration.

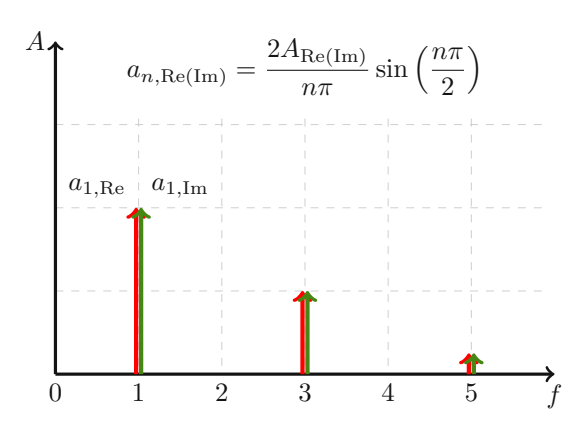
Data Acquisition and Post-Processing 3.4.3

The instrumentation and the positioner system are controlled directly from Matlab [42] using virtual instrument software architecture (VISA) to establish the connections and standard commands for programmable instruments (SCPI) to communicate. Physically, the devices are connected either via Ethernet or via General Purpose Interface Bus (GPIB) to the network. Such approach allows for an automated acquisition and processing of measurement data directly in Matlab, avoiding the manual data export.

Having the time domain signal, measured at the input of the VSA⁷, at hand, the delta tag response Δw (in V), i. e., the complex-valued difference between the modulation states of the tag, needs to be extracted first, to be then embedded in the $\sqrt{\Delta}$ RCS (cf. (2.15)). Before this can be done, the received signal must be processed as it contains not only the tag response but also the leaking RF carrier, the reference phase if the measurement was obtained with the UXA, and is affected by distortion and noise. Especially the signal distortion deserves attention and needs to be corrected because it limits the accuracy of the determination of Δw . It is revealed through a transient behavior of the RF carrier, on which the tag response is superimposed and results from a transient behavior of the PA's complex gain. During the transmission of the query command the RF carrier is on-off modulated causing a modulation of the junction temperature, consequently the complex

⁷The raw IQ-samples fetched from the VSA represent peak values of the in-phase and quadrature components of the RF signal and need to be related to a $50\,\Omega$ system before processing.





- (a) Tag's modulation in the complex plane.
- (b) Discrete line spectrum of the modulation, for the real and imaginary part independently.

Figure 3.11: Principle of determining Δw : The tag's continuous modulation between s_1 and s_2 generates a discrete line spectrum in which the first harmonic at the BLF is used to determine the magnitude from the Fourier coefficient, for the real and the imaginary part independently.

gain and, eventually, the output power of the PA exploiting an exponential growth/decay behavior. By fitting the parameters of an exponential function with an offset component to compensate simultaneously the RF carrier leakage

$$x_{\text{fit}}(t) = x_0 + (x_1 - x_0)(1 - e^{-t/\tau}),$$
 (3.1)

where x_0 and x_1 are the start and the end value (in V), and τ is the time constant in (in s). The fitted function is subsequently subtracted from the received signal. Now, the determination of Δw , via a fast Fourier transform (FFT)- and a correlation-based method, is presented. The FFT Method is used in configurations Probe-TX and Probe-RX and the Correlation Method is used in configuration Probe-RX-C.

FFT Method

The delta tag response Δw is the complex-valued difference of the tag's modulation states s_1 and s_2 , and is illustrated in the complex plane (time domain) in Figure 3.11a. By identifying both states the vector difference can be easily obtained. However, in measurements, the points become point clouds, see Figure 3.13b, due to noise and are distorted. The radii of the point clouds increase as the SNR decreases until they start to overlap, rendering an accurate state identification impossible. Therefore, the approach is to identify the states s_1 and s_2 in the Fourier domain where results are then transformed back into the time domain to obtain Δw . The Fourier analysis [43] is done for the real and the imaginary part of the complex-valued time domain signal individually. The real and the imaginary contribution in the complex plane $A_{\rm Re}$ and $A_{\rm Im}$ of Δw can be determined via the Fourier coefficients $a_{1,\text{Re}}$ and $a_{1,\text{Im}}$ of the first harmonic (and in general all other harmonics) located at the BLF, as illustrated in Figure 3.11, and

$$\Delta w := A_{\text{Re}} + jA_{\text{Im}} = \frac{\pi}{2} \left(a_{1,\text{Re}} + ja_{1,\text{Im}} \right) e^{-j\psi},$$
 (3.2)

where $\psi \in \{0, \pi\}$ denotes a phase correction term because, so far, it is ambiguous if Δw points from s_1 to s_2 or vice versa, hence the phase ambiguity of π must be resolved in an additional step. Before addressing this, note that to ensure that the Fourier coefficients at



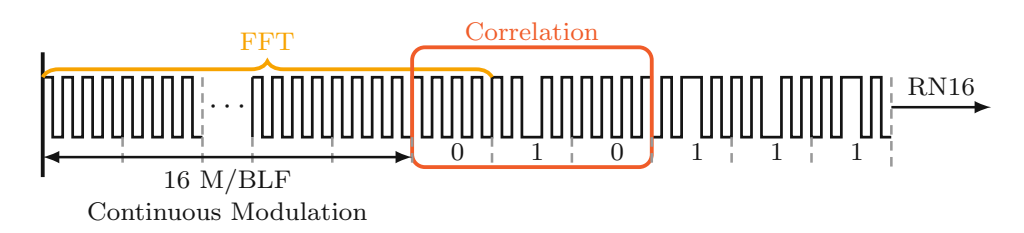


Figure 3.12: $T \Rightarrow R$ preamble with Miller subcarrier modulation and TRext = 1 [8], where the first phase inversion is utilized to resolve the phase ambiguity of the FFT Method.

the BLF are taken with high accuracy zero padding and windowing needs to be done prior to the FFT. A high amplitude accuracy is achieved with a Kaiser window [44] which was therefore selected.

Resolving the Phase Ambiguity: Use of the fact that Miller modulation encodes the data into phase changes can be made by correlating a synthetic Miller sequence with a phase inversion with the received signal to resolve the phase ambiguity. This is illustrated in Figure 3.12 where in yellow, the part of the T \Rightarrow R preamble utilized by the FFT Method and in orange, the part which is used for the correlation is marked. To improve the correlation result not only the Miller period with the phase inversion is correlated but also the Miller periods before and after. The phase of the correlation peak reveals the value of the phase correction term ψ . Note that the correlation performed to resolve the phase ambiguity must not be confused with the Correlation Method.

Correlation Method

The Correlation Method, utilized in configuration Probe-RX-C, eliminates the need for the generation of a synthetic Miller sequence to determine the phase of Δw unambiguously, instead the traces recorded at both VSAs are correlated after applying the necessary corrections mentioned above. In contrary to the FFT Method, the entire tag response including the RN16 can be utilized. A longer correlation length will result in a higher accuracy of the determination of Δw . To simplify the calculation and to avoid incorrect maxima, the processed signal captured at the pickup antenna $x_1(t)$ and the processed signal collected at probe $x_2(t)$ are time-aligned. Then the maximum of the correlation at $R_{x_1,x_2}(\tau=0)$ can be computed efficiently and does not need to be searched following

$$R_{x_1,x_2} = \int_{-\infty}^{\infty} x_1^*(t) x_2(t) \, \mathrm{d}t \,. \tag{3.3}$$

To obtain the delta tag response Δw , a magnitude correction m needs to be applied to the correlation result

$$\Delta w = m\Delta R_{x_1, x_2} \,, \tag{3.4}$$

and since configuration Probe-RX-C acts as supplementary approach to support configuration Probe-RX, the magnitude correction m is adjusted to align with the results of configuration Probe-RX.

Exemplary Measurements

To provide measurement data, consider Figure 3.13 for a visualization of the IQ data in the complex plane, in Figure 3.13a before and in Figure 3.13b after processing the



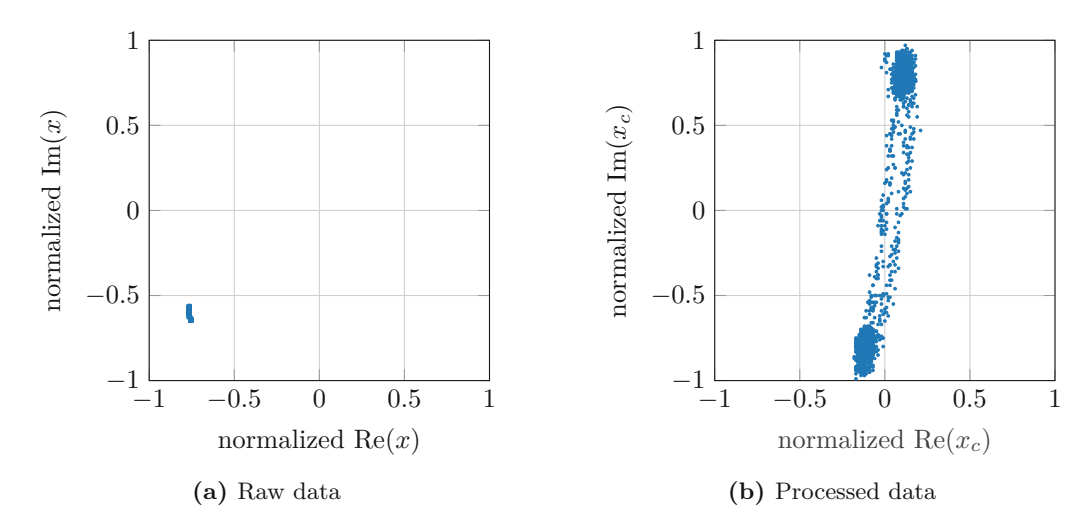


Figure 3.13: Exemplary IQ samples (normalized to the maximum) of the tag's continuous modulation, obtained by the Ucode7 label on Teflon, aligned in co-polarization to the probe located at $\theta = 0^{\circ}$: In (a) before and in (b) after processing the data.

raw data. The processing includes establishing the phase reference, the correction of the signal distortion, and removing the RF carrier leakage, as introduced previously. The measurements were conducted with the Ucode7 label on Teflon, introduced in Section 4.1, which was aligned in co-polarization to the probe. The probe was located at $\theta = 0^{\circ}$ and the measurement was conducted with configuration Probe-RX-C. The data is normalized to the respective maximum. After the processing, both point clouds revealing both modulation states appear centered around the origin whereas before, the point clouds are shifted from the origin, which is due to the backscattered portion of the RF carrier, i.e. self-interference, and also due to some reflections. Compared to the small distance between the modulation states, the offset from the origin is the predominant component. In addition to the just considered representation in the complex the same is repeated for the frequency domain in Figure 3.14, in Figure 3.14a before the corrections and in Figure 3.14b afterwards. This results are presented to emphasize the strong magnitude peak at the subcarrier which justifies the implemented method for the power leveling.

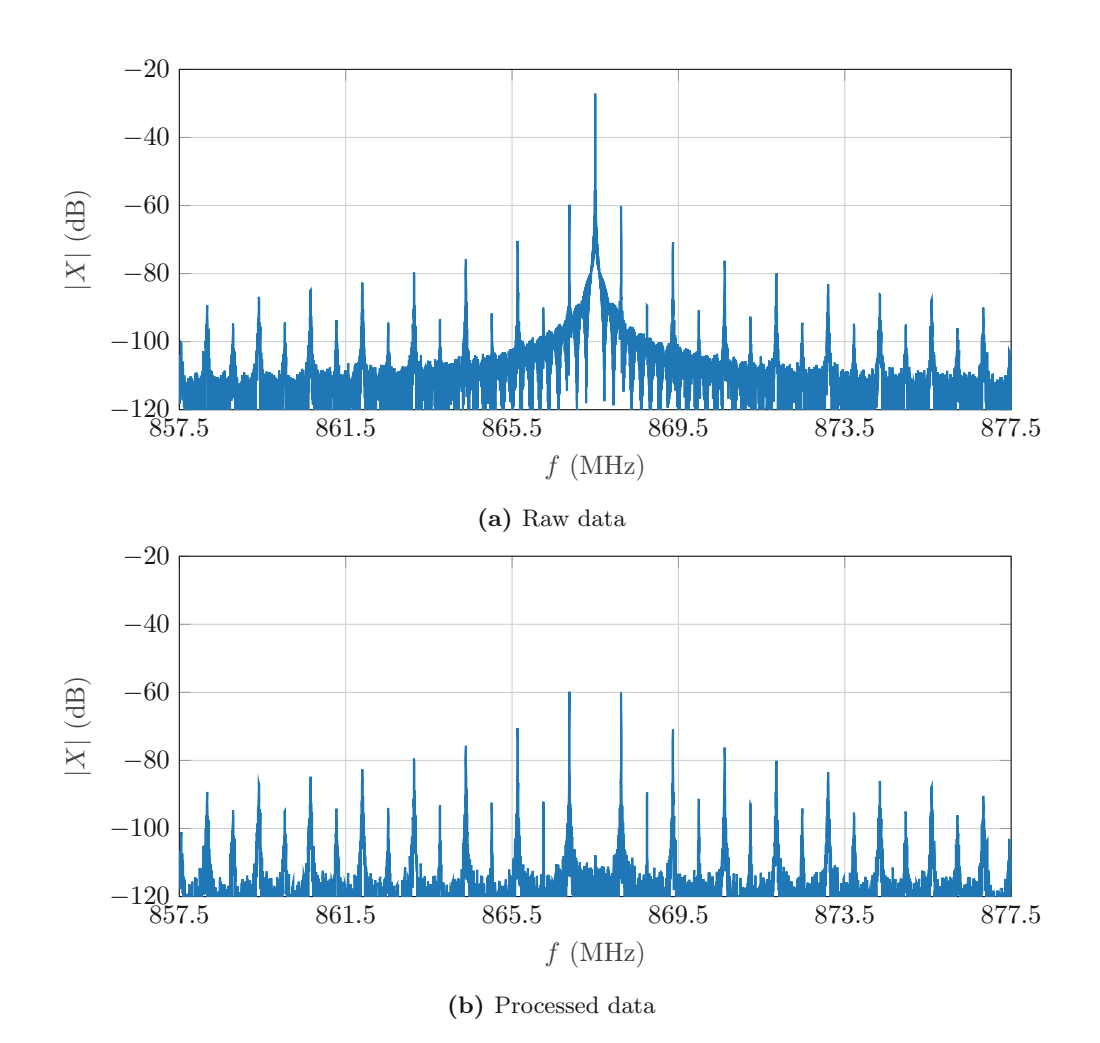


Figure 3.14: Frequency domain representation of the tag's continuous modulation, obtained by the Ucode7 label on Teflon aligned in co-polarization to the probe located at $\theta = 0^{\circ}$: In (a) before and in (b) after processing the data.

Determination of the $\sqrt{\Delta RCS}$ 3.5

This section delves into modeling the measurement situation inside the chamber on the positioner system to establish a framework leveraging the determination of the $\sqrt{\Delta RCS}$. To ensure a complex-valued $\sqrt{\Delta RCS}$, the modeling is based on a scattering description.

3.5.1Tag Model

The tag consisting of an antenna and a subsequent input stage can be described by a scattering flow graph [25] visualized in Figure 3.15. The radiation port indicates the incoming and outgoing waves on the tag antenna, whereas the local port indicates the power waves entering and leaving the input stage. The transformation between the waves is indicated by branches. That is, the power wave a entering the input stage is described by a particular field component χ_i of the incoming wave from a particular direction (θ_i, ϕ_i) at the antenna multiplied by its receiving partial square root gain

$$a = \sqrt{g_{\gamma_i}}(\theta_i, \phi_i)v. \tag{3.5}$$

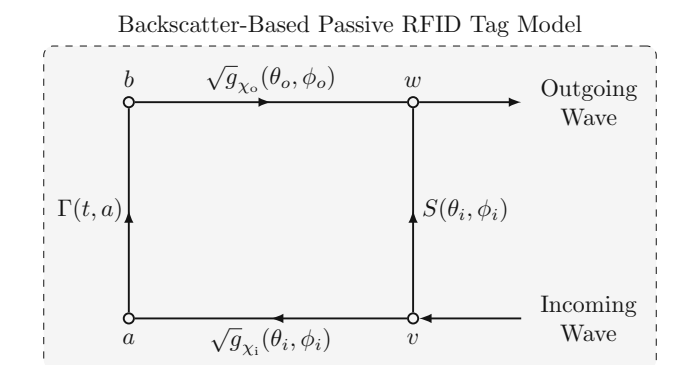


Figure 3.15: Model of a backscatter-based passive RFID tag based on scattering flow graphs.

The behavior of the input stage is denoted by a nonlinear power-dependent, time-variant reflection coefficient $\Gamma(t,a)$. It can modulate between two modulation states, $\Gamma_1(a)$ and $\Gamma_2(a)$. Hence

$$b(t,a) = \Gamma(t,a)a, \qquad \Gamma(t,a) \in \{\Gamma_1(a), \Gamma_2(a)\}. \tag{3.6}$$

The contributions to the outgoing wave w are then b multiplied by the transmitting square root gain and $S(\theta_i, \phi_i)$, denoting reflections, which do not enter the input stage at all. Matching a bistatic arrangement, the incoming direction particular field component $(\chi_i, \theta_i, \phi_i)$ and the outgoing direction particular field component $(\chi_o, \theta_o, \phi_o)$, do not have to be same, thus,

$$w(t, a, \theta, \phi) = S(\theta_i, \phi_i)v + \sqrt{g_{\chi_i}}(\theta_i, \phi_i)b(t, a)$$

$$= \left(S(\theta_i, \phi_i) + \sqrt{g_{\chi_o}}(\theta_o, \phi_o)\Gamma(t, a)\sqrt{g_{\chi_i}}(\theta_i, \phi_i)\right)v.$$
(3.7)

As it is of interest of how much the RFID tag modulates the backscatter, the focus is on the modulation state difference $\Delta\Gamma(a) = \Gamma_1(a) - \Gamma_2(a)$, simplifying (3.7) to

$$\Delta w(a, \theta, \phi) = \sqrt{g_{\chi_o}}(\theta_o, \phi_o) \Delta \Gamma(a) \sqrt{g_{\chi_i}}(\theta_i, \phi_i) v.$$
 (3.8)

Having defined an input/output relation of the tag, the next step is to derive the same for the antenna coupling on the positioner system, where (3.8) is embedded accordingly.

3.5.2Antenna Coupling Model

Figure 3.16 represents a model of the antenna coupling on the positioner system, where Figure 3.16a and Figure 3.16b are similar representations with the only difference in the scalar/vector notation and Figure 3.16c acts supplementary to establish a connection to the actual placement in the anechoic chamber. It consists of the necessary blocks comprising the properties of TX and RX antennas, the channel, and the tag, to derive a relation between the power wave v entering the feed of the transmitting antenna and the delta power wave Δw , which is in fact the delta tag response, at the feed of the receiving antenna. Perfectly matched TX/RX antennas and reciprocity are assumed, and far-field conditions must be ensured. The tag must be in the far field of the TX antenna and the RX antenna. Sources of error, such as noise, reflections, and positioning errors of TX/RX antennas, are neglected. The model is illustrated to match configurations Probe-RX and Probe-RX-C. Due to reciprocity it is also a valid description for configuration Probe-TX. The input/output relation will be derived from a block-wise explanation of the blocks, starting with Block 1a in Figure 3.16a. Note that K is a constant and part of a calibration procedure.

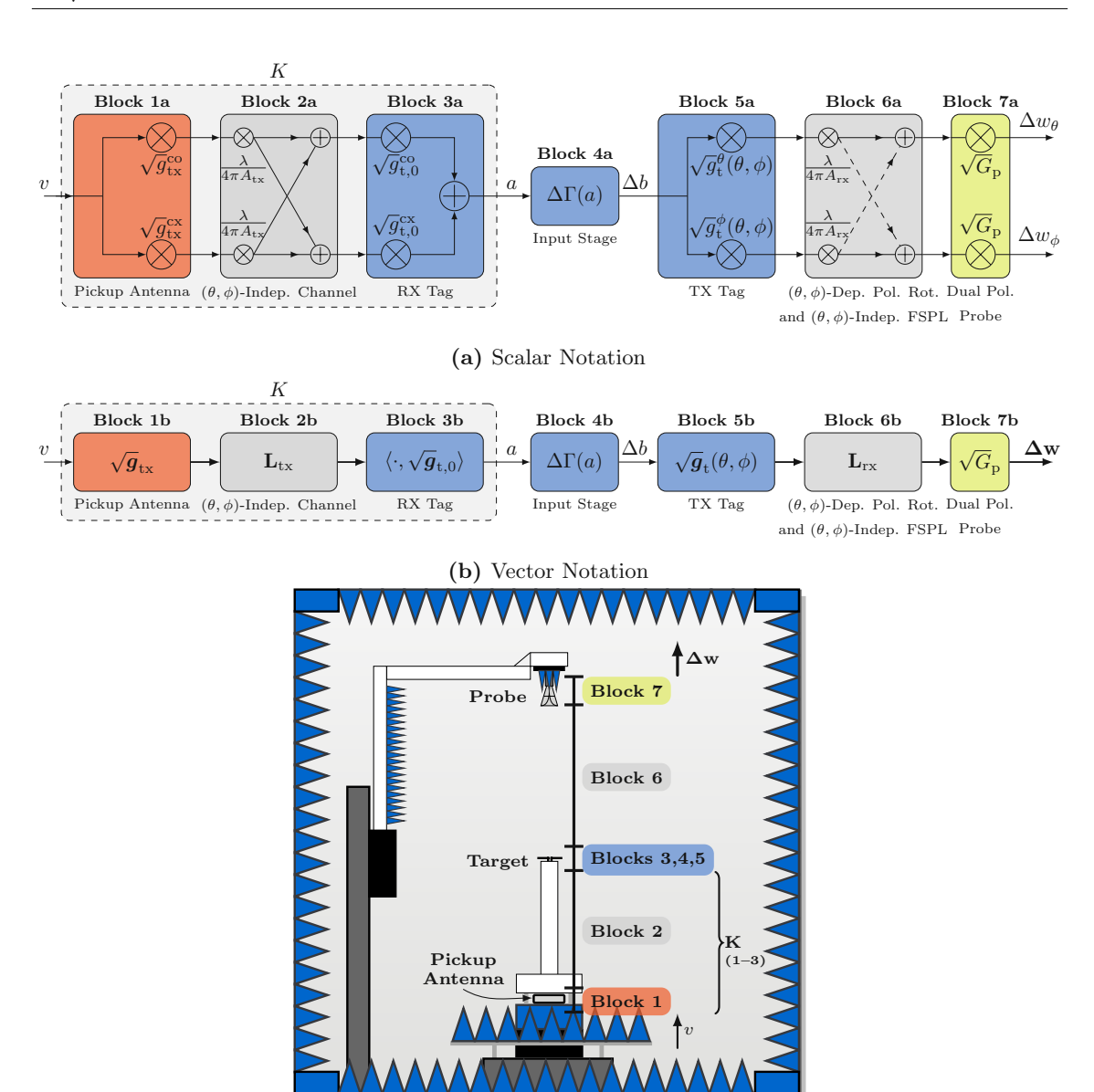


Figure 3.16: Representation of the measurement model: Description based on scalar notation in (a), based on vector notation in (b), and illustration of the model in the anechoic chamber in (c).

(c) Illustration in the chamber

Block 1a: A (complex-valued) power wave v at the local port of the transmit antenna is multiplied respectively by two orthogonal partial square root gain coefficients, $\sqrt{g_{\rm tx}^{\rm co}}$ and $\sqrt{g_{\rm tx}^{\rm cx}}$, and transmitted to the radiation port, where an outgoing wave emerges. Recall that the coupling between the TX antenna and the tag is (θ, ϕ) -independent due to their respective fixed positions on the ϕ -stage and the support structure, so the partial square root gain coefficients are constants.

Block 2a: A joint description of the TX path comprising the free-space path loss (FSPL), the phase rotation and the polarization basis transformation of the outgoing wave to the

incoming wave of the tag is provided by the matrix

$$\mathbf{L}_{\mathrm{tx}} = \frac{\lambda \mathrm{e}^{-jkA_{\mathrm{tx}}}}{4\pi A_{\mathrm{tx}}} \begin{pmatrix} l_{\mathrm{tx}}^{\mathrm{coco}} & l_{\mathrm{tx}}^{\mathrm{cocx}} \\ l_{\mathrm{tx}}^{\mathrm{coco}} & l_{\mathrm{tx}}^{\mathrm{cocx}} \end{pmatrix}$$

$$= l_{\mathrm{tx},0} \begin{pmatrix} l_{\mathrm{tx}}^{\mathrm{coco}} & l_{\mathrm{tx}}^{\mathrm{cocx}} \\ l_{\mathrm{tx}}^{\mathrm{coco}} & l_{\mathrm{tx}}^{\mathrm{cocx}} \\ l_{\mathrm{tx}}^{\mathrm{coco}} & l_{\mathrm{tx}}^{\mathrm{cocx}} \end{pmatrix},$$
(3.9)

where $l_{\rm tx,0}$ comprises the FSPL, the phase rotation, and $A_{\rm tx}$ denotes distance from the TX antenna to the tag. The matrix elements $l_{\rm tx}^{\chi_i\chi_o}$ express the polarization basis transformation χ_i to χ_o . As the TX antenna and the tag are placed with naked eye and not aligned, a polarization basis transformation is necessary to describe the coupling of the individual polarization components between the TX antenna and the tag antenna. Due to the (θ, ϕ) -independence of this path, the matrix elements are constants.

Blocks 3a and 4a: Based on the model of a tag presented in Section 3.5.1, the outgoing delta power wave Δb on the local port can be described as

$$\Delta b(a) = \Delta \Gamma(a) \left(\sqrt{\boldsymbol{g}}_{t,0} \right)^{H} \mathbf{L}_{tx} \sqrt{\boldsymbol{g}}_{tx} v$$

$$= \Delta \Gamma(a) K v.$$
(3.10)

As \sqrt{g}_{tx} , the vector $\sqrt{g}_{t,0}$ is evaluated in an unknown but (θ, ϕ) -independent direction. As a consequence, $\sqrt{g}_{\rm t,0}, \mathbf{L}_{\rm tx}$ and $\sqrt{g}_{\rm tx}$ can be described by an unknown constant Krepresenting the TX path behavior. The constant K is part of the calibration procedure explained in Section 3.5.3.

Block 5a: The delta power wave Δb is then provided to the radiation port, weighted with the partial square root gains, $\sqrt{g_t^{\theta}}(\theta,\phi)$ and $\sqrt{g_t^{\phi}}(\theta,\phi)$, where then an outgoing wave emerges.

The RX path exposes the same structure as the TX path introduced in Block 3a/b. It comprises the FSPL, the phase rotation, and the polarization basis transformation. Fortunately, the swing arm-over-azimuth scanner system is able to probe the polarization components θ and ϕ directly, without the need for further synthesis, simply by orienting the probe antenna in $\chi = 0^{\circ}$ and $\chi = 90^{\circ}$. In this way, the polarization transformation reduces to an identity matrix

$$\mathbf{L}_{\rm rx} = \frac{\lambda e^{-jkA_{\rm rx}}}{4\pi A_{\rm rx}} \mathbf{I} = l_{\rm rx,0} \mathbf{I}. \tag{3.11}$$

This block models the probe. The square root gain of the probe is the only one known in advance. Due to the assumption of perfect cross-polarization suppression, the total square root gain \sqrt{G}_p is used instead of the partial square root gain. For modeling purposes, a dual-polarized probe is assumed, allowing both polarization components to be measured in a single measurement. The transmission formula can then be written as

$$\Delta \mathbf{w}(a, \theta, \phi) = \sqrt{G_{\rm p}} \mathbf{L}_{\rm rx} \sqrt{\mathbf{g}_{\rm t}}(\theta, \phi) \Delta \Gamma(a) K v, \qquad (3.12)$$

and in its polarization components

$$\Delta w_{\theta}(a, \theta, \phi) = \sqrt{G_{\rm p}} l_{\rm rx, 0} \sqrt{g_{\rm t}^{\theta}}(\theta, \phi) \Delta \Gamma(a) K v, \qquad (3.13a)$$

$$\Delta w_{\phi}(a,\theta,\phi) = \sqrt{G_{\rm p}} l_{\rm rx,0} \sqrt{g_{\rm t}^{\phi}}(\theta,\phi) \Delta \Gamma(a) K v. \qquad (3.13b)$$

These equations express the complex receive vector $\Delta \mathbf{w}(a, \theta, \phi)$ by the probe as a function of the partial square root gain $\sqrt{g}_{\rm t}(\theta,\phi)$ and the modulation state difference $\Delta\Gamma(a)$. It is emphasized that a distinct determination of $\Delta\Gamma(a)$ and $\sqrt{g}_{t}(\theta,\phi)$ is not possible, because the impedance of the input stage is not known. In the next step, a calibration procedure is introduced that allows the determination of $\sqrt{\Delta RCS}$, without knowing the exact TX path behavior.

3.5.3Resolving the Unknown Path

Absolute calibration can be achieved by reversion of TX/RX and fulfilling the tag's minimum power condition (cf. Section 3.4.1). The first measurement is conducted using the configuration Probe-RX (cf. Figure 3.3). That is, the source power wave v_1 is increased until the level of the power wave a entering the input stage of the tag is large enough to power up the tag

$$a_{\min} = K v_1. \tag{3.14}$$

The specific spherical direction (θ_0, ϕ_0) is not important, but it must be maintained during the calibration procedure. The next measurements are conducted in the same manner but using configuration Probe-TX (cf. Figure 3.2) and each respective polarization

$$a_{\min}^{\theta} = \sqrt{g_{\mathrm{t}}^{\theta}}(\theta_0, \phi_0) l_{\mathrm{rx},0} \sqrt{G_{\mathrm{p}}} v_2, \qquad (3.15a)$$

$$a_{\min}^{\phi} = \sqrt{g_{\rm t}^{\phi}}(\theta_0, \phi_0) l_{\rm rx,0} \sqrt{G_{\rm p}} v_3 \,.$$
 (3.15b)

The tag's minimum input power, i.e., the minimum level of the power wave a, is independent of the measurement direction. Consequently

$$a_{\min} \stackrel{!}{=} a_{\min}^{\theta} \stackrel{!}{=} a_{\min}^{\phi} . \tag{3.16}$$

Inserting (3.14), (3.15a) and (3.15b) into (3.16) and rearranging to solve for K reads

$$K = \frac{v_2}{v_1} \sqrt{g_t^{\theta}} (\theta_0, \phi_0) l_{\text{rx},0} \sqrt{G_p}$$
(3.17a)

$$= \frac{v_3}{v_1} \sqrt{g_t^{\phi}}(\theta_0, \phi_0) l_{\text{rx},0} \sqrt{G_p}$$
(3.17b)

Despite having only one constant K, both (3.17a) and (3.17b) are required, as the goal is to state independent expressions for each polarization. Finally, (3.17a) and (3.17b) are inserted in (3.13a) and (3.13b) respectively

$$\Delta w_{\theta}(\theta, \phi) = \frac{v_2}{v_1} G_{\rm p} l_{\rm rx,0}^2 \sqrt{g_{\rm t}^{\theta}}(\theta, \phi) \Delta \Gamma(a_{\rm min}) \sqrt{g_{\rm t}^{\theta}}(\theta_0, \phi_0) v, \qquad (3.18a)$$

$$\Delta w_{\phi}(\theta,\phi) = \frac{v_3}{v_1} G_{\rm p} l_{\rm rx,0}^2 \sqrt{g_{\rm t}^{\phi}}(\theta,\phi) \Delta \Gamma(a_{\rm min}) \sqrt{g_{\rm t}^{\phi}}(\theta_0,\phi_0) v. \tag{3.18b}$$



Embedding the $\sqrt{\Delta RCS}$ 3.5.4

Recall Section 2.1.4 where the $\sqrt{\Delta RCS}$ was expressed by (2.5). This expression will be reformulated to embed the bistatic arrangement and to consider a certain polarization χ

$$\sqrt{g_{\rm t}^{\chi}}(\theta,\phi)\Delta\Gamma(a_{\rm min})\sqrt{g_{\rm t}^{\chi}}(\theta_0,\phi_0) = \frac{\sqrt{4\pi}}{\lambda}\sqrt{\Delta\sigma_{\chi}}(\theta,\phi). \tag{3.19}$$

Embedding (3.19) into (3.18a) and (3.18b) individually and express in terms of the $\sqrt{\Delta}RCS$

$$\sqrt{\Delta\sigma_{\theta}}(\theta,\phi) = \frac{\Delta w_{\theta}(\theta,\phi)}{v} \frac{v_1}{v_2} \frac{\lambda}{\sqrt{4\pi} l_{\text{rx},0}^2} \frac{1}{G_{\text{p}}}$$
(3.20a)

$$\sqrt{\Delta\sigma_{\phi}}(\theta,\phi) = \frac{\Delta w_{\phi}(\theta,\phi)}{v} \frac{v_1}{v_3} \frac{\lambda}{\sqrt{4\pi} l_{\rm rx,0}^2} \frac{1}{G_{\rm p}}$$
(3.20b)

Finally, the expression for $l_{\rm rx,0}$, the scalar factor involving the FSPL and the phase rotation as previously defined, is substituted into (3.20a) and (3.20b). The resulting expressions are then obtained by

$$\sqrt{\Delta\sigma_{\theta}}(\theta,\phi) = \frac{\Delta w_{\theta}(\theta,\phi)}{v} \frac{v_1}{v_2} \frac{4\pi A_{\rm rx}^2}{\lambda} \frac{\sqrt{4\pi}}{G_{\rm p}} e^{j2kA_{\rm rx}}, \qquad (3.21a)$$

$$\sqrt{\Delta\sigma_{\phi}}(\theta,\phi) = \frac{\Delta w_{\phi}(\theta,\phi)}{v} \frac{v_1}{v_3} \frac{4\pi A_{\rm rx}^2}{\lambda} \frac{\sqrt{4\pi}}{G_{\rm p}} e^{j2kA_{\rm rx}}, \qquad (3.21b)$$

where $k = 2\pi/\lambda$ denotes the wavenumber. Equations (3.21a) and (3.21b) represent the monostatic $\sqrt{\Delta RCS}$ for a (θ, ϕ) -polarization basis of an arbitrary passive RFID tag, derived from a measurement obtained in a bistatic arrangement. Further, (3.21) aligns conceptually with the definition of the radar cross-section found in the literature, for example, see [34]. Since RCS values are typically expressed on a logarithmic scale, i.e., in decibels referenced to one square meter (dBsm), the conversion, for an arbitrary polarization component χ reads

$$\Delta \sigma_{\chi}(\theta, \phi) = 20 \log_{10} \left(\frac{\left| \sqrt{\Delta \sigma_{\chi}(\theta, \phi)} \right|}{\sqrt{1 \,\mathrm{m}^2}} \right) \,. \tag{3.22}$$

Note that the logarithmic representation in (3.22) employs the $\sqrt{\Delta RCS}$ as a power quantity. In order to ensure comparability to results of others, henceforth, the logarithmic representation in (3.22) will be used to represent the magnitude of the $\sqrt{\Delta RCS}$ and the phase of the $\sqrt{\Delta RCS}$ will be represented as

$$\angle\sqrt{\Delta\sigma_{\chi}}(\theta,\phi) = \angle\Delta w_{\chi}(\theta,\phi) + 2kA_{\rm rx}. \tag{3.23}$$

Recall that only relative phase calibration up to an unknown constant is achieved by the measurement setup and thus the second summand can be neglected.

3.6 Link Budget

The link budget is based on the measurement model presented in the previous section and follows (3.12). Moreover, it is evaluated by measurements conducted with the label on



Table 3.1: Link budget of the implemented configurations based on measurements with the label on Teflon centered in the measurement sphere and aligned in co-polarization to the probe.

Element	Unit	Pro	Probe-TX		be-RX	Probe	e-RX-C
		Block	Value	Block	Value	Block	Value
Amplifier Output	dBm		15.1		19.6		39.6
TX Path Losses	dB		5.3		3.7		23.7
TX Antenna Gain	dBi	7	5.2	1		1	
TX Path Gain	dB	6	-33.6	2	$\rightarrow -32.3^{1}$	2	$\rightarrow -32.3^{1}$
Tag Antenna Gain [45]	dBi	5	2.2	3		3	
Tag Mod. Efficiency [6]	dB	4	-5.0	4	-5.0	4	-5.0
Tag Antenna Gain [45]	dBi	3		5	2.2	3	
RX Path Gain	dB	2	-32.3^{1}	6	-33.6	2	$\rightarrow -32.3^{1}$
RX Antenna Gain	dBi	1		7	5.2	1	
RX Path Losses	dB	,	3.7		5.3	·	4.1
RX at VSA ²	dBm		-57.4		-52.9		-57.8
→ Leakage	dBm		-28.2		-23.7		17.4
→ Phase Noise	$\mathrm{dBm/Hz}$		-171.2		-166.7		-125.6
Thermal Noise	$\mathrm{dBm/Hz}$		-174.0		-174.0		-174.0

 $^{^1}$ Measured in different scenarios with tagged objects: $-36.8...-28.4\,\mathrm{dB}$

Teflon, centered in the measurement sphere with the naked eye, aligned in co-polarization to the probe located at $\theta = 0^{\circ}$, and for a RF frequency of 867.5 MHz. It is emphasized that utilizing a different tag, tagged object, or a different placement on the tag support structure will result in different results for certain elements. To capture this, ranges are specified for these elements. Nevertheless it is not possible to evaluate all contributions in (3.12) by measurements only, thus, the (ideal and omnidirectional) tag gain is provided by [45] and the tag modulation efficiency (Block 4) is suggested by Dobkin [6]. The link budget, is tabulated in decibel notation, in Table 3.1 for all elements and all all three configurations together with the block numbers. It is explained starting with the $R \Rightarrow T$ link.

$R \Rightarrow T$ Budget 3.6.1

First, the calibration procedure presented in Section 3.5.3 is followed. That is, the power levels v_1 and v_2 , at the feed of the respective TX antennas, required to activate the tag, were determined for configurations Probe-TX and Probe-RX by simply increasing the source power until a peak at the subcarrier was visible. Both levels are not explicitly listed in Table 3.1 but rather the respective amplifier output power and losses on the transmission line which in sum up to the power levels v_1 and v_2 . Following configuration Probe-TX in its actual order from Block 7 to Block 1, the measured gain of the probe (Block 7) is 5.3 dB and the path gain between probe and tag (Block 6) can be calculated by inserting the measurement distance $A_{\rm rx} = 1.31$ m and the wavelength λ at 867.5 MHz in (3.11), where the matrix reduces to the scalar $l_{\rm rx,0}$ if only a single polarization component is considered,

²Probe-TX and Probe-RX: UXA (cf. Section 3.2) | Probe-RX-C: PXI (cf. Section 3.2)

and results in $-33.6\,\mathrm{dB}$. To determine the minimum level of the power wave a entering the input stage (Block 4) via (3.14) the tag gain in direction to the probe (Block 5) is needed. As mentioned previously, the gain is unknown and thus the value provided by the datasheet [45], which assumes an ideal and omnidirectional dipole, must be used. Finally, the level of a_{\min}^{θ} was determined to $-16.4\,\mathrm{dBm}$. In fact, this is $4.6\,\mathrm{dB}$ more then the datasheet suggests, but it is to be expected that the label on Teflon does not achieve the specified performance, since the Teflon was to provide the label with roughly the dielectric backing for which it was designed but it does not meet it precisely. With knowing the level of a_{\min} , the $R \Rightarrow T$ link is concluded.

3.6.2 $T\Rightarrow R$ Budget

The input stage (Block 4) comprises the modulation behavior ($\Delta\Gamma$) and also this value is unknown. Dobkin [6] suggests a modulation efficiency of $-5 \,\mathrm{dB}$ which means that the modulated backscatter power is around 1/3 of the absorbed power. Note that this is a design-specific parameter and can only be estimated as it varies from one design to another. Moving further, the Blocks 3 to 1 are not determined individually, instead they are jointly described by the constant K which is determined by evaluating (3.14). To do so, (3.14) is reformulated for K and the power level v_1 , determined initially with configuration Probe-RX as well as a_{\min} are inserted. It results in $-32.3\,\mathrm{dB}$ for this specific measurement situation but can vary from $-36.8...-28.4\,\mathrm{dBm}$ measured with several tagged objects. This range was determined empirically by examination of different tags, tagged objects, and tag orientations. Eventually, all relevant Blocks are determined and by accounting for the losses on the transmission line from the pickup antenna to the VSA, the received signal strength at the VSA can be determined which results in $-57.4\,\mathrm{dB}$. After the link budget is determined for configuration Probe-TX, the link budget for configuration Probe-RX follows directly as it is just in the opposite direction from Block 1 to 7. In contrast, the situation is different in configuration Probe-RX-C due to the monostatic scenario it passes the Blocks from 1 to 3 twice.

3.6.3 Leakage, Phase and Thermal Noise

The leakage can be determined by simply measuring the RF carrier without the tag in the test range. Note, especially for configuration Probe-RX-C the strong RF carrier leakage compared to the comparatively weak backscatter signal strength. The phase noise contribution can be determined by using the measured $-143\,\mathrm{dBc/Hz}$ and adding the leakage. The thermal noise at the VSA is $-174\,\mathrm{dBm/Hz}$.

Chapter 4

Results

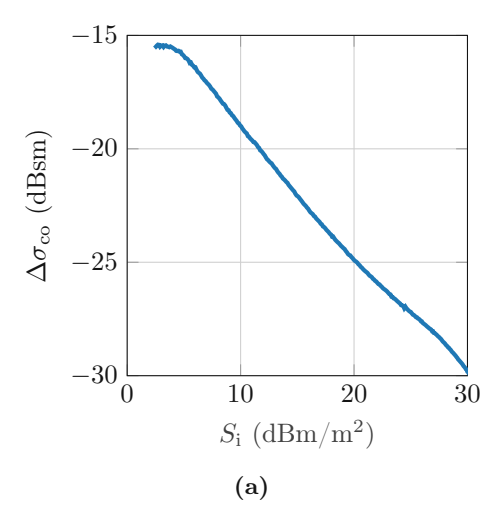
In this chapter, emphasis is given to the results obtained using the implemented $\sqrt{\Delta RCS}$ characterization method. The first aspect to assess is the nonlinear $\sqrt{\Delta RCS}$ behavior when the tag, which will be introduced in Section 4.1, is driven beyond its operating point, in Section 4.2. In Section 4.3, a performance comparison of the three developed configurations follows, where these are compared in four criteria including the measurement duration, the hardware complexity, the achievable power density at the tag, and the achievable dynamic range. During the performance evaluation, long-term $\sqrt{\Delta RCS}$ oscillations became apparent, worth noting and discussing in Section 4.4. Eventually, a truncated-sphere $\sqrt{\Delta RCS}$ pattern is presented in Section 4.5.

Tag under Test 4.1

The RFID label, which consists of the Ucode7 [45] chip embedded in a meander-shaped antenna, was used during this and the next chapter. The decision for this label is simply because it was available in the lab, and although this chip is several years old, its sensitivity can keep up with newer generations. Considering that RFID labels are designed to be mounted on objects, this label is intended for the application in the retail/fashion market, i.e., to be attached to apparel or footwear. In free space it does not achieve its peak performance. By supplying a backing made from a Teflon bulk, which was empirically found as a tradeoff with respect to the dielectric properties, the performance of the label could be significantly enhanced. The label on Teflon was then utilized for the evaluations throughout this chapter.

4.2 $\sqrt{\Delta RCS}$ Power Dependency

To study the behavior of the $\sqrt{\Delta RCS}$, when the tag is driven beyond its operating point, a power sweep was conducted. To this end, the power density S_i at the tag's location was increased in 0.1 dB-steps from the level required to wake up the tag, to the maximum level that the measurement configuration can provide. Configuration Probe-TX was utilized as it can provide the largest incident power density. Such an evaluation gives an indication how sensitive the tag behaves and, consequently, how precise the power leveling must be done. This deserves special attention because in configuration Probe-TX the power leveling is done for each (χ, θ, ϕ) -position and the required precision in this process contributes significantly to the overall measurement duration. To do so, the Ucode7 label on Teflon was placed on the support structure and aligned, with the naked eye, in co-polarization to the probe which was located at $\theta = 0^{\circ}$ during the measurement. The results are presented in Figure 4.1, where Figure 4.1a depicts the magnitude of the $\sqrt{\Delta RCS}$ and Figure 4.1b the associated phase. First of all, it can be seen that both, the magnitude and the phase. depend on the incident power density S_i . While the magnitude remains approximately



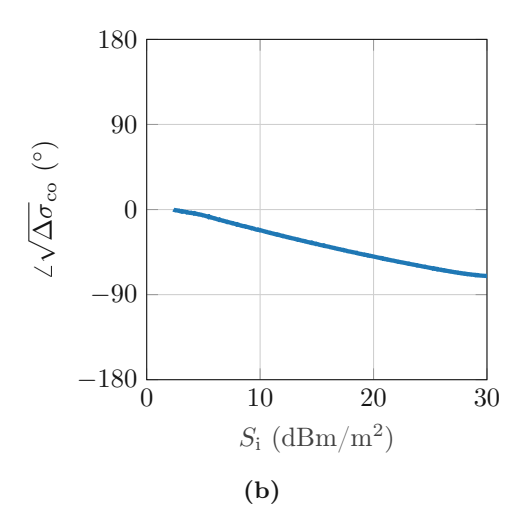


Figure 4.1: Analysis of the $\sqrt{\Delta RCS}$ power dependency: Conducted with the Ucode7 label on Teflor aligned in co-polarization to the probe located at $\theta = 0^{\circ}$: Magnitude in (a) and phase in (b).

constant for small offsets $(S_i - S_{i,min}) < 2 dB$, for larger offsets it decreases. From a radar's perspective this is an unfavorable result since the RCS is a property of the radar target and dependent on the targets shape or size but not on the incident power density. The phase exhibits almost the same behavior as the magnitude, with the only difference that it decreases even for small offsets $(S_i - S_{i,min}) < 2 \,\mathrm{dB}$. In total, the phase rotates about 70°. Compared to results presented by others [17], it was concluded that the tag phase variation is less than 10° due to varying power in a range of approximately 20 dB of the incident signal. Having in mind that the tag exhibits nonlinear behavior, a variation in magnitude and phase is reasonable.

The analysis emphasizes the sensitivity of the tag with regard to the incident power density. It is an important finding for the $\sqrt{\Delta RCS}$ characterization method, because it suggests that the power leveling should ideally be performed in each spherical measurement, regardless of the actual configuration, because different (χ, θ, ϕ) -positions lead to changing reflections due to the insufficient performance of the absorbers at this frequency. Moreover, the granularity of the power leveling should be set as fine as possible. Furthermore, this finding is also important in the context of phase-based localization, as it means that even if the tag maintains its position, if the incident power density changes, the phase of the tag changes as well, which may causes localization inaccuracies.

Measurement Configurations' Achieved Performance 4.3

The three developed configurations, introduced in Section 3.1, are compared in four criteria comprising the measurement and movement (of the spherical positioner system) duration per sample, the hardware complexity, the achievable power density at the tag's location, and achievable dynamic range, where the results are listed in Table 4.1 and elaborated in the following. The grading is based on empiric observations and measurements.

4.3.1Measurement Duration

The first evaluation analyzes the measurement/movement duration per sample achieved by the respective configuration. Since the absolute time, required for a spherical measurement,



Table 4.1: Performance comparison of the implemented configurations.

Criterion	Probe-TX	Probe-RX	Probe-RX-C
Duration per Sample	_	+	0
\rightarrow Measurement ¹	2.243.3 s (avg: 14.1 s)	$1.0\mathrm{s}\mathrm{(fix)}$	$1.8 \mathrm{s} \mathrm{(fix)}$
\longrightarrow Movement $(avg)^1$	$2.0\mathrm{s}$	$2.0\mathrm{s}$	$2.0\mathrm{s}$
Hardware Complexity	0	0	_
→ Power Amplifier	У	(y)	У
→ Additional VSA	n	n	У
Power Density at Tag	+	+	0
$\longrightarrow S_{\max}^2$	$32.6\mathrm{dBm/m^2}$	$20.3\mathrm{dBm/m^2}$	$12.6\mathrm{dBm/m^2}$
Dynamic Range	$28.1\mathrm{dB}$	$40.2\mathrm{dB}$	$66.2\mathrm{dB}$
$\longrightarrow \overline{SNR}^3$	$48.8\mathrm{dB}$	$47.9\mathrm{dB}$	$28.7\mathrm{dB}$

Legend: '+' = Excellent, 'o' = Average, '-' = Poor, 'n' = No, 'y' = Yes, '(y)' = not necessarily ¹In a spherical measurement with bi-directional and equiangular sampling ($\Delta_{\theta\phi} = 10^{\circ}$)

is dependent on the angular step size, the idea was to determine the measurement duration per sample and separately a movement duration per sample to distinguish between measurement/data acquisition and movement of the positioner system.

The movement duration per sample takes the movements of the probe in χ , the θ -stage, and the ϕ -stage along with the communication of the positioner controller and Matlab into account and is understood as an average value. It was evaluated in an exemplary spherical measurement, bi-directional and equiangulary sampled in 10°-steps, for two polarizations. In this setting, the average movement duration per sample evaluates to 2.0 s. If uni-directional instead of bi-directional sampling is pursued the movement duration per sample increases further to 2.4s. Now, emphasis is given to the measurement duration per sample, starting with configuration Probe-TX.

Configuration Probe-TX: A power leveling is pursued in each (χ, θ, ϕ) -position, i. e., it is only possible to state a range instead of a fixed duration. With a minimum duration per sample of 2.2s and a maximum of 43.3s, it is obvious that this configuration performs very slow. Nevertheless, due to the omnidirectional behavior of the tag, it is possible to accelerate the power leveling, when approaching new (χ, θ, ϕ) -positions, by providing initial values based on power levels found in previous (χ, θ, ϕ) -positions. For example, if scanning over ϕ , then the levels found on the previous θ -step can be utilized as initial values. Eventually, an average measurement duration per sample of 14.1s was determined during the spherical measurement. Note that this can change significantly, if a tagged object is measured and no prior assumptions for the power leveling can be made. Conclusively, for a productive system, this configuration is too slow, thus it receives a '-' in this criterion.

Configuration Probe-RX: Achieves with 1.0s the fastest measurement duration per sample and on contrary to configuration Probe-TX, it is a fixed duration since the power leveling is done only once at the beginning of the spherical measurement. It was found

²Pickup antenna gain taken from the datasheet [46]

³In the mean delta radar cross-section (ΔRCS) that can be measured by all configurations

that especially the power meter is less responsive, which was connected via a GPIB. Since, the power meter is used in all configurations, this does not contribute to the evaluation, therefore this configuration gets a '+' in this criterion.

Configuration Probe-RX-C: Differs to configuration Probe-RX by utilizing an additional VSA. The PXI is controlled by the VSA software on a host computer which does not allow to acquire the measurement data directly from the software, instead, a .mat file must be stored on the computer from where the data can then be imported to the Matlab script. This overhead comes costly with 0.8s additional duration per sample compared to configuration Probe-RX, issuing a 'o' in this criterion.

Hardware Complexity 4.3.2

All configurations employ an RF signal source, a sequencer, a power meter together with a power sensor, a VSA, several elements (e.g., couplers, splitter, isolator) and a pickup antenna. The digital attenuator and switch will likely need to be purchased separately but are available as off-the-shelf elements. This together forms the basic equipment regardless of the utilized configuration and does not contribute to the hardware complexity evaluation.

Configuration Probe-TX: Requires an additional PA, but not an additional VSA, thus receiving a 'o' in this criterion.

Configuration Probe-RX: Makes use of an additional PA in the current implementation, but it is not an absolute requirement. It was used to increase the maximum available power density at the tag's location, which is beneficial when tagged objects are measured, and moreover because it was freely available. This leads to a '+' in this criterion.

Configuration Probe-RX-C: Requires both, an additional PA and VSA leading to the most complex hardware compared to the other configurations causing a '-' in this criterion.

The hardware complexity evaluation should emphasize what hardware is needed to give others the change to replicate this configurations and especially a PA and a second VSA are maybe not available in less advanced student labs. Furthermore, the objective to utilize solely off-the-shelf components was achieved.

Power Density at the Tag

This evaluation point analyzes the power density at the tag's location that is, on the one hand, lower bounded by S_{\min} , due the tag's sensitivity and the power margin, as well as upper bounded by S_{max} . Since S_{min} is a property of the utilized tag, and not the configurations, it is not part of the evaluation, and solely S_{max} is determined respectively by evaluating (2.9). To do so, the gain for the pickup antenna was taken from the datasheet [46].

Configuration Probe-TX: For a given S_{\min} (3.8 dBm/m² for the label on Teflon), the achievable dynamic range with this configuration depends on $S_{\rm max}$. Therefore, achieving a large S_{max} is essential. The only limitation is the PA. A maximum power density of 32.0 dBm/m² was achieved, issuing a '+' in this criterion.



Configuration Probe-RX: Unlike configuration Probe-RX, the dynamic range is not limited by S_{max} . Moreover, the low-loss link between the pickup antenna and the tag puts less requirements for a large S_{max} , which would only apply if tagged objects are measured. However, the pickup antenna accepts a maximum of $30 \,\mathrm{dBm}$ on its feed resulting in a S_{max} of 20.3 dBm/m². In comparison, the probe accepts roughly 52 dBm on its feed, and hence, the evaluation for this configuration cannot be made based on the value of S_{max} , but rather on whether if it limits the configuration in achieving a certain dynamic range, which is not the case, therefore causing a '+' in this criterion.

Configuration Probe-RX-C: The same considerations as for configuration Probe-RX apply here, but with including an additional coupling loss reducing S_{max} to $12.6 \, \text{dBm/m}^2$. This causes that in some measurements with tagged objects the tag could not be activated, therefore issuing a 'o' in this criterion.

Dynamic Range 4.3.4

An essential aspect of the measurement configurations' performance is the evaluation of their achieved dynamic range. In the context of the $\sqrt{\Delta RCS}$ characterization, the dynamic range is understood as the span between the largest and the smallest $\sqrt{\Delta RCS}$ that can be detected. In addition the SNR within the achieved dynamic range is of interest. Note that limitations on the dynamic range or the SNR may also arise from non-robust postprocessing methods (cf. FFT Method and Correlation Method) besides the limitations due to the hardware setup.

Introduction to the Measurement

To determine the dynamic range, the tag was aligned in co-polarization to the probe and a electro-mechanical step attenuator from Rohde & Schwarz was utilized to attenuate the signals. The step attenuator can be easily included in the measurement setup, as well in the automated measurements via VISA commands, and it allows to attenuate the $\sqrt{\Delta RCS}$ in constant steps, to determine the dynamic range in equidistant steps. For the dynamic range evaluation of configuration Probe-TX, the attenuator is placed on the transmit path to the chamber and for the evaluation of configurations Probe-RX and Probe-RX-C, it is placed in the receive path from the chamber, as indicated in Figure 4.2 in blue and red, respectively.

Note that solely attenuating the entire backscattered signal before recording it with the VSA is not enough. To infer the dynamic range, the situation, where a strong leaking RF carrier and a comparatively weak backscattered signal from the tag, are both present at the VSA simultaneously, needs to be reassembled. The strong RF carrier is potentially driving the instruments frontend into saturation, causing that the backscatter response cannot be successfully decoded. Since not only the backscattered response is recorded at the instrument, but also the reference signal for the phase calibration (Section 3.2.3), which is in fact a portion of the RF carrier, the situation can be reassembled, by adjusting the level of the reference signal to the signal level of the backscattered signal as it would occur under the best condition, and then attenuating the backscattered signal, while leaving the reference signal constant. As a consequence, the VSA see's a strong RF carrier from the reference signal and simultaneously an attenuated backscattered response. The step attenuator comes with an attenuation range from 0...139 dB which is sufficient for a thorough investigation on the dynamic ranges. Note that this procedure only applies for



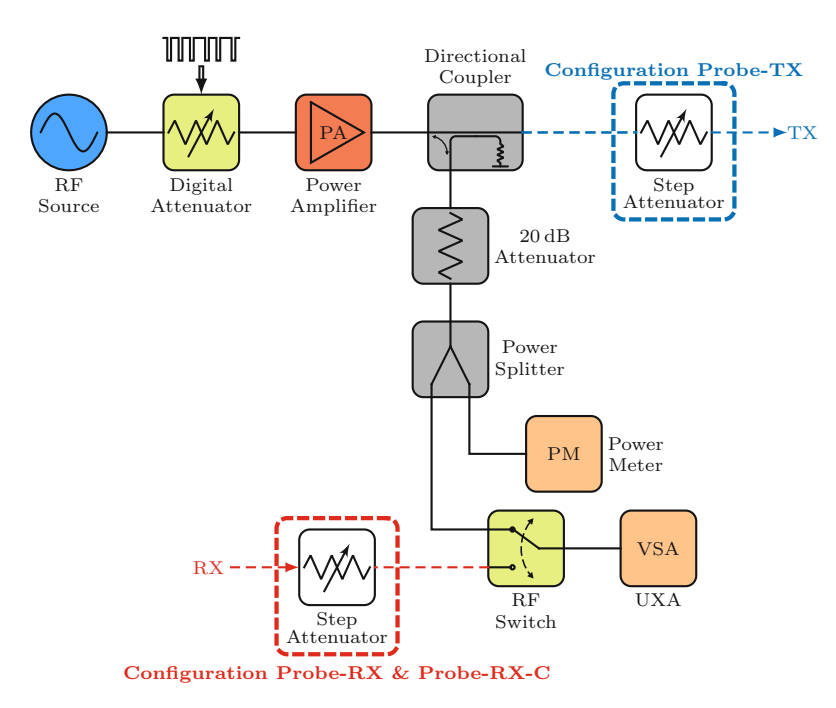


Figure 4.2: Setup for evaluating the dynamic range of each configuration. Modifications are indicated in blue for configuration Probe-TX and in red for configurations Probe-RX and Probe-RX-C.

the backscatter link limited configurations Probe-RX and Probe-RX-C. Since configuration Probe-TX is forward link limited it's dynamic range is determined by the maximum power density at the tag as discussed previously.

To compute the SNR, a significant number of repetitions in each attenuation step is required and for the present analysis, 200 measurements per dB-step were performed, which was found as a trade-off between accuracy and measurement duration. In each dB-step the complex-valued mean of the $\sqrt{\Delta RCS}$ samples is determined by

$$\overline{\sqrt{\Delta\sigma}}_{\text{co}} = \frac{1}{N} \sum_{i=1}^{N} \sqrt{\Delta\sigma}_{\text{co},i} , \qquad (4.1)$$

and afterwards converted on a logarithmic scale and referenced to one square meter (dBsm) by

$$\overline{\Delta\sigma}_{co} = 20 \log_{10} \left(\frac{\left| \overline{\sqrt{\Delta\sigma}_{co}} \right|}{\sqrt{1 \, \text{m}^2}} \right) . \tag{4.2}$$

Although (4.1) and (4.2) are straightforward they are stated specifically, because $\overline{\Delta\sigma}_{co}$ should not be understood as a mean of ΔRCS samples (cf. (3.22)) which are a power quantities thus exclude phase information. Instead $\overline{\Delta}\sigma_{\rm co}$ should be understood as the mean of field quantities, i. e., of $\sqrt{\Delta RCS}$ samples which are then converted to a logarithmic scale. This is important because excluding the phase increase the SNR artificially. To compute the SNR the standard deviation must be calculated first according to

$$s = \sqrt{\frac{1}{N-1} \sum_{i=1}^{N} \left(\sqrt{\Delta \sigma_{\text{co},i}} - \overline{\sqrt{\Delta \sigma}_{\text{co}}} \right)^2} , \qquad (4.3)$$

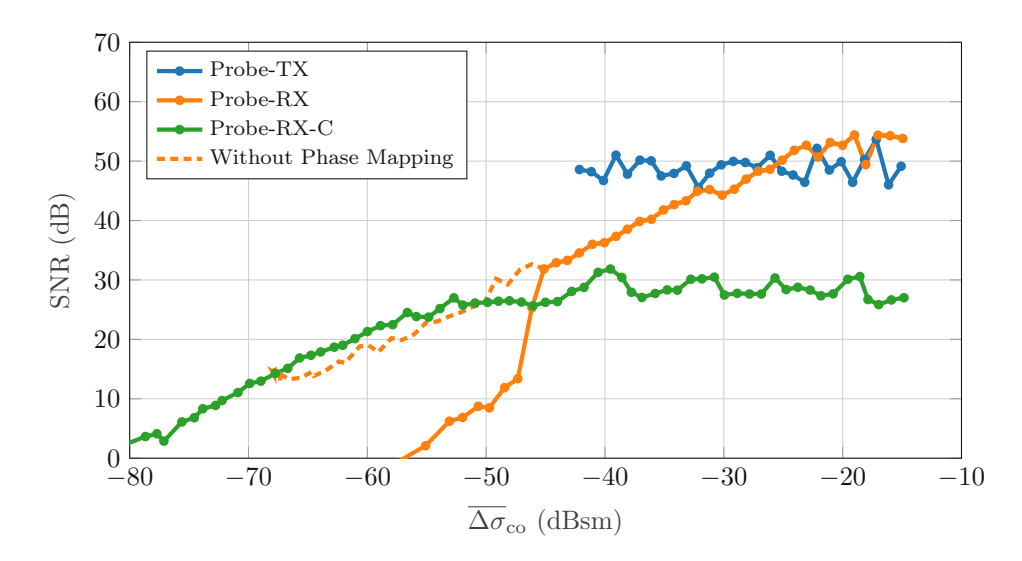


Figure 4.3: Comparison of the achieved dynamic ranges, conducted with the Ucode7 label on Teflon and aligned in co-polarization to the probe at $\theta = 0^{\circ}$.

and then together with (4.1) embedded in

$$SNR = 20 \log_{10} \left(\frac{\left| \overline{\sqrt{\Delta \sigma}_{co}} \right|}{s} \right) . \tag{4.4}$$

The mean signal-to-noise ratio (\overline{SNR}) achieved in the dynamic range that is common to all configurations, is then calculated by simply taking the mean of the SNR values (in linear scale) within this shared range.

Results and Discussion

In Figure 4.3 the computed SNR (in dB) is shown as a function of the mean delta radar cross-section (ΔRCS) denoted as $\Delta \sigma_{co}$ (in dBsm) for each configuration, respectively. Additionally, the results obtained by the FFT Method without resolving the phase ambiguity are plotted.

Configuration Probe-TX: Achieves a dynamic range of 28.1 dB and, within this range, a very high $\overline{\rm SNR}$ of 48.8 dB. It exhibits uncertainties in the SNR because consecutive Δ RCS differ significantly in the achieved SNR. The maximum SNR, which is 53.6 dB, is 8.1 dB apart from the minimum SNR which is 45.5 dB.

Qualitatively, this configuration behaves as expected. The low-loss and (χ, θ, ϕ) -independent link quality on the backscatter path leverages that if a tag can be activated, it can also be read with high SNR. As previously mentioned and now validated, the only limitation on the dynamic range of this configuration, is the available output power of PA. Simply put, the more power is available, the larger the dynamic range' span.

Configuration Probe-RX: Reveals that a large $\overline{\Delta RCS}$ can be represented with very high SNR with a overall maximum of 54.4 dB. After a small range where the SNR stays approximately constant, except for one outlier, the SNR decreases linearly with the ΔRCS with a gradient of approximately 1. At a $\overline{\Delta RCS}$ of roughly -45 dBsm the SNR drops from about 32 dB to 13 dB and then approaches linearly to zero. Configuration Probe-RX

utilizes the FFT Method and Figure 4.3 also includes a dashed orange trace indicating the case, if the FFT Method is applied without the phase mapping. It can be seen that at the breakpoint $(\overline{\Delta RCS} = -45 \, dBsm)$, the dashed orange curve continues in the same manner as the orange curve before the breakpoint. This trend continues until the $\overline{\Delta RCS}$ reaches roughly -68 dBsm represented by a SNR of roughly 15 dB. Once this point is reached, no further change occurs, even though SNR would still be available. Hence, without the phase mapping the dynamic range can be extended by 13 dB to 53.2 dB. The SNR is 47.9 dB

In contrast to configuration Probe-TX, the factor limiting the dynamic range's span is not the available power of the PA, it is the phase mapping. Below a $\triangle RCS$ of roughly -45 dBsm, the SNR drops rapidly which is due to phase assignments into the wrong quadrant. If the phase mapping is not pursued, this drop does not occur and the limit is at an $\overline{\Delta RCS}$ of $-68\,\mathrm{dBsm}$, but with the drawback of introducing a phase ambiguity of 180°. At this point the FFT of the tag response reaches the noise floor.

Configuration Probe-RX-C: Reveals an almost constant SNR in a range of the $\overline{\Delta RCS}$ from the maximum of roughly $-15 \,\mathrm{dBsm}$ to roughly $-53 \,\mathrm{dBsm}$. Then the SNR decreases with a gradient of roughly 1 of the $\overline{\Delta RCS}$ until it reaches zero at a $\overline{\Delta RCS}$ just below 80 dB. Hence, the dynamic range is 66.2 dB and the SNR is 28.7 dB. Also in this range, it seems that this configuration suffer from an uncertainty in the SNR. The maximum SNR is 31.8 dB and the minimum 25.9 dB which equates to a difference of 5.9 dB.

The limiting factor in this configuration is clearly the monostatic support since it inevitably introduces significant self-interference. It is revealed in the high $\overline{\Delta RCS}$ regime where other configurations achieve a significant higher SNR. Nevertheless, it achieves the largest dynamic range of 66.2 dB compared to the other configurations and therefore, it is concluded that by combining a bistatic arrangement with a monostatic support the dynamic range can be extended by more than 25 dB.

4.4Long-Term Stability Issues

Throughout the evaluation of the dynamic range, the measurements, took a long time (sweeping over 70 dB attenuation while taking 200 measurements respectively) and moreover the analysis of the measurement data conducted with configuration Probe-TX and Probe-RX-C indicated uncertainties. This gave rise to perform a long-term measurement under static conditions, i.e., no attenuation, no source power adjustments, no spherical position change, just the pure measurements repeated in 1.8 s time intervals with the tag aligned in co-polarization and the probe located at $\theta = 0^{\circ}$ conducted with configuration Probe-RX-C.

After the computation of the respective $\sqrt{\Delta RCS}$ values from the measurements over time, an oscillating behavior in magnitude and phase, with a time period of roughly 3 h was observed. The peak-to-peak amplitude was 0.35 dB and the peak-to-peak phase was 1.39°. To find the root of this cause, the measurement setup as well as the instruments and the respective settings were checked. It was found that depending on the alignment setting of the UXA (the PXI does not have this feature), the $\sqrt{\Delta RCS}$ amplitudes were either clipped or not. That is, if the automatic alignment was on, the UXA performed a clipping on the amplitude, if it was off, it revealed the uncorrected oscillation. By allowing the UXA to perform expired alignments before measurements, the peak-to-peak amplitude of the $\sqrt{\Delta RCS}$ oscillation was reduced to 0.21 dB but the peak-to-peak phase even increased to

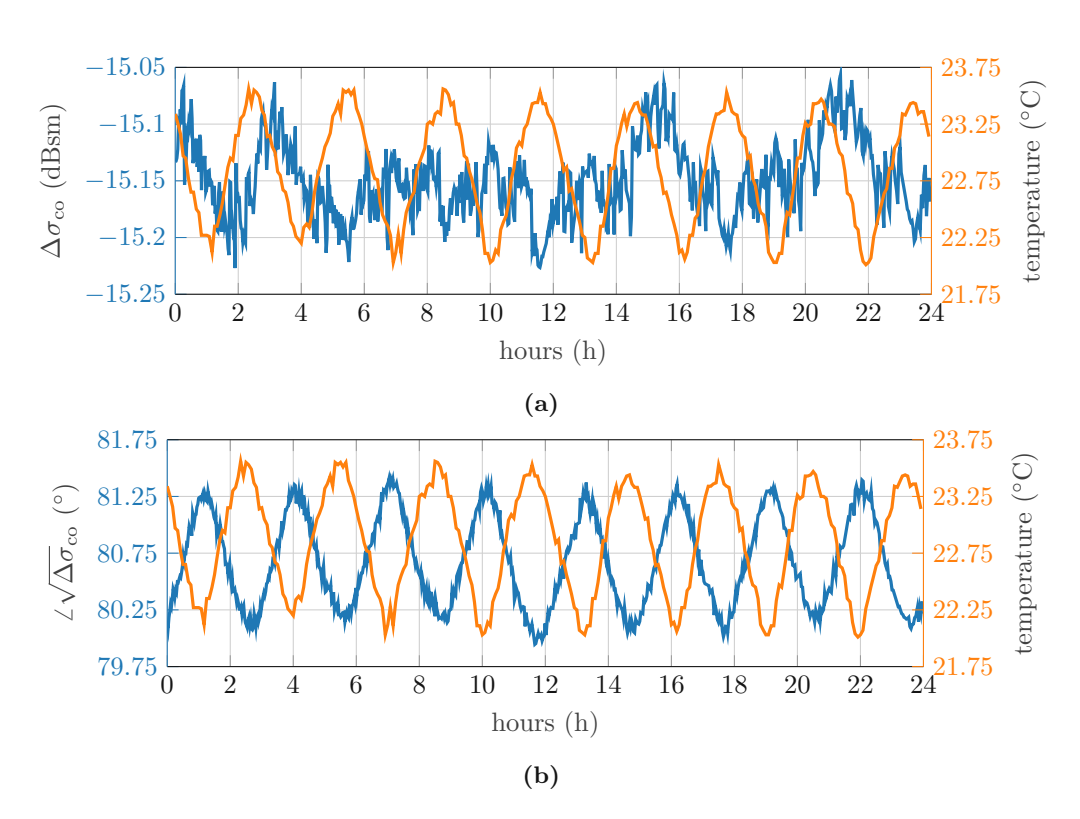


Figure 4.4: Analysis of the long-term $\sqrt{\Delta RCS}$ stability conducted with the Ucode7 label on Teflon and aligned in co-polarization to the probe at $\theta = 0^{\circ}$: Magnitude in (a) and phase in (b) together with the temperature in the measurement hall in orange.

1.64°. The UXA performs alignments of its submodules to compensate for magnitude and phase drifts over time and temperature.

Since this was not the solution to the oscillating behavior the room temperature over time in the measurement hall was observed. See Figure 4.4, where Figure 4.4a depicts the ΔRCS magnitude in blue together with the room temperature in the measurement hall in orange. The $\sqrt{\Delta RCS}$ phase is visualized in Figure 4.4b also in blue and together with the room temperature in orange. In Figure 4.4a the clipping may not be so easily recognizable but it should still be possible. In contrast what is clearly visible is the behavior of the phase in Figure 4.4b and the room temperature which approximately have the same periodicity. This gives an indication that the $\sqrt{\Delta RCS}$ oscillation is induced through room temperature changes. Nevertheless the air conditioning system in the measurement hall uses a temperature corridor of 1.5 °C which is exactly met.

A possible reason for the oscillations could be thermal expansion effects on the coaxial cables. A 14 m long cable from the connector outside the chamber to the probe and a 8.5 m long cable from the pickup antenna to another connector outside the chamber are installed. The specification of the former cable can be found online [47] which is a flexible coaxial cable with foam polyethylene (PE) as dielectric medium and also PE as jacket. The inner conductor material is a copper-clad aluminum wire and the outer conductor material is corrugated copper. The datasheet itself does not state any thermal expansion behavior but it is well-known that coaxial cables that use foam PE as the dielectric are subject to significant changes in their electrical length when exposed to temperature variations. This is due to the relatively high coefficient of thermal expansion (CTE) typically around $100 \cdot 10^{-6} \dots 200 \cdot 10^{-6} / K$.

For example, the 14 m coaxial cable with foam PE dielectric will experience a length change corresponding to a phase shift which can be calculated by

$$\Delta L = L_0 \,\alpha_{\rm PE} \,\Delta T = 14 \,\mathrm{m} \cdot 150 \cdot 10^{-6} /\mathrm{K} \cdot 1.5 \,\mathrm{K} = 3.15 \,\mathrm{mm} \,\,.$$
 (4.5)

For foam PE with an effective relative permittivity $\varepsilon_{\rm r,eff}$ of approximately 1.5 the wavelength λ at 867.5 MHz is

$$\lambda = \frac{c_0}{f\sqrt{\varepsilon_{\text{r,eff}}}} = \frac{3 \cdot 10^8 \,\text{m/s}}{867.5 \cdot 10^6 \,\text{Hz}\sqrt{1.5}} = 282.4 \,\text{mm} \,\,, \tag{4.6}$$

which corresponds to a phase change of

$$\Delta_{\varphi} = 360^{\circ} \frac{\Delta L}{\lambda} = 360^{\circ} \cdot \frac{3.15 \,\text{mm}}{282.4 \,\text{mm}} \approx 4^{\circ} \ .$$
 (4.7)

Conclusively, even a temperature increase of 1.5 °C results in a phase shift of roughly 4°. To reduce the impact of the cables, a down conversion of the backscatter signal could solve this issue by using the distributed frequency converters at the θ -stage and the ϕ -stage.

Truncated-Sphere $\sqrt{\Delta RCS}$ Pattern 4.5

Now, a truncated $\sqrt{\Delta RCS}$ pattern conducted with the label on Teflon and utilizing configurations Probe-RX and Probe-RX-C is presented. The dimension of the label on Teflon together with the required sampling step size $\Delta_{\theta\phi}$ is listed in Table 4.2. Besides that, the dimensions of the label in free space, which will be utilized in Chapter 5 are listed. To introduce the measurement procedure, the label on Teflon was placed on the support structure, aligned with the naked eye such that the labels radiation nulls point in the y-direction of the measurement sphere. See Figure 4.5 for a visualization of the placement.

The patterns conducted by the both configurations are tabulated on a spherical coordinate system and polarization basis. They are visualized in Figure 4.6 where the pattern conducted with configuration Probe-RX is depicted in Figure 4.6a and the pattern conducted with configuration Probe-RX-C is depicted in Figure 4.6b. The $\sqrt{\Delta}$ RCS is separated into magnitude (left) and phase (right) and in its polarization components. The magnitude of the $\sqrt{\Delta RCS}$ is represented via the ΔRCS in dBsm and the phase in degrees (°). A glance at Figure 4.6 reveals that both configurations produce qualitatively the same outcome. The patterns exhibit similarity to that of a theoretical dipole in y-orientation, which was expected, since the label antenna is a meandered dipole. Sources of error such as the impact of the support structure, reflections stemming from the absorbers or offset positioning are not compensated. Due to the scan area truncation, a significant part of the pattern is missing. This part cannot simply be neglected as the requirement on the $\sqrt{\Delta RCS}$ characterization method is to allow for a full-sphere characterization. Therefore, the truncation will be addressed in the next chapter.

Table 4.2: Dimensions of the label on Teflon or in free space.

Label	Length (mm)	Width (mm)	Height (mm)	MRE (mm)	$\Delta_{\theta\phi}$ (°)
Free Space	74	18	0.16	38	18
On Teflon	165	40	10.16	85	15





Figure 4.5: The Ucode7 label on Teflon mounted on the tag support structure.

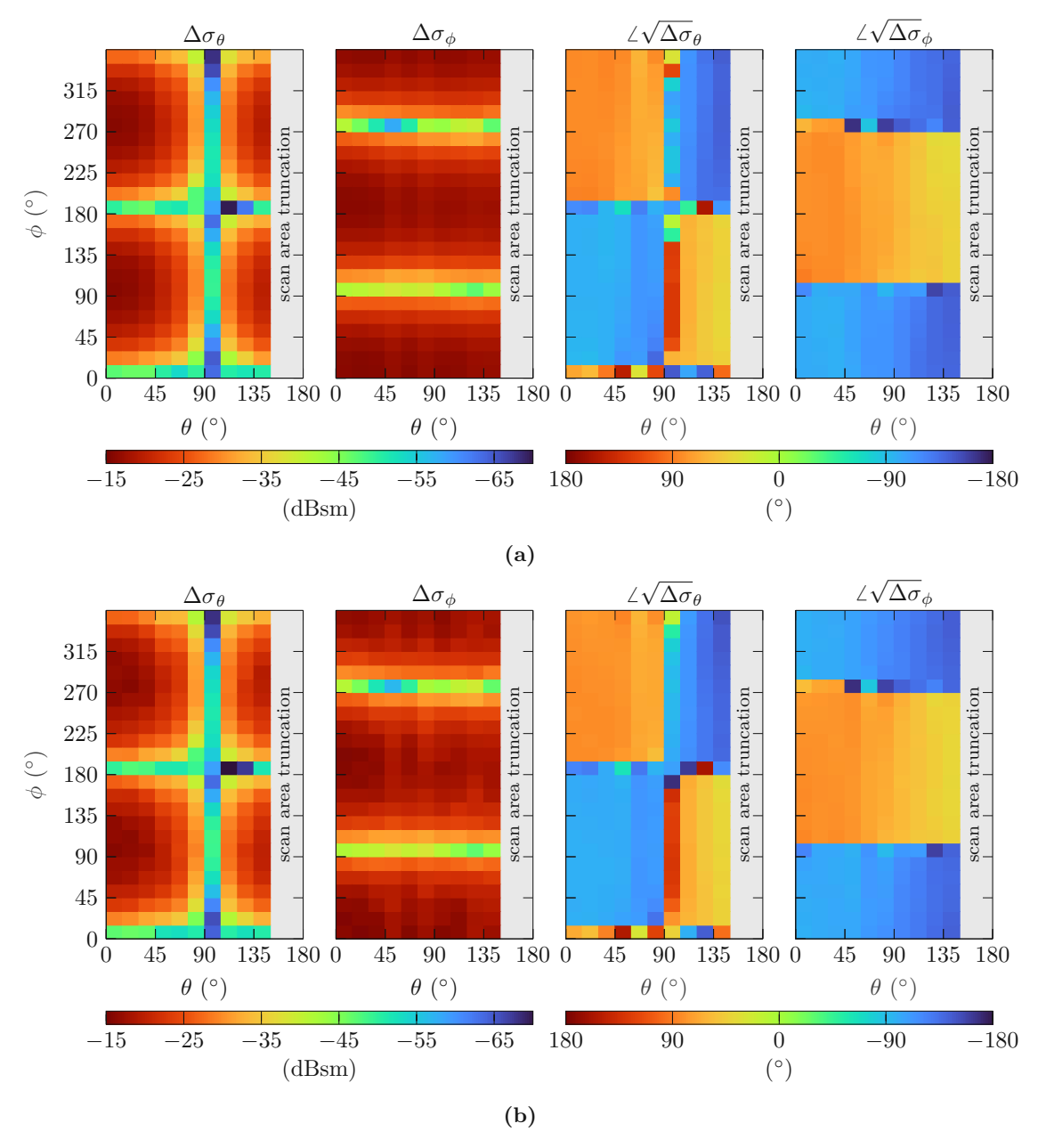


Figure 4.6: Truncated-sphere $\sqrt{\Delta RCS}$ patterns of the Ucode7 label on Teflon: In (a) conducted with configuration Probe-RX and in (b) with configuration Probe-RX-C.



Chapter 5

Expansion to the Full Sphere

The $\sqrt{\Delta RCS}$ characterization method has been implemented and its performance evaluated on a truncated sphere, the next step is to expand the $\sqrt{\Delta RCS}$ characterization onto the entire sphere.

To overcome the θ -truncation, pattern stitching [26] is utilized. In pattern stitching, the idea is to measure the AUT from two orientations to obtain samples that cover the entire measurement sphere together. Unfortunately, the measurements cannot simply be put together afterwards, because each change of the AUT's orientation relative to the measurement coordinate system likely introduces positional offsets of the AUT from the center of the measurement sphere. Therefore, the measurements must be aligned to the same coordinate system before they can be stitched together, which requires coordinate system translation and rotation. Such operations can be performed on SWCs, but to do so, the SWCs must be identified first. A prerequisite enabling the determination of the SWC in the first place is that the E-field radiated by an AUT can be expanded into weighted spherical wave functions [25], where the weighting coefficients are the SWCs. Nevertheless. they can only be determined accurately if the measurements are conducted over the entire sphere, which is due to the θ -truncation not possible. Without going into detail now how pattern stitching addresses this challenge: Sections 5.1 and 5.2 give an introduction to the SWE and pattern stitching. Then, an AUT offset compensation, developed within this work, is presented in Section 5.3. Finally, the full-sphere $\sqrt{\Delta RCS}$ patterns of labels, either in free space or attached to objects, are investigated in Section 5.4. Moreover, pattern stitching includes performance metrics implemented to evaluate the quality of the acquired measurement data. This is of interest because it provides additional insight into the performance of the $\sqrt{\Delta RCS}$ characterization method. This chapter concludes with a short summary in Section 5.5.

Introduction to the Spherical Wave Expansion 5.1

The SWE is a powerful tool to determine the field radiated from an AUT at any point (r, θ, ϕ) , up to the smallest sphere enclosing the AUT centered at the origin, from spherical (near-field) measurements. This builds upon the fact that the E-field radiated by the AUT can be expanded into weighted spherical wave functions by [25] (assuming and suppressing the $-j\omega t$ time convention)

$$\mathbf{E}(r,\theta,\phi) = k\sqrt{Z_0} \sum_{smn} Q_{smn} \mathbf{F}_{smn}(r,\theta,\phi), \tag{5.1}$$

where $\mathbf{F}_{smn}(r,\theta,\phi)$ denotes the vector spherical wave function (SWF), Q_{smn} the corresponding complex-valued scalar SWC, Z_0 the impedance of the propagation medium, and k the wavenumber. The azimuthal and polar indices m and n, where $|m| \leq n$, specify the order and the degree of the spherical wave, respectively. The index s accounts for



transversal magnetic (TM) and transversal electric (TE) modes with s=1 and s=2, respectively. The summation in (5.1) is understood as

$$\sum_{smn} = \sum_{s=1}^{2} \sum_{n=1}^{\infty} \sum_{m=-n}^{n} . \tag{5.2}$$

Having the field samples at hand, one seeks a solution to the inverse problem, i.e., determining the SWCs. Once the SWCs are determined, plugging them in the SWE enables an analytical field description leveraging field information at any point (r, θ, ϕ) at larger distance than r_0 , in free space. The radius r_0 , which is also referred to as the minimum radial extent (MRE) describes the radius of the smallest sphere, measured from the origin of the measurement coordinate system which encloses the entire AUT. Nevertheless, even if assuming ideal measurement conditions, i. e., without noise, positioning errors, full-sphere coverage, an infinite number of samples would be needed to determine all the SWCs. This is, because the expansion in (5.1) is of infinite length. Fortunately, in practical cases, considering antennas of limited extent, not all spherical modes contribute significantly to the radiated field. Therefore, truncating the polar index at some n=Nand further M=N, if no prior knowledge about the AUT exists, is common practice. The empirical rule [25]

$$N = \lfloor kr_0 \rfloor + n_1 \tag{5.3}$$

has been established where n_1 is a constant depending on the desired accuracy, and according to Hansen [25], $n_1 = 10$ is sufficient for most practical cases.

It is important to note that, since the \sqrt{RCS} is based on field quantities and proportional to the radiated field, the application of the SWE is justified. The same holds true for the $\sqrt{\Delta RCS}$ which is the superposition of two \sqrt{RCS} values, and since the SWE is linear, any linear combination of solutions of the SWE is a valid solution.

5.2Introduction to Pattern Stitching

The author in [26] proposed a novel method to compute full-sphere patterns from truncated (near-field) measurements by taking advantage of the fact that an antenna can be measured in multiple orientations, leveraging that field samples over the whole sphere are obtained. In the present implementation, two truncated patterns stemming from measurements in two different AUT orientations, which together cover the entire measurement sphere, are needed. However, measurements in different orientations require physically rotating the AUT, therefore the antenna's orientation with regard to the measurement coordinate system changes as well. To be able to stitch such patterns together, they must be aligned to the same coordinate system, which requires coordinate system translation and rotation. Translation and rotation operations can be done on SWCs, but one has to keep in mind that the SWCs can only be determined accurately if the field samples are obtained over the full sphere and further are not distorted by noise or measurement uncertainties. A consequence of not covering the full sphere is that the inverse problem becomes underdetermined causing that although the found solution is one of the possible combinations of the SWCs, there is no guarantee that they represent the real SWCs associated with the AUT in any way. In the worst case this can lead to a nonphysical field distribution, hence these effects combined render the computation of the SWCs rather difficult. The author refers to it as the calculation of truncated SWCs. Keeping one truncated pattern fixed, the alignment

procedure of the stitching method manipulates the truncated SWCs of the second truncated pattern via translation and rotation operations in the condition of minimizing a mean square error metric in the overlapping region between them. After alignment of the second pattern to the coordinate system of the first pattern, the patterns are stitched together using a hemisphere split approach. That is, taking the upper hemisphere of the fixed pattern and combining it with the lower hemisphere of the aligned second pattern.

In order to guide pattern stitching towards a physically meaningful solution that can be associated with the AUT it is important to consider in advance the orientation of the AUT on the positioner system and further the rotation axis around which the AUT is rotated. In the present implementation rotations about the x- and the y-axis are allowed. This becomes crucial when measuring tagged objects which are large compared to the tag.

The author further proposed a scaled mean square error (SMSE) metric, which compares stitched patterns to the original measurement data in the overlapping region in the least squares sense,

$$SMSE = \frac{1}{K_{\text{overlap}}} \frac{\sum_{\chi, \theta_{\text{overlap}}, \phi} |w(\chi, \theta, \phi) - \hat{w}(\chi, \theta, \phi)|^2}{\max_{\chi, \theta_{\text{overlap}}, \phi} |w(\chi, \theta, \phi)|^2}, \qquad (5.4)$$

where K_{overlap} is the total number of points in $(\chi, \theta_{\text{overlap}}, \phi)$, w the array containing the measurement data, and \hat{w} the array containing the stitched pattern. Note that although it is a single L2-metric, it is used throughout this chapter in two different scenarios, once before and once after performing pattern stitching. Consequently, it is referred to as an SNR estimate when utilized to compare the measurement data against the estimated field pattern after the computation of the truncated SWCs for the partial measurements and it is referred to as a SMSE when utilized after pattern stitching. The SNR estimate describes how well the measurement data can be represented by the SWE and the SMSE describes how well the partial measurements are represented in the final full-sphere pattern.

5.3 Offset Compensation

Note that (5.3) does not account for an AUT in offset position, i. e., a situation where the AUT is not centered in the measurement sphere. If so, a possible offset must be included and, hence, the radius of the minimum sphere increases with the offset

$$r' = r_0 + |\mathbf{r}_{\text{offset}}| = r_0 + \sqrt{x_{\text{offset}}^2 + y_{\text{offset}}^2 + z_{\text{offset}}^2}$$
 (5.5)

Besides that, also the number of spherical modes increases $(N' = |kr'| + n_1)$ causing that the radiated power of an AUT, which is expressed as [25]

$$P = \frac{1}{2} \sum_{smn} |Q_{smn}|^2 , \qquad (5.6)$$

distributes towards modes of higher index n. This is simply due to the higher phase variation in an offset position. For example, a small electrical dipole is solely characterized by SWCs of order n=1 and the total radiated power is confined in these coefficients, but only if the dipole is located in the origin of the coordinate system [25]. If it is shifted by some offset $\mathbf{r}_{\text{offset}}$, the radiated power distributes to modes of higher index n, although the AUT remains the same consequently the total radiated power must be the same. Such a situation is presented in Figure 5.1, where the SWCs of an y-oriented small dipole at 867.5 MHz are depicted on a logarithmic scale. In Figure 5.1a centered and in Figure 5.1b translated by $\mathbf{r}_{\text{offset}} = \lambda[-1/4, 1/4, 1/2]$. Recall that the azimuthal order m is upper bounded by n causing that the white space in each of the figures represents mathematically impermissible SWCs. On the contrary, the dark blue area represents mathematically permissible SWCs. Note that a small dipole in y- and in x-orientation is described by $m=\pm 1$ whereas in z-orientation it is described by m=0 [25]. Further, for an electric dipole holds SWCs in s=2 and if instead a magnetic dipole is considered SWCs in s=1true.

Conversely, if the total radiated power is confined within SWCs of lower index n it implies that the AUT is close to the origin of the measurement coordinate system. Hence, the idea is to shift an offset AUT to the origin of the measurement coordinate system by finding an offset vector $\mathbf{r}_{\text{offset}}$ for which a mathematical translation of the AUT causes that the radiated power redistributes to modes of lower index n. The redistribution is accomplished by weighting each row n with its index and further a tuning factor c, thus

$$\mathbf{r}_{\text{offset}} = \underset{\mathbf{r} \in \mathbf{r}_{\text{set}}}{\text{argmin}} \sum_{smn} n^c |\mathbf{Q}_{\text{smn}}|^2 , \qquad (5.7)$$

where \mathbf{r}' is drawn from a set of permitted offset vectors \mathbf{r}_{set} . The implementation in Matlab is done by utilizing the fmincon optimizer and it was found that the choice of c is uncritical because for tested values in a range of $1 \dots 2$, it was observed that for c = 1 a similar mean square error (MSE) compared to c=2 could be determined, if the number of iterations is increased. However, for the measurements c was set to 1.1 to ensure that it is slightly above linear. The method was validated by simulations with combinations of $\mathbf{r}_{\text{offset}}$ offset vectors applied on the dipole example, i.e. analytical SWCs without noise. The offset compensation will be used in what follows to estimate positional offsets prior to comparing the patterns.

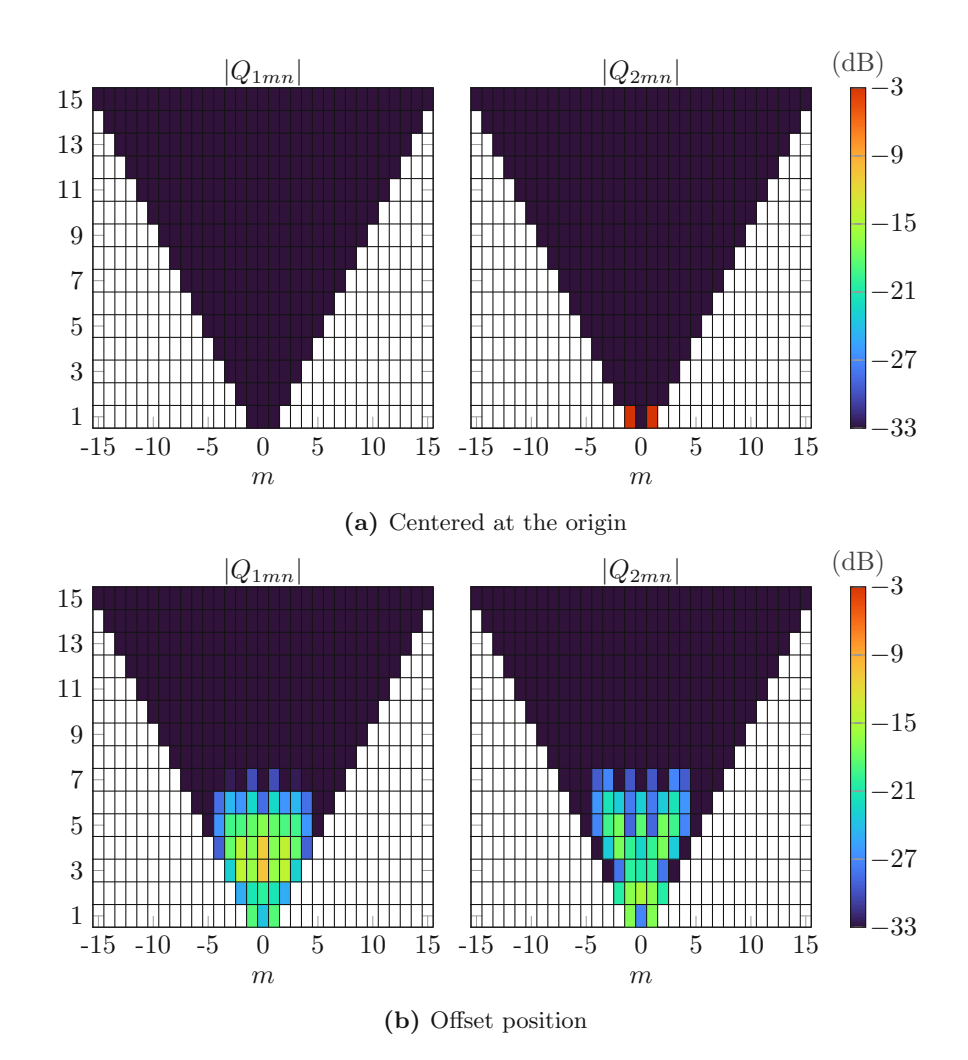


Figure 5.1: Comparison of analytical SWCs of a y-oriented small electrical dipole at 867.5 MHz on a logarithmic scale: Centered at the origin in (a) and in offset position $\mathbf{r}_{\text{offset}} = \lambda[-1/4, 1/4, 1/2]$ in (b).

Applied Scenarios 5.4

Results from applying pattern stitching and the offset compensation to different measurement scenarios are investigated now. First, the truncated-sphere $\sqrt{\Delta RCS}$ pattern obtained from the Ucode7 label on Teflon (cf. Section 4.1), presented in Section 4.5, is revisited and its expansion to the full sphere is shown. This pattern is then compared to the full-sphere $\sqrt{\Delta RCS}$ pattern of the label without the Teflon in free space. Afterwards the label was placed on the side wall of an empty crate and the measurements were repeated. Finally, metal cans were placed inside the crate and the so obtained pattern was compared to that of the empty crate. The specific use of metal cans was motivated by [15], where the tag performance was investigated when attached to crates with various materials inside. This study found that placing plastic or glass inside the crate introduces only minor changes in the magnitude and phase, while placing liquid or metal changes the tag's performance significantly.

Table 5.1: SNR and SMSE for top and bottom hemisphere measurements for the label in free space and on Teflon conducted with configurations Probe-RX and Probe-RX-C together with SMSE results determined after the stitching.

Label	Configuration	SNR (dB)		SMSE (dB)		Offset (mm)		
		Top	Bottom	Top	Bottom	\overline{x}	y	z
In Free Space	Probe-RX	39	38	-30.4	-29.4	-9.6	11.4	25.8
	Probe-RX-C	31	31	-26.1	-25.9	-9.8	11.2	26.4
On Teflon	Probe-RX	45	43	-32.5	-27.5	-3.4	3.9	32.6
	Probe-RX-C	35	35	-29.0	-25.7	-3.3	3.9	33.4

5.4.1 Tag in Free Space

In this scenario the full-sphere $\sqrt{\Delta RCS}$ patterns of the label in free space and on Teflon are presented. Therefore, the top and bottom hemisphere measurements had to be conducted for both labels. Both were positioned identically on the xy-plane with radiation nulls in the y-direction on the support structure, similar to that in Figure 4.5. After the top hemisphere measurement were executed, the labels were rotated by 180° around the x-axis and the measurements were repeated. Configurations Probe-RX and Probe-RX-C (both introduced in Section 3.1), were utilized to perform the measurements but similar as in Chapter 4, the hardware setup of Probe-RX-C was used for both configurations because this setup allows to gather also the data which would be obtained by the setup of configuration Probe-RX and, thus the additional time to rebuild the setup is saved. Afterwards, SNR values of the partial measurements were computed and results are provided, in Table 5.1. Note that Table 5.1 lists several evaluations that will be addressed in the subsequent discussion, for now, the focus is on the SNR. The SNR indicates how well the measurement data can be described by the SWE in the least-squares sense. Three conclusions can be drawn from this evaluation:

- (i) Measurements conducted with configuration Probe-RX exhibit higher SNR than measurements taken with Probe-RX-C. This is consistent with the findings in Section 4.3.
- (ii) Measurements performed with the label on Teflon achieve a higher SNR than that with the label in free space. It was expected since the label needs some dielectric backing to perform, even though the precise dielectric constant is unknown, and the Teflon was empirically found.
- (iii) Top and bottom hemisphere SNR match approximately. Due to the shape of the labels a certain rotational symmetry was expected.

After the stitching was performed, the SMSE was determined to evaluate how well the fullsphere stitched patterns match the partial measurements. Since the partial measurements are truncated, the SMSE computation must be done for the top and the bottom hemisphere measurement independently. The results are listed in the fourth column of Table 5.1 and allow two findings:

- (i) All errors are below $-25 \, \mathrm{dB}$.
- (ii) Top and bottom hemisphere SMSE match approximately.

These findings allow the conclusion that pattern stitching converged successfully towards the optimum solution, which was anticipated due to the high SNR and the small MRE. The latter allows an easy rotation without changing the position of the label on the support structure largely, which essentially means that the alignment procedure only has to perform the rotation but no translation to align the coordinate systems of the partial measurements.

Then, the offsets of the labels were estimated and results, listed in the fifth column of Table 5.1, reveal that both configurations yield similar values for the respective labels, indicating consistency. Since the height of the label in free space is negligible, the z-offset of 25.8 mm and 26.4 mm indicates that the label was not perfectly centered in the origin of the measurement sphere, however, due to the naked eye alignment this is reasonable. The z-offset of 32.6 mm and 33.4 mm for the label on Teflon are then approximately accumulated to the additional height of the Teflon. The x- and y-offsets of both labels appear noticeably small. It would need further investigation by performing measurements while placing the labels intensionally in an known offset position and afterwards determining the offsets to verify the results.

Full-sphere $\sqrt{\Delta RCS}$ patterns of both labels conducted with configuration Probe-RX-C, after the offset compensation, are depicted in Figure 5.2, where Figure 5.2a presents the pattern obtained by the label on Teflon, and Figure 5.2b depicts the pattern obtained by the label in free space. The data is tabulated on a polar spherical coordinate system and resolved onto a polar spherical polarization basis, exactly as it was measured, but with higher angular granularity. The measurements were carried out in 15°-steps and the data is depicted in 5°-steps to provide finer details of the $\sqrt{\Delta}RCS$ pattern. The $\sqrt{\Delta}RCS$ magnitudes $\Delta \sigma_{\theta}$ and $\Delta \sigma_{\phi}$ are expressed on a logarithmic scale and referenced to one square meter. The scales were intentionally maintained to highlight the significantly reduced backscatter strength for the label in free space.

Tag on Object 5.4.2

Now, a tagged object is considered by attaching the label, previously measured in free space, to a crate. A crate made from polypropylene (PP) with dimensions listed in Table 5.2 was selected to perform the measurements. This material resembles roughly similar dielectric properties of Teflon. Note that the label on Teflon is not specified to be attached to Teflon, it is just a tradeoff to provide a backing for the label that roughly resembles the dielectric properties for which the label was designed for. Nevertheless, the label on Teflon revealed a sufficient backscatter strength hence the crate is compared to the Teflon. In contrast to the previous cases, the MRE increased significantly requiring a sampling step size $\Delta_{\theta\phi}$ of 10°. This equates to a total number of $K = K_{\chi}K_{\theta}K\phi = 2 \cdot 15 \cdot 36 = 1080$ sampling points required for a single partial measurement. Having in mind the duration per sample for configuration Probe-TX (cf. Section 4.3), conducting both partial measurements, for a single tagged object scenario, would last in total 9.66 h. In comparison, with configuration Probe-RX-C the total duration is 2.28 h and with configuration Probe-RX it is 1.8 h. Besides that, the main reason why configuration Probe-TX is not utilized when pattern stitching is applied is simply the limited dynamic range leading to an ill-conditioned inverse problem causing that pattern stitching may not converge successfully. Next, measurements conducted with the label attached to the empty crate are presented.

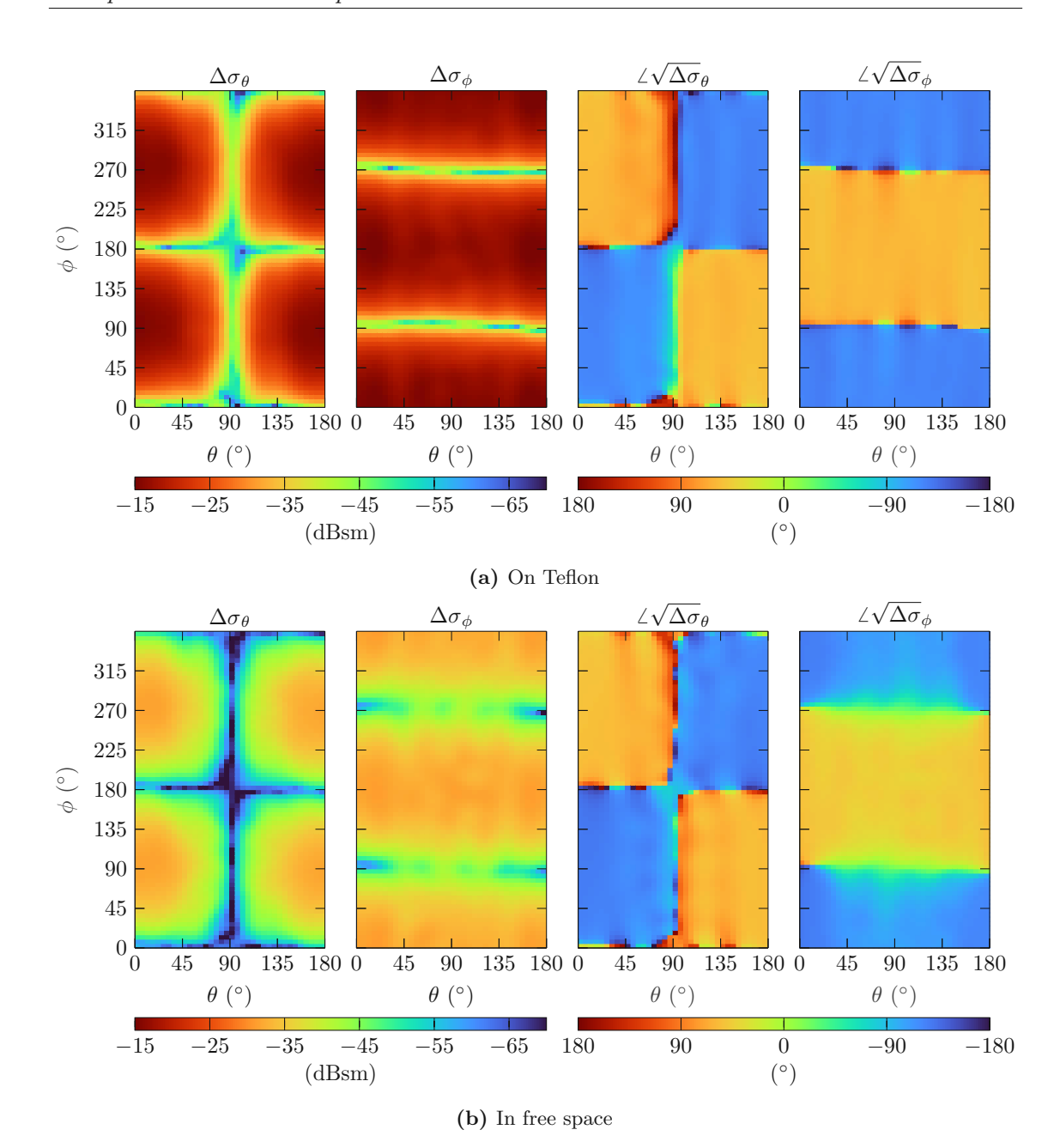


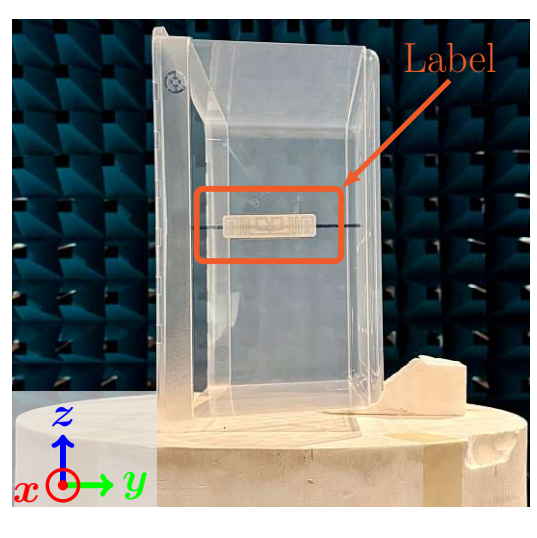
Figure 5.2: Full-sphere $\sqrt{\Delta RCS}$ patterns after offset compensation conducted with configuration Probe-RX-C: Ucode7 label on Teflon in (a) and in free space in (b).

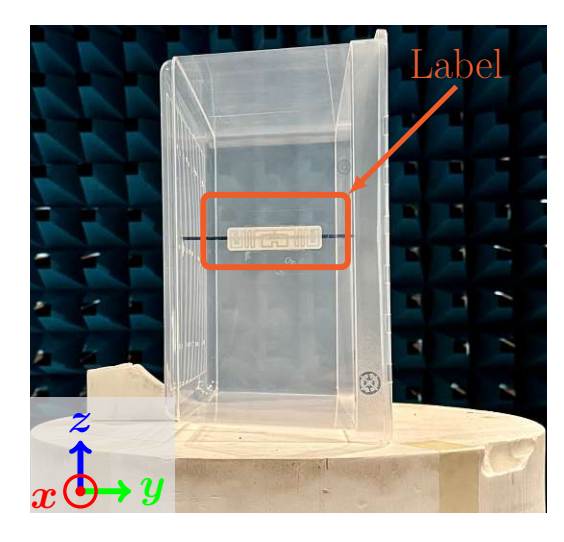
Empty Crate

To conduct a full-sphere $\sqrt{\Delta RCS}$ pattern of the tagged object, the procedure introduced in the preceding section was repeated. To illustrate the measurement situation, the placement and the orientation are depicted in Figure 5.3 where Figure 5.3a depicts the orientation for the top hemisphere measurement and Figure 5.3b for the bottom hemisphere measurement. Since the extent of the misalignment between both measurements is crucial for the convergence of pattern stitching and moreover, a large misalignment might cause not converging towards the optimal solution it is important to support pattern stitching by physically keeping the misalignment as low as possible. To do so, the tag was placed, with radiation nulls in the y-direction, in the center of the side wall on the crate and the

Table 5.2: Dimensions of the crate together with the MRE and the respective sampling step size.

Length (mm)	Width (mm)	Height (mm)	MRE (mm)	$\Delta_{\theta\phi}$ (°)
390	335	180	272	10





(a) Top orientation

(b) Bottom orientation

Figure 5.3: Empty crate tagged by the Ucode7 label: Top orientation in (a) and bottom orientation in (b).

height of the support structure was approximately adjusted such that the center of the crate is in the origin of the measurement sphere. The rotation axis is set as the x-axis because in this case, when rotating the tagged object for the bottom measurement, the position of the label remains and just the orientation changes. Although the entire object is considered as the radiating structure the dominant source of energy is the tag and if the rotation would be done around the y-axis the position of the tag would be mirrored about the y-axis, resulting in an misalignment corresponding to the length (390 mm) of the crate. However, when rotating around the x-axis, pattern stitching must not translate the bottom measurement and only perform the 180°-rotation to align the coordinate systems. It needs to be taken into account that without precision instrumentation such as a laser it is unlikely that the AUT is placed exactly in the center of the measurement sphere so that a minor misalignment will remain but not as large as with the rotation axis in y-direction.

The measurements were carried out with configurations Probe-RX and Probe-RX-C and further SNR estimates prior to pattern stitching, SMSE values after the stitching and estimated positional offsets are reported. Results are listed in Table 5.3. Again, configuration Probe-RX achieves a higher SNR compared to configuration Probe-RX-C. Top and bottom hemisphere SNR are similar for both configurations and the SMSE values are consistent indicating that the stitching converged successfully. The offset of the tagged object to the origin to measurement sphere was estimated and for the same reason as above the label which has indeed an offset in x-direction equal to the half of the crate length (195 mm). Taking into account a misalignment of the entire crate due to the naked eye alignment, the estimated offset of 174.4 mm is in good agreement. Further, the consistency between the configurations validates the estimate.

Table 5.3: SNR and SMSE for top and bottom hemisphere measurements for an empty tagged crate. The measurements were conducted with configurations Probe-RX and Probe-RX-C.

Tagged	Configuration	SNR (dB)		SMS	SMSE (dB)		Offset (mm)	
		Top	Bottom	Top	Bottom	\overline{x}	y	\overline{z}
Empty	Probe-RX	41	41	-31.1	-26.8	174.4	-0.5	18.2
Crate	Probe-RX-C	32	34	-28.8	-25.9	174.3	-0.4	17.8

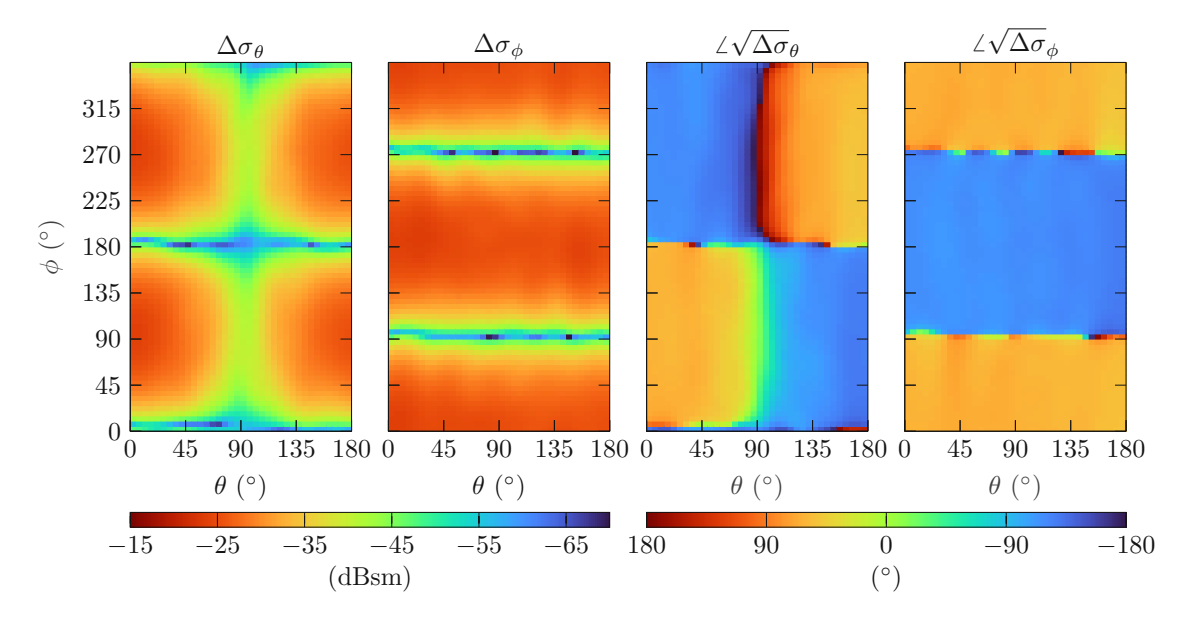
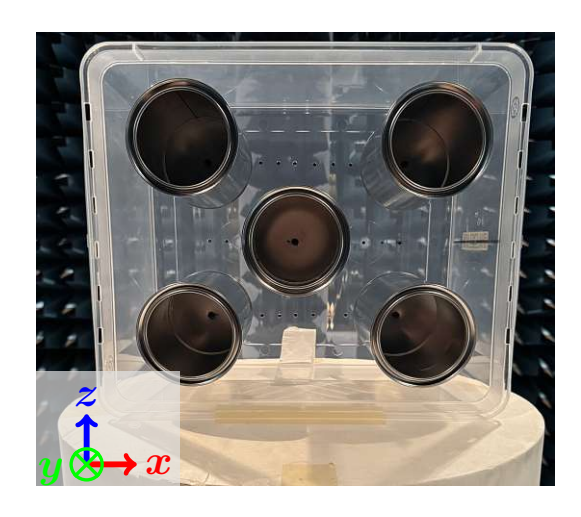


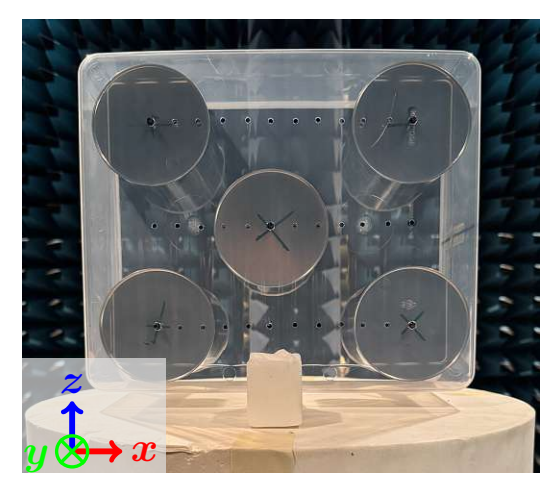
Figure 5.4: Full-sphere $\sqrt{\Delta RCS}$ patterns of the label on an empty crate conducted with configuration Probe-RX-C after applying pattern stitching and offset compensation.

A qualitative assessment of the full-sphere $\sqrt{\Delta RCS}$ pattern after offset compensation and conducted with configuration Probe-RX-C in Figure 5.4 reveals that the magnitude is increased compared to the label in free space (cf. Figure 5.2b) but does not come close to the strength of the label on Teflon (cf. Figure 5.2a). The phase behavior remains consistent with the label on Teflon and in free space. Eventually, although the modified dielectric may introduce minor change in magnitude and phase, the full-sphere $\sqrt{\Delta RCS}$ pattern resembles that of the label on Teflon and in free space very well. Next, the crate is filled with material.

Filled Crate

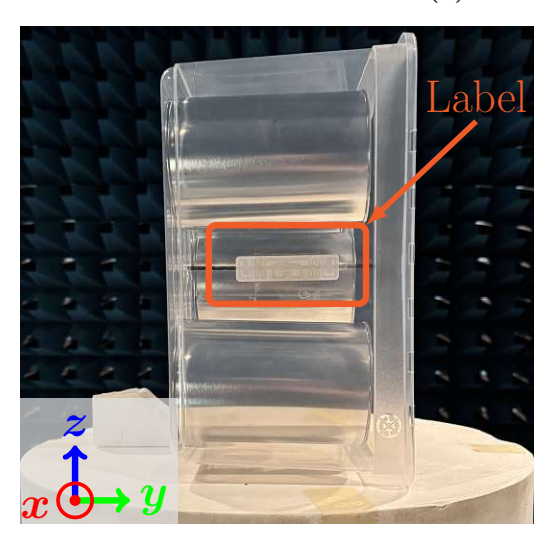
As reported in [15], while plastics or glass will only have minor effects on the magnitude and phase of the radiation pattern, metal or liquid will have a significant impact. Therefore, in this work, metal cans are placed inside the crate. Five cans were placed and it was found that the cans must not be placed too close to the label otherwise it cannot be activated and at least a separation of 80 mm was needed. This is an important finding with respect to phase-based localization, because it suggests that in order to be able to activate the label, regardless of the elements inside the crate, a label or tag with integrated ground plane is needed. On the one hand this would lead to higher costs and on the other their radiation pattern no longer exhibits an omnidirectional behavior which causes that the tag





(a) Top orientation

(b) Bottom orientation



(c) Bottom orientation - side view

Figure 5.5: Filled crate tagged by the Ucode7 label: Top orientation in (a), bottom orientation in (b), and the side view in (c).

can only be read from one hemisphere.

Top and bottom hemisphere measurements are illustrated in Figure 5.5, where Figure 5.5a depicts the top, Figure 5.5b the bottom orientation, and Figure 5.5c the side view of the bottom orientation to visualize the placement of the label.

Since the position of the crate is maintained while filling it with the metal cans, the offset is already known from the previous scenario, and hence the pattern can be compensated by the found offset to allow for a fair comparison of the empty and the filled scenario. A qualitative comprehension of Figure 5.4 with Figure 5.6, both conducted with configuration Probe-RX-C, allows the conclusion that the two $\sqrt{\Delta RCS}$ patterns differ significantly in both, magnitude and phase and across both polarization components.

SNR and SMSE insights are provided in Table 5.4. Compared to the prior scenario where the crate was empty, the SNR and SMSE values have slightly increased which may be explained by the fact that the nulls in the pattern are more distributed, leading to a better

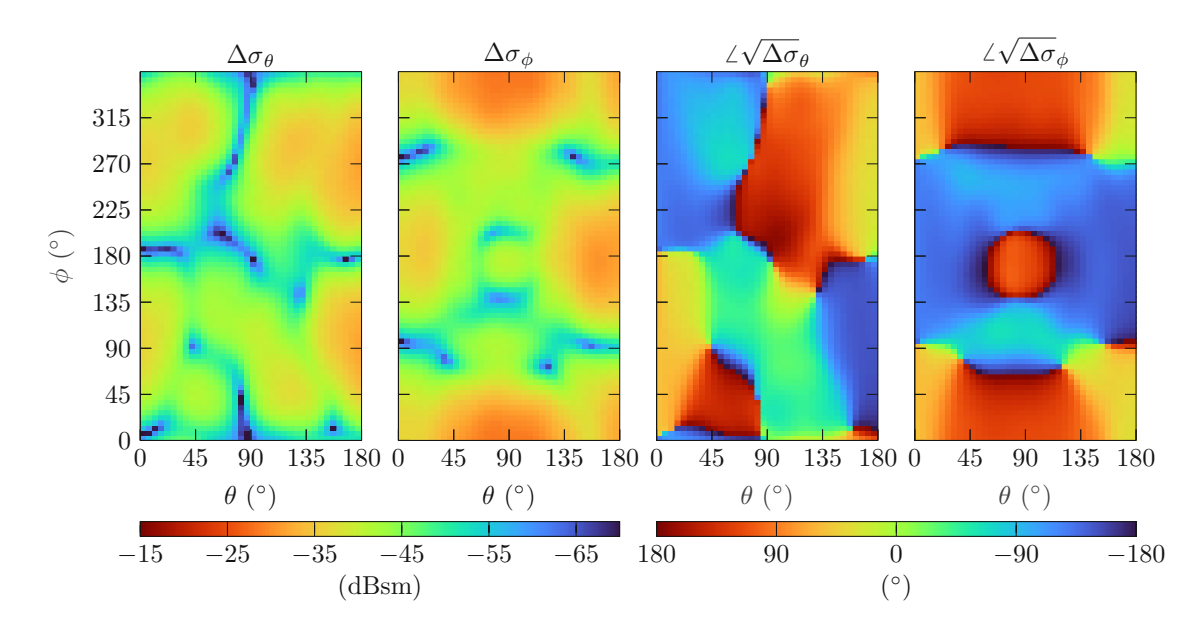


Figure 5.6: Full-sphere $\sqrt{\Delta RCS}$ pattern of the Ucode7 label on a crate filled with five metal cans conducted with configuration Probe-RX-C after applying pattern stitching and offset compensation.

Table 5.4: SNR and SMSE for top and bottom hemisphere measurementsfor a filled tagged crate. The measurements were conducted with configurations Probe-RX and Probe-RX-C.

Tagged	Configuration	SN	R (dB)	SMS	E (dB)
		Top	Bottom	Top	Bottom
Filled	Probe-RX	44	42	-33.9	-29.5
Crate	Probe-RX-C	39	30	-31.4	-27.0

conditioning of the inverse problem when computing the SWCs and consequently a solution that describes the tagged object with higher accuracy.

5.5 Summary

By the utilization of pattern stitching a procedure was presented to expand the so far truncated $\sqrt{\Delta RCS}$ onto the entire sphere. SNR and SMSE values better than 30 dB and $-25\,\mathrm{dB}$ respectively, associated with exemplary stitched patterns from labels in free space or on objects suggest that the measurement data is of sufficient quality allowing pattern stitching to converge towards physically meaningful solutions. This holds true for measurements obtained with configuration Probe-RX and configuration Probe-RX-C. After pattern stitching, an offset compensation, implemented in this work, was applied to the stitched pattern to ensure, that the corresponding SWCs can entirely be associated with the AUT and are not affected by a misplacement of the AUT. Eventually, this enables a fair comparison of measurements. Lastly, it was found that the pattern of the empty crate tagged by a Ucode7 label resembles that of the same label in free space or on Teflon very well but this no longer hold true when material is placed inside.

Chapter 6

Conclusion

Phase-based localization with passive ultra high frequency (UHF) radio-frequency identification (RFID) tags has attracted significant attention in research activities, see [11–17]. Such methods rely on measuring the phase of the received tag signal to determine the tag's position. An accurate phase model must incorporate the phase response of the tag which is typically modeled without any dependency on the spherical direction (θ, ϕ) . While this might hold true for tags with an ideal dipole in free space, it does no longer when the tag is attached to complex objects, where the phase response can indeed exhibit dependency on (θ, ϕ) . The essential parameter for obtaining the phase response is the square root delta radar cross-section ($\sqrt{\Delta RCS}$), which is the complex-valued difference of the tag's two radar cross-sections (RCSs) that are used for backscatter communication. The $\sqrt{\Delta RCS}$ is the rigorous extension to the well-known delta radar cross-section (ΔRCS) and is based on (complex-valued) field quantities rather than on (real-valued) power quantities. A complex-valued description preserves the phase and allows to characterize the phase response in the first place.

From the literature, it is already known that self-interference limits the dynamic range of the measurement system, especially if monostatic arrangements are used. The authors in [22, 24, 41] proposed to employ carrier cancellation to improve the dynamic range at the expense of non-off-the-shelf components and an additionally required control-loop. To address the challenge of self-interference but proceed with off-the-shelf equipment, this work follows a different approach: (i) To employ a bistatic arrangement which inherently reduces the self-interference. (ii) To utilize the spherical wave expansion (SWE) [25] in the post-processing allowing for an continuous field reconstruction based on measurement values. Essentially, this means that the SWE allows to determine the fields even at positions where the measurement system's dynamic range was insufficient and thus effectively lowers the requirements on the measurement system's dynamic range. Moreover, the second antenna is placed on the positioner system in the anechoic chamber such that a (χ, θ, ϕ) -independent low-loss link to the tag can be established. This enables that the tag can easily be activated from this antenna, or easily read (if activated from the other antenna). Several assignments of transmitting and receiving antennas are permitted due to the bistatic arrangement and three of those were systematically elaborated and led to configurations Probe-TX (bistatic, cf. Section 3.1.2), Probe-RX (bistatic, cf. Section 3.1.3), and Probe-RX-C (combined monostatic-bistatic, cf. Section 3.1.4). Configuration Probe-TX tackles the self-interference, configuration Probe-RX addresses a power leveling required with configuration Probe-TX, and configuration Probe-RX-C eliminates the need for a decoder required with configuration Probe-RX. Since the bistatic arrangement introduces an additional uncalibrated signal path from the pickup antenna to the tag, a calibration procedure had to be developed (cf. Section 3.5.3). Reciprocal tag behavior can be assumed therefore absolute calibration can be achieved by reversion of TX/RX and fulfilling the tag's minimum power condition. Using configuration Probe-TX the source power level is increased until the tag can be activated. In the second step configuration Probe-RX is used and the procedure is repeated. 6. Conclusion 63

The found power levels can then be utilized to resolve the unknown path. Although the measurements are bistatic, a calibrated monostatic $\sqrt{\Delta RCS}$ can be determined.

Results have shown that configuration Probe-RX-C achieves the largest dynamic range of 66 dB, followed by configuration Probe-RX-C with 40 dB and configuration Probe-TX with 28 dB. On the contrary, if considering the mean signal-to-noise ratio (SNR) in the mean delta radar cross-section $(\overline{\Delta}RCS)$ that can be measured by all configurations, configuration achieves the highest SNR of 49 dB followed 48 dB obtained by configuration Probe-RX and 29 dB accomplished with by configuration Probe-RX-C. Configuration Probe-TX necessitates a sophisticated power leveling leading of an average duration per measurement sample of 14.1 s, whereas configurations Probe-RX and Probe-RX-C achieve a fixed duration per measurement sample of 1.8 s and 1.0 s, respectively. Due to the additional vector signal analyzer (VSA), the hardware complexity is increased with configuration Probe-RX-C. Configuration Probe-RX could be used without the power amplifier (PA) but if so, it could be the case that the tagged object cannot be activated because of insufficient power density at the tag.

Conclusively, a measurement system consisting of three configurations and off-the-shelf hardware leveraging the determination of the $\sqrt{\Delta RCS}$ of tags was implemented and after the validation of the achieved performance, the θ -truncation of the utilized spherical test range at TU Wien, has been addressed. Since the spherical wave coefficients (SWCs), required for the SWE, can only be determined accurately if measurement samples that cover the entire sphere are present, pattern stitching [26] needs to be pursued. Pattern stitching allows to the determine the radiated field on the entire sphere from two truncated-sphere measurements. Since any physical manipulation of the antenna under test (AUT) changes its position relative to the origin of the measurement coordinate system, the measurement data that together cover the entire sphere from partial measurements cannot be simply put together. It requires coordinate system translation and rotation, which is done on SWCs, before the partial measurements can be stitched together. After the stitching, the so-obtained full-sphere SWCs allow then for comprehensive analysis, for example, field reconstruction at any distance larger than the minimum radial extent (MRE) with arbitrary angular granularity, compensation of positional offsets, and mode order truncation, i.e., filtering. Exemplary measurements with the Ucode7 label showed that pattern stitching converged successfully, which is underlined by SNR and SMSE values better than 30 dB and $-25\,\mathrm{dB}$ throughout the measurements. This indicates that the measurement system's dynamic range is sufficient to determine the SWCs accurately.

An applied scenario with a label on an empty crate and the crate filled with metal cans were compared. The results indicated while the $\sqrt{\Delta RCS}$ pattern obtained by the label on the empty crate resembles that of a dipole in free space very well, this no longer hold true for the filled crate. This suggests the dependency of tagged objects on the spherical direction, non-negligible for most phase-based localization algorithms. Consequently, the measurement system allows to carry out further measurements on complex tagged objects, which will contribute to improving the phase model, and eventually, the accuracy of phase-based localization with passive UHF RFID tags.



References

- K. Finkenzeller. RFID Handbook: Fundamentals and Applications in Contactless Smart Cards and Identification. Wiley, 2007. 427 pp. (cit. on pp. 1, 7, 8).
- James Stafford. "How Marks & Spencer is Using RFID to Improve Customer Service and Business Efficiency: A Case Study". In: Smart Packaging Technologies for Fast Moving Consumer Goods. Ed. by Joseph Kerry and Paul Butler. 1st ed. Wiley, Apr. 4, 2008, pp. 197-210. DOI: 10.1002/9780470753699.ch11 (cit. on p. 1).
- A. Rizzi, G. Romagnoli, and F. Thiesse. "A new framework for RFID use cases in fashion and apparel retailing". In: International Journal of RF Technologies: Research and Applications 7.2 (May 25, 2016), pp. 105–129. DOI: 10.3233/RFT-150075 (cit. on p. 1).
- Susana Garrido Azevedo and Helena Carvalho. "Contribution of RFID technology to better management of fashion supply chains". In: International Journal of Retail & Distribution Management 40.2 (Feb. 10, 2012), pp. 128-156. DOI: 10.1108/ 09590551211201874 (cit. on p. 1).
- Rajkishore Nayak et al. "RFID in textile and clothing manufacturing: technology and challenges". In: Fashion and Textiles 2.1 (June 27, 2015), p. 9. DOI: 10.1186/s40691-015-0034-9 (cit. on p. 1).
- D. M. Dobkin. The RF in RFID: Passive UHF RFID in Practice. Elsevier, 2008. 493 pp. (cit. on pp. 2, 5, 6, 37, 38).
- ETSI. ETSI EN 302 208. Version 3.4.1. Dec. 2023. URL: https://www.etsi.org/ deliver/etsi_en/302200_302299/302208/03.04.01_60/en_302208v030401p. pdf (visited on 06/16/2025) (cit. on pp. 2, 27).
- GS1. EPC Radio-Frequency Identity Protocols Generation-2 UHF RFID. Version 1.2.0. Oct. 2008. URL: https://ref.gsl.org/standards/gen2/1.2.0/ (visited on 04/19/2025) (cit. on pp. 2, 6, 7, 21, 23, 27, 29).
- Jingren Xu et al. "The Principle, Methods and Recent Progress in RFID Positioning Techniques: A Review". In: IEEE Journal of Radio Frequency Identification 7 (2023), pp. 50-63. DOI: 10.1109/JRFID.2022.3233855 (cit. on pp. 2, 3).
- Chenyang Li, Lingfei Mo, and Dongkai Zhang. "Review on UHF RFID Localization Methods". In: IEEE Journal of Radio Frequency Identification 3.4 (Dec. 2019), pp. 205–215. DOI: 10.1109/JRFID.2019.2924346 (cit. on p. 2).
- T. M. Pohl et al. "Direct Positioning in Single-Channel UHF-RFID Systems with Particle Filter-Based Algorithms". In: 2024 IEEE International Conference on RFID Technology and Applications (RFID-TA). 2024 IEEE International Conference on RFID Technology and Applications (RFID-TA). Daytona Beach, FL, USA: IEEE, Dec. 2024, pp. 74–77. Doi: 10.1109/RFID-TA64374.2024.10965174 (cit. on pp. 3, 62).

REFERENCES 65

T. M. Pohl, H. Arthaber, and C. F. Mecklenbräuker. "Reconstruction of Passive UHF RFID Tag Trajectories with a Distributed Antenna Reader System". In: 2023 IEEE International Conference on RFID (RFID). 2023 IEEE International Conference on RFID (RFID). Seattle, WA, USA: IEEE, June 2023, pp. 7–12. DOI: 10.1109/ RFID58307.2023.10178462 (cit. on pp. 3, 62).

- T. M. Pohl, H. Arthaber, and C. F. Mecklenbräuker. "Spatial Statistics of Received UHF RFID Phase in Indoor Environment Using Distributed Reader Antenna System". In: 2023 17th European Conference on Antennas and Propagation (EuCAP). 2023 17th European Conference on Antennas and Propagation (EuCAP). Florence, Italy: IEEE, Mar. 2023, pp. 1–4. DOI: 10.23919/EuCAP57121.2023.10133777 (cit. on pp. 3, 62).
- Evangelos Giannelos et al. "Robust RFID Localization in Multipath With Phase-Based Particle Filtering and a Mobile Robot". In: IEEE Journal of Radio Frequency Identification 5.3 (Sept. 2021), pp. 302-310. DOI: 10.1109/JRFID.2021.3086759 (cit. on pp. 3, 62).
- Chenglong Li et al. "ReLoc: Hybrid RSSI-and Phase-based Relative UHF-RFID Tag Localization with COTS Devices". In: IEEE Transactions on Instrumentation and Measurement (2020), pp. 1-1. DOI: 10.1109/TIM.2020.2991564 (cit. on pp. 3, 54, 59, 62).
- Nicolò Decarli. "On phase-based localization with narrowband backscatter signals". In: EURASIP Journal on Advances in Signal Processing 2018.1 (Dec. 2018), p. 70. DOI: 10.1186/s13634-018-0590-4 (cit. on pp. 3, 62).
- Pavel V. Nikitin et al. "Phase based spatial identification of UHF RFID tags". In: 2010 IEEE International Conference on RFID (IEEE RFID 2010). 2010 IEEE International Conference on RFID (IEEE RFID 2010). Orlando, FL: IEEE, Apr. 2010, pp. 102–109. DOI: 10.1109/RFID.2010.5467253 (cit. on pp. 3, 40, 62).
- P.V. Nikitin, K.V.S. Rao, and R.D. Martinez. "Differential RCS of RFID tag". In: Electronics Letters 43.8 (Apr. 12, 2007), pp. 431-432. DOI: 10.1049/e1:20070253 (cit. on pp. 3, 8, 10).
- S. Skali, C. Chantepy, and S. Tedjini. "On the measurement of the delta Radar Cross Section for UHF tags". In: 2009 IEEE International Conference on RFID. 2009 IEEE International Conference on RFID. Orlando, FL: IEEE, Apr. 2009, pp. 346–351. DOI: 10.1109/RFID.2009.4911176 (cit. on p. 3).
- Kai She et al. "Theory and Measurement of Delta RCS for RFID Tag on Various Materials". In: 2010 6th International Conference on Wireless Communications Networking and Mobile Computing (WiCOM). 2010 6th International Conference on Wireless Communications, Networking and Mobile Computing (WiCOM). Chengdu, China: IEEE, Sept. 2010, pp. 1-4. DOI: 10.1109/WICOM.2010.5600728 (cit. on p. 3).
- Audrey Pouzin et al. "Automated bench test for UHF RFID tags measurement in operational environment". In: International Journal of Microwave and Wireless Technologies 3.4 (Aug. 2011), pp. 415–422. DOI: 10.1017/S1759078711000511 (cit. on p. 3).
- D. Neunteufel, F. Galler, and H. Arthaber. "Comprehensive Measurement of Complexvalued Delta Radar Cross-section". In: 2018 6th International EURASIP Workshop on RFID Technology (EURFID). 2018 6th International EURASIP Workshop on RFID Technology (EURFID). Brno, Czech Republic: IEEE, Sept. 2018, pp. 1–7. DOI: 10.1109/EURFID.2018.8611768 (cit. on pp. 3, 16, 62).



REFERENCES66

F. Galler, D. Neunteufel, and H. Arthaber. "Complex-Valued Delta RCS Simulation of RFID Tags for Time of Flight Ranging Performance Assessment". In: 2019 IEEE International Conference on RFID Technology and Applications (RFID-TA). 2019 IEEE International Conference on RFID Technology and Applications (RFID-TA). Pisa, Italy: IEEE, Sept. 2019, pp. 285-290. DOI: 10.1109/RFID-TA.2019.8892198 (cit. on p. 3).

- [24]Daniel Neunteufel. "Delta-RCS characterization of RFID tags and implications on localization accuracy". Artwork Size: 81 pages Medium: application/pdf Publisher: TU Wien. PhD thesis. 2018. URL: https://repositum.tuwien.at/handle/20.500. 12708/3015 (visited on 09/11/2025) (cit. on pp. 3, 16, 62).
- J. E. Hansen, ed. Spherical Near-Field Antenna Measurements. Institution of Engineering and Technology, 2008. 387 pp. (cit. on pp. 4, 15, 31, 50–53, 62).
- J. Soklic. "Full-Sphere Antenna Measurements via Pattern Stitching". PhD thesis. TU [26]Wien, 2024. URL: https://repositum.tuwien.at/handle/20.500.12708/201044 (visited on 05/24/2025) (cit. on pp. 4, 15, 50, 51, 63).
- Robert Blair Green. "The general theory of antenna scattering". PhD thesis. The Ohio State University, 1963 (cit. on p. 7).
- R.K. Schneider. "A re-look at antenna in-band RCSR via load mismatching". In: IEEE Antennas and Propagation Society International Symposium. 1996 Digest. IEEE Antennas and Propagation Society International Symposium. 1996 Digest. Vol. 2. Baltimore, MD, USA: IEEE, 1996, pp. 1398-1401. DOI: 10.1109/APS.1996.549858 (cit. on p. 7).
- David M. Pozar. *Microwave engineering*. Fourth edition. Hoboken, NJ: John Wiley & Sons, Inc, 2012. 1 p. (cit. on p. 8).
- IEEE Standard for Radar Definitions. Piscataway, NJ, USA. DOI: 10.1109/ieeestd. 2024.10815038 (cit. on p. 9).
- Merrill Ivan Skolnik. Introduction to Radar Systems. 2d ed. New York: McGraw-Hill, 1980. 581 pp. (cit. on p. 9).
- E. F. Knott, J. F. Shaeffer, and M. T. Tuley. Radar Cross Section. SciTech Pub, [32]2004. 611 pp. (cit. on p. 9).
- IEEE Standard for Definitions of Terms for Antennas. DOI: 10.1109/IEEESTD.2014. [33]6758443 (cit. on pp. 10, 12).
- C. A. Balanis. Antenna Theory: Analysis and Design. 3. ed. Hoboken, N.J. Wiley-Interscience, 2005. 1117 pp. (cit. on pp. 10, 11, 36).
- G. F. Masters and S. F. Gregson. "Coordinate System Plotting for Antenna Measurements". In: AMTA Annual Meeting and Symposium 32 (2007) (cit. on pp. 11, 12).
- R.B. Dybdal. "Radar cross section measurements". In: Proceedings of the IEEE 75.4 (1987), pp. 498–516. DOI: 10.1109/PROC.1987.13757 (cit. on p. 13).
- IEEE Recommended Practice for Antenna Measurements. DOI: 10.1109/IEEESTD. 2022.9714428 (cit. on p. 13).



REFERENCES67

Olav Breinbjerg. "Spherical near-field antenna measurements — The most accurate antenna measurement technique". In: 2016 IEEE International Symposium on Antennas and Propagation (APSURSI). 2016 IEEE International Symposium on Antennas and Propagation & USNC/URSI National Radio Science Meeting. Fajardo, PR, USA: IEEE, June 2016, pp. 1019–1020. DOI: 10.1109/APS.2016.7696217 (cit. on p. 13).

- NSI-MI Technologies. Swing Arm over Azimuth Systems Webpage. URL: https: //www.nsi-mi.com/ (visited on 09/09/2025) (cit. on p. 14).
- EVONIK Industries. ROHACELL® HF Datasheet. Mar. 2024. URL: https:// products.evonik.com/assets/72/86/ROHACELL_HF_March_2024_EN_Asset_ 2347286.pdf (visited on 09/09/2025) (cit. on p. 15).
- Kerem Kapucu, Muriel Pauli, and Catherine Dehollain. "A fast active leakage cancellation method for UHF RFID readers". In: 2017 IEEE International Conference on RFID (RFID). 2017 IEEE International Conference on RFID (RFID). Phoenix, AZ, USA: IEEE, May 2017, pp. 182–186. DOI: 10.1109/RFID.2017.7945606 (cit. on pp. 16, 62).
- The MathWorks Inc. MATLAB. Version R2024b. Natick, Massachusetts, United States, 2024. URL: https://www.mathworks.com (visited on 04/19/2025) (cit. on p. 27).
- Steven W. Smith. The scientist and engineer's guide to digital signal processing. 2nd edition. OCLC: 493473234. San Diego (Calif.): California Technical Pub., 1999. URL: https://www.dspguide.com/ (cit. on p. 28).
- Alan V. Oppenheim and Roland W. Schafer. Discrete-time signal processing. Third edition, Pearson New international edition. Always learning. Harlow: Pearson, 2014. 1 p. (cit. on p. 29).
- NXP Semiconductors. SL3S1204 UCODE 7 Datasheet. Rev. 4.0. Mar. 2019. URL: https://www.nxp.com/docs/en/data-sheet/SL3S1204.pdf (visited on 04/21/2025) (cit. on pp. 37-39).
- KATHREIN Solutions GmbH. MidRange 100° Pro Antenna ETSI Version Datasheet. URL: https://www.kathrein-solutions.com/wp-content/uploads/2024/08/ MidRange-100%C2%B0-PR0_S-MidRange-100%C2%B0-PR0-Antenna-52010082_ 083_172_936B116d.pdf (visited on 09/09/2025) (cit. on pp. 41, 42).
- ANDREW an Amphenol company. FSJ1P-50A-42 Coaxial Cable Datasheet. Mar. 2025. URL: https://www.andrew.com/globalassets/digizuite/115473-p360fsj1p-50a-42-external.pdf (visited on 09/09/2025) (cit. on p. 47).



Appendix A

Utilized Equipment and Software

Table A.1: Overview of the equipment and software used.

RF Signal Source	Agilent E8244A PSG
Power Splitter	Mini-Circuits ZN2PD2-63+
Digital Attenuator	Analog Devices HMC472ALP4E on PCB
Sequencer	Rohde & Schwarz SMBV100A
Power Amplifier	Mini-Circuits ZHL-30W-252+
Power Meter	Agilent E4417A
Power Sensor	Agilent E9327A
Directional Coupler	Atlantec A3202-10
Directional Coupler	Atlantec A3202-20
RF Switch	Hittite Microwave Corporation HMC545 on PCB
Vector Signal Analyzer	Keysight N9040B UXA
Vector Signal Analyzer	Keysight M9391A PXIe
Probe Antenna	NSI-RF-RGP-10
Pickup Antenna	Kathrein MiRa ETSI Version
Step Attenuator	Rohde & Schwarz RSG
Test Range	NSI-MI Swing Arm-over-Azimuth System
Vector Signal Analysis Platform	Keysight 89600 VSA Software Version 21.2
General Programming Platform	The Math Works Inc. MATLAB version R2024b